Electromagnetic properties of baryons from lattice QCD

Sharada Boinepalli
Supervisors: A/Prof. Derek B. Leinweber and Prof. Anthony G. Williams

Centre for the Subatomic Structure of Matter
and
Department of Physics
University of Adelaide, Australia

Thesis submitted for the degree of PhD

Date of submission:

5 April 2006

To my family

“Whatever you do will be insignificant,

but it is very important that you do it.”

M. K. Gandhi

Abstract

Electromagnetic properties of the octet and decuplet baryons are calculated in quenched QCD on a $20^3 \times 40$ lattice with a lattice spacing of 0.128 fm using the fat-link irrelevant clover (FLIC) fermion action.

FLIC fermions enable simulations to be performed efficiently at quark masses as low as 300 MeV. By combining FLIC fermions with an improved conserved vector current we ensure that discretization errors occur only at $\mathcal{O}(a^2)$ while maintaining current conservation.

Magnetic moments, charge radii and magnetic radii are extracted from the electric and magnetic form factors for each individual quark sector. From these the corresponding baryon properties are constructed.

Our results for the octet baryons are compared with the predictions of Quenched Chiral Perturbation Theory (QχPT) and experimental values where available. Results for the charge radii and magnetic moments of the octet baryons are in accord with the predictions of the QχPT, suggesting that the sum of higher order terms makes only a small contribution to the chiral expansion. The regime where chiral physics dominates remains to be explored. We establish the non-analytic behavior of the charge radii and magnetic moment in the case of octet baryons. The neutron charge radius suggests that the chiral regime is still far away. We establish substantial environment sensitivity in the quark behavior in the low mass region. We establish that the u and d quarks make substantial and important contribution to the magnetic moment of the Λ contradicting the predictions of the Simple Quark Model.

We present the $E0$ and $M1$ form factors of the decuplet baryons and the charge radii and magnetic moments. We compare the decuplet baryon results with the lattice calculation of charge radii and magnetic moments of octet baryons. We establish that the environment sensitivity is far less pronounced in the case of the decuplet baryons compared to that in the octet baryons. A surprising result is that the charge radii of the decuplet baryons are generally smaller than that of the octet baryons.

Magnetic moment of the Δ^+ shows a turn over in the low quark mass region, making it smaller than the proton magnetic moment. This is consistent with the expectations of the Quenched Chiral Perturbation Theory. A similar turn over is also noticed in the magnetic moment of the Σ^{*0}, but not for Ξ^* where only kaon loops can appear in Quenched QCD.

We present results for the higher order moments of the decuplet baryons, i.e., the electric quadrupole moment $E2$ and the magnetic octupole moment $M3$. With these results we provide the first conclusive analysis which shows that decuplet baryons are deformed. The electric quadrupole moment of the Ω^- baryon is positive when the negative charge factor is included, and is equal to 0.014 ± 0.005 fm^2, indicating an oblate shape.

Statement of originality

This work contains no material which has been accepted for the award of any other degree or diploma in any university or tertiary institution. To the best of my knowledge and belief this contains no material previously published or written by another person, except where due reference has been made in the text.

I give consent to this copy of my thesis, when deposited in the University Library, being available for loan and photocopying.

Acknowledgments

I wish to take this opportunity to thank my supervisors, Derek Leinweber and Anthony Williams for all their patient guidance and encouragement. I thank the CSSM for the excellent research facilities and SAPAC and APAC for the generous and valuable computing time. I also sincerely thank Dr. James Zanotti for helping me during the initial phases, his continued help through out the research and for his valuable help when I was wading through thousands of lines of code.

Thanks are due to Sara, Sharon and Ramona for keeping me sane through out the time. Deeply felt thanks to my family, my husband Murali and my little girls Madhu and Anu for sticking with me through thick and thin and cheering me all along the way.

Table of Contents

List of Figures

List of Tables

Chapter 1

Introduction

Quantum Chromodynamics (QCD) is part of the fundamental theory known as the Standard Model that explains particle interactions at the most elementary quark level. QCD describes the Strong Interactions that bind the hadrons together. It is formulated in terms of quarks and gluons, the main players of the Strong Interactions. QCD can be studied perturbatively at short distances. However, at long distances QCD is a non-perturbative theory in which the gauge-fields, viz., gluons are self-interacting making it impossible to calculate analytically the non-perturbative properties of QCD from first principles. The complexity of the QCD vacuum is evident in the non-vanishing vacuum expectation values of quark gluon operator products having vacuum quantum numbers. Numerical simulation is the only known first principle method for obtaining the properties of the strongly interacting particles. Using numerical simulations, one can calculate observables directly from the QCD Lagrangian, fully accounting for non-perturbative interactions.

The lattice formulation of QCD is widely accepted as the best tool for the calculation of non-perturbative properties of the QCD. Lattice QCD is formulated by discretizing the continuum QCD action on a space-time lattice of finite spacing a. The finite lattice spacing and finite volume of the total lattice cause systematic uncertainties in the calculated observables. Direct simulation of QCD for light current quark masses, near the chiral limit ($m_\pi^2 \to 0$) is computationally expensive. Vast computer resources and advanced techniques in formulation of lattice actions greatly reduced these errors. The FLIC fermion action is one such improved action. Apart from minimizing errors due to finite lattice spacing it also provides improved access to the light quark mass regime, hitherto unexplored.

We present here the results of the lattice calculation of electromagnetic properties of the octet and the decuplet baryons. The electric and magnetic form factors are calculated as ratios of the three point and two point correlation functions. From the form factors so calculated we can subsequently extract quantities such as charge radii, magnetic moments and magnetic radii.

A brief primer on Elementary Particle Structure with focus on the octet and decuplet baryon properties is given in Chapter 2. Chapter 3 contains essential features of QCD. Lattice QCD is introduced in Chapter 4.

Since we compare our results with the prediction of Quenched Chiral Perturbation Theory, a brief introduction of this is given in Chapter 5. The simulation details and lattice calculation of the form factors is discussed in Chapter 6 . Results for the octet and the decuplet baryons are discussed in Chapters 7 and 8 respectively. We summarize our conclusions and future directions in Chapter 9.

The numerical values of all the properties calculated are listed in tables in Appendix A. We use the natural units in which $\hbar = 1$ and $c = 1$.

Chapter 2

Elementary particles

Three quarks for Muster Mark......
- James Joyce (Finnegan's Wake)

2.1 Introduction

Matter is composed of atoms which consist of a nucleus and surrounding electrons. The nucleus further contains protons and neutrons, together denoted as the nucleons. Many new particles have been created and observed in scattering experiments of fundamental particles following the advent of particle accelerators. These are currently classified depending on the type of interactions in which they play a role. The four fundamental types of interaction in which the particles interact are the Strong, Electromagnetic, Weak and Gravitational interactions.

Of these, Electromagnetism (EM), Weak Interactions (WI), and Strong Interactions (SI) are described by gauge field theories. EM and WI together manifest themselves as Electroweak interactions. The strong interactions originate in the color charge of the quarks. The strong force is mediated by exchange of gluons, the electromagnetic force by exchange of photons, and the weak force via the $W^{\pm}$, Z^0 bosons which acquire a mass via the Higgs mechanism.

Broadly the particles are grouped into hadrons (that interact via the strong interactions), leptons (that are insensitive to the strong interactions) and gauge bosons (that interact via the electromagnetic and weak interactions).

Hadrons are further classified into baryons and mesons. Baryons (for eg, nucleons) are fermions while the mesons are bosons. There are a number of hadrons, while the number of leptons and gauge bosons is limited. Hadrons are further made of fundamental particles, viz., the quarks, which are limited in number like the leptons.

The structure of hadrons suggests a multiplet structure similar to irreducible representations of an internal symmetry group $SU(3)$. Electron scattering and deep inelastic scattering experiments confirm the existence of an internally symmetric structure of the hadrons.

Leptons and quarks are fermionic spin-1/2 particles forming the fundamental constituent matter. The gauge bosons which are spin-1 particles act as “force carriers” facilitating the interactions between the leptons and quarks.

There is no experimental evidence of existence of any internal structure of the leptons and the gauge bosons.

The “Standard Model” is an attempt to explain all the particle physics phenomena using three distinct types of elementary particles, viz., the leptons, quarks and the gauge bosons [1].

The Standard Model treats the leptons and quarks as point particles, without internal structure or excited states. Groups of six leptons and six quarks form the basic constituents of matter. These are arranged into three generations of families and they interact exchanging the vector bosons, in the four types of interactions. In addition, each quark comes in three colors while the leptons are colorless.

2.2 Quark Model

Hadrons fall into multiplets, suggesting underlying internal symmetries. Each multiplet can be viewed as a realization of an irreducible representation of an internal symmetry group. Elements of each multiplet have very nearly equal masses. Hadrons are bound states of quarks and hence the strong interactions are basically interactions between the quarks.

Quarks, like leptons fall into six flavors,viz, the up, down, strange, charmed, top and bottom (u, d, s, c, t, b) quarks. These are grouped into three generations, denoted as

$$\begin{pmatrix} u \\ d \end{pmatrix}, \begin{pmatrix} c \\ s \end{pmatrix}, \begin{pmatrix} t \\ b \end{pmatrix}. \tag{2.1}$$

The properties of quarks are listed in the table below. There is no experimental evidence

Table 2.1: Properties of the quarks. Data from Particle Data Group 2005 [2].

Flavor	Charge	Mass
up (u)	$\frac{2}{3}$	1-5 MeV
down (d)	$-\frac{1}{3}$	3-9 MeV
strange (s)	$-\frac{1}{3}$	75-170 MeV
charm (c)	$\frac{2}{3}$	1.15-1.35 GeV
bottom (b)	$-\frac{1}{3}$	4.0 - 4.4 GeV
top (t)	$\frac{2}{3}$	174.4 ± 5.1 GeV

of isolated quarks.

Hadrons are characterized by a set of quantum numbers, B (baryon number), Q (charge), S (strangeness), C (charm), $\tilde{B}$ (Beauty) and T (truth). $Eightfold$ way introduced by Murray Gell-Mann and Yuval Ne'eman [3] in 1961 classified the baryons and mesons into geometrical patterns depending upon their charge and strangeness. Thus strange ($S \neq 0$) and non-strange baryons ($S = 0$) form groups of octets, singlets and decuplets. The structure of these families indicates a $SU(3)_{\text{flavor}}$ symmetry. However, this symmetry of the u, d, s quarks is broken due to the heavy mass of the s quark. This results in large mass splittings among hadrons within each multiplet. Mesons on the other hand form super multiplets of nine particles each called nonets.

Baryons are hadrons with baryon number $B = 1$. In the non-relativistic quark models baryons are bound states of three quarks qqq, implying that the quarks carry a baryon number of $1/3$.

Mesons are quark-anti quark pairs $q\overline{q}$ with baryon number $B = 0$. The pseudo scalar nonet indicated in Fig. 2.1 consists of negative parity states. The spins of the quark-anti-quark pair are anti-parallel making the net spin zero. The pseudo-scalar meson nonet is also a zero angular momentum state making the total angular momentum $J = 0$.

The baryon octet and decuplet particles are shown in figs. 2.2 and 2.3. The diagrams show the particle state's hyper charge (Y) and Isospin projection I_3. Hyper charge is defined as the sum of the strangeness S and the baryon number B. The zero strangeness baryons like the nucleons and Δ resonances have hyper charge 1, while the states with one strange quark (Σ, Σ^*) have zero hyper charge and states with two strange quarks (Ξ, Ξ^*) have $Y = -1$.

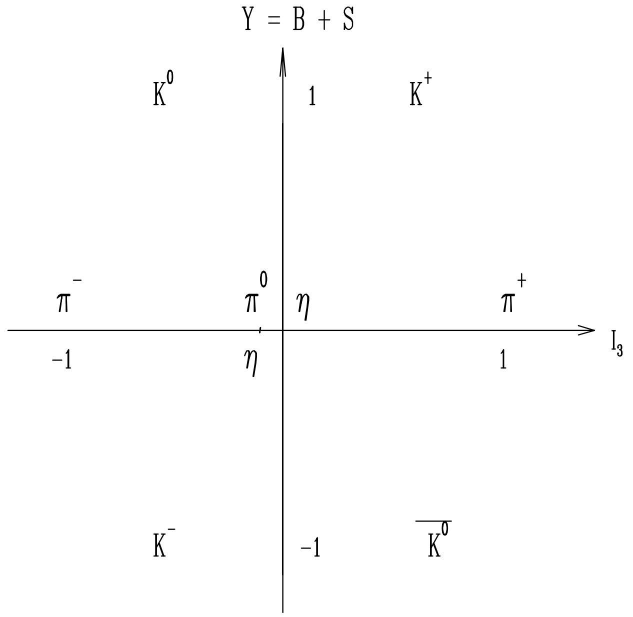

Figure 2.1: The Meson Octet.

The lightest baryon super multiplets that are experimentally observed are the octet ($J^P = 1/2^+$) and the decuplet ($J^P = 3/2^+$) particles. The octet includes the nucleons, the Λ, Σ and Ξ particles. The two nucleons,viz., proton and the neutron form an isospin 1/2 state, the three Σ particles form an isospin 1 state, Λ is an isospin 0 singlet and the two Ξ particles form an isospin 1/2 state. The Λ and the Σ^0 are both composed of uds quarks. However, the $u-d$ system in the Σ^+ is a spin-1 system with the u and d spins aligned parallel to each other, while that in the Λ is a spin-0 state, the u and d spins being anti-parallel states.

The decuplet $3/2^+$ states are all resonances except the Ω^- which decays through the weak interactions with a life time of nearly $10^{-10}s$.

2.2.1 Color charge of quarks

Quarks have an additional degree of freedom, i.e., the color. Consider the pion-nucleon resonance Δ^{++} which has spin $J = 3/2$ and the Ω^- particle, which has $J_z = 3/2$. The spin wave function is symmetric with all the three quark spins aligned. The quantum numbers of Δ^{++} suggest that it is made up of three u quarks, while the Ω^- is made up of three s quarks. This implies that the total spin, flavor and space function is symmetric with respect to interchange of quarks, unless the orbital part of the wave function were antisymmetric. But both Δ^{++} and Ω^- are the lowest lying states with their internal quantum numbers. They correspond to the three-quark ground state, which should

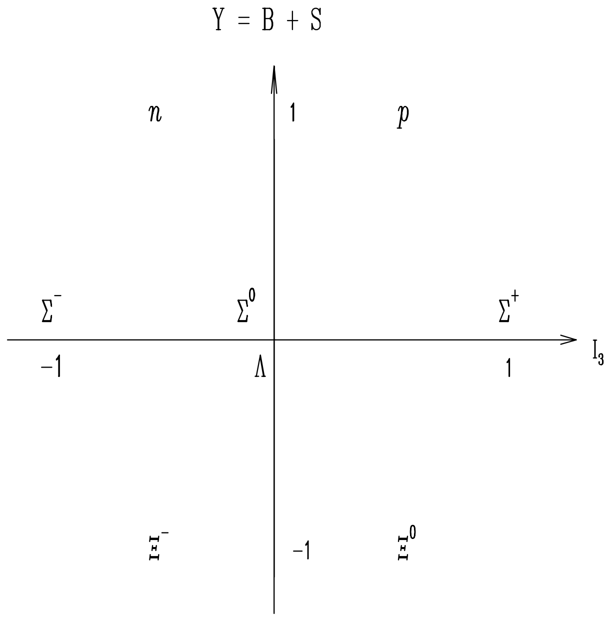

Figure 2.2: The Baryon Octet.

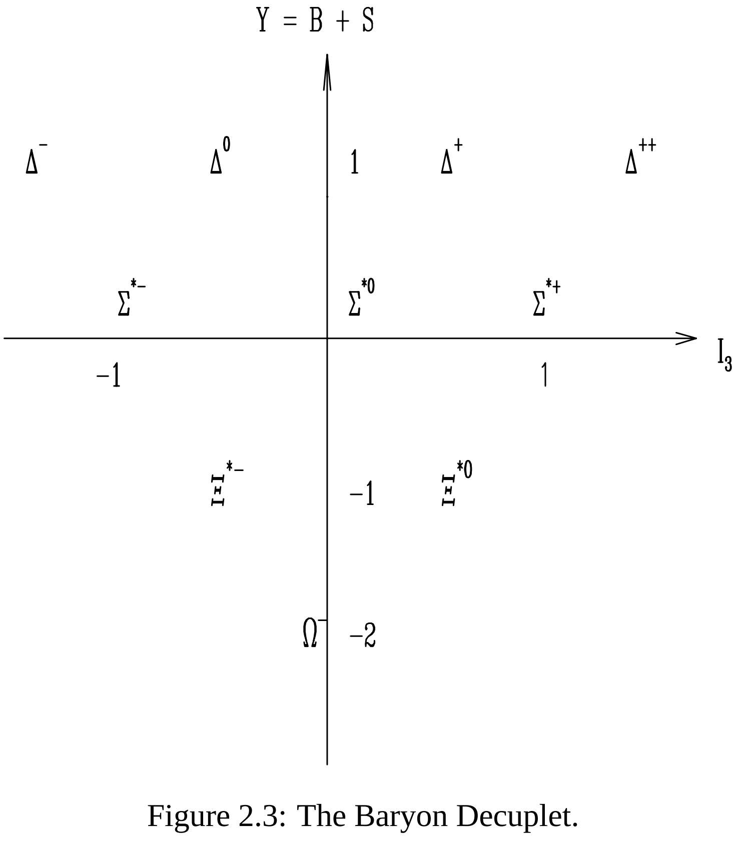

Figure 2.3: The Baryon Decuplet.

have both total angular momentum and relative angular momentum equal to zero and hence a symmetric orbital wave function. But the quarks are spin-1/2 particles and obey Fermi-Dirac statistics, with an antisymmetric wave function. Therefore the antisymmetry in the total wave function of the Δ^{++} and Ω^{-} must be arising out of another hidden quantum number, color. Assigning three states to this color quantum number allows the three u quarks to stay in spins aligned state, in the case of Δ^{++} and the three s quarks in Ω^{-}.

The three quark colors are called red, blue and green, forming the representation of a $SU(3)_{\text{color}}$ symmetry. Since the color degrees of freedom are not observed experimentally, the hadronic particles are color singlets.

Similarly no mesons carrying color quantum number have been experimentally detected, implying that a quark and an anti quark system with same color forms a color singlet.

2.2.2 Baryon mass splittings

The baryon members of the same isospin multiplet exhibit small mass differences, while those in different isospin multiplets show large mass differences. Thus all the Σ particles, which form an isospin 1 multiplet have nearly same mass, but they show a large mass difference with the nucleons, which form an isospin 1/2 system. The heaviest isospin multiplets are those that have s quarks, suggesting that the mass differences arise due to the difference in the heavy s quark and the light u/d quarks. Tables 2.2 and 2.3 list the experimentally measured masses of the octet and decuplet baryons.

Table 2.2: Masses of the octet baryon states $L = 0$, $J^P = 1/2^+$. Data from Particle Data Group 2005 [2].

Baryon	Mass (MeV)	I_3	I
p(uud)	938	1/2	1/2
n(udd)	940	-1/2	1/2
$\Lambda(uds)$	1116	0	0
$\Sigma^+(uus)$	1189	1	1
$\Sigma^0(uds)$	1193	0	1
$\Sigma^-(uds)$	1197	-1	1
$\Xi^0(uss)$	1315	1/2	1/2
$\Xi^-(dss)$	1321	1/2	1/2

Table 2.3: Masses of the decuplet baryon states $L = 0, J^P = 3/2^+$. Data from Particle Data Group 2005 [2].

Baryon	Mass (MeV)	I_3	I
$\Delta^{++}(uuu)$	1232	3/2	3/2
$\Delta^{+}(uud)$	1232	1/2	3/2
$\Delta^{0}(udd)$	1232	-1/2	3/2
$\Delta^{-}(ddd)$	1232	-3/2	3/2
$\Sigma^{*+}(uus)$	1383	1	1
$\Sigma^{*0}(uds)$	1384	0	1
$\Sigma^{*-}(dds)$	1387	-1	1
$\Xi^{*0}(uss)$	1532	1/2	1/2
$\Xi^{*-}(dss)$	1535	1/2	1/2
$\Omega^{-}(sss)$	1672	0	0

2.2.3 Baryon Magnetic Moments

Magnetic moments of all the members of $1/2^+$ octet baryons except the Σ^0 have been experimentally measured Σ^0 [2].

If the quarks are in zero orbital angular momentum state, the baryon magnetic moments are just the sum of the quark magnetic moments. The magnetic moment of a quark of charge e_q and mass m_q is given as [1]

$$\mu_q = \left(\frac{e_q M_p}{m_q}\right)\mu_N \,, \tag{2.2}$$

where M_p is the mass of the proton and $\mu_N = e/2M_p$ is the nuclear magneton.

In the $1/2^+$ baryons B with quark composition xxy, the two x quarks are in a symmetric spin-1 state with with parallel spins and anti parallel to the y quark. Magnetic moment of such a baryon is given by the Simple Quark Model(SQM) as

$$\mu_B = \frac{4}{3}\mu_x - \frac{1}{3}\mu_y \,. \tag{2.3}$$

Hence the proton (uud) magnetic moment is

$$\mu_p = \frac{4}{3}\mu_u - \frac{1}{3}\mu_d \,. \tag{2.4}$$

Neglecting the small mass difference between the u and d quarks, the proton magnetic moment is

$$\mu_p = \frac{M_p}{m_u}\mu_N \,. \tag{2.5}$$

If the experimentally measured value of the proton magnetic moment, $2.79\mu_N$ is substituted in the above relation, the mass of the u or d quark mass turns out to be approximately 336MeV. In the case of Λ (uds), the ud pair is in a spin-0 state and hence makes no contribution to the Λ spin and magnetic moment. The entire magnetic moment of the Λ arises from that of the s quark and is given by

$$\mu_\Lambda = \mu_s = -\frac{1}{3}\frac{M_p}{m_s}\mu_N \,. \tag{2.6}$$

Substituting the experimental value for the μ_Λ as $-0.613\mu_N$, the s quark mass turns out to be nearly 510MeV. There is a wide disagreement between the experimentally measured values of the quark masses with the above suggestions. The experimentally measured values of magnetic moment of Ξ^- is $-0.651 \pm 0.003\mu_N$ and that of Λ is $-0.613 \pm 0.004\mu_N$, making their ratio to be 1.062 ± 0.012. Using Eq. (2.3), the magnetic moment of the $\Xi^-(dss)$ is $\frac{4}{3}\mu_s - \frac{1}{3}\mu_d$, where μ_s and μ_d are the magnetic moments of the s and d quarks respectively. With the assumption that the entire magnetic moment of the Λ is due to the s quark alone (Eq. (2.6)), the ratio of the magnetic moments μ_{Ξ^-}/μ_Λ turns out to be 0.836, in disagreement with the experiment.

Simple quark model assumes the three quark baryon states to be zero angular momentum states. But in reality, the ground states of strongly interacting systems are not pure S-waves but might contain small admixtures of non-zero angular momentum states. This could be a reason for the discrepancy in the predicted values of the SQM and experimentally measures values.

Chapter 3

Quantum Chromodynamics

3.1 Gauge Field Theories

Gauge theories are theories with a particular type of symmetry, called gauge invariance. The principle of gauge invariance requires that the theory be invariant under a particular gauge transformation [4].

An example of a gauge field theory is the Quantum Electrodynamics (QED) which describes the dynamics of charged fermions. QED is an abelian gauge field theory with local invariance under the unitary abelian group of transformations, $U(1)$. Imposing local gauge invariance gives rise to the electromagnetic vector potentials A_μ. Current conservation and the zero mass of the photon are the consequences of gauge invariance of the electromagnetic field. The QED Lagrangian density is given by

$$\mathcal{L}_{\mathrm{QED}} = \overline{\psi}(x)(i\not{D} - m)\psi(x) - \frac{1}{4}F_{\mu\nu}F^{\mu\nu}\,, \tag{3.1}$$

where the kinetic term $F^{\mu\nu}_{\mu\nu}$ is gauge invariant and is given by

$$F_{\mu\nu}(x) = \partial_\mu A_\nu(x) - \partial_\nu A_\mu(x)\,. \tag{3.2}$$

The covariant derivative D_μ is defined as

$$D_\mu = \partial_\mu - ieQA_\mu(x)\,, \tag{3.3}$$

where Q is a real arbitrary constant defining the unitary transformations as $U(1) = \exp(iQ\theta)$.

Yang-Mills theory is a theory of a multicomponent field invariant under a non-abelian group of transformations, $SU(2)$.

The number of gauge fields in a theory is equal to the number of generators of the gauge group. Therefore QED has one gauge field, the photon. The relevant groups for the weak, electromagnetic and strong interactions are $SU(2)$, $U(1)$ and $SU(3)$ respectively. The electromagnetic and weak interactions can be combined as unified gauge theory, invariant under a gauge group $SU(2) \times U(1)$.

QED and QCD describe interactions of different strengths, which are mediated by massless spin-1 bosons which couple to conserved charges.

3.2 Quantum Chromodynamics

QCD is a quantized non-abelian gauge field theory, describing the strong interactions. It is formulated in terms of the quarks and gluons, the bosons that mediate the strong interactions. It demands local gauge invariance under an $SU(3)$ gauge group.

Quarks carry the color charge with three degrees of freedom. Any gauge transformation on such a system inter-mixes the three colors. The photons that mediate the electromagnetic interactions between electrically charged particles do not carry any electric charge themselves. In contrast, the gluons carry color charge themselves and hence interact among themselves. $SU(3)$ has eight generators and hence the gauge fields gluons come in eight colors. The gluon-gluon interaction of QCD has no QED analogue and is the cause of the main differences between the QED and QCD.

All bound states of quarks are color singlets and have integral electric charges. Isolated quarks with fractional electric charges and color are not observed in nature. This is the property of “color confinement” exhibited by the strong interactions. It further implies that gluons too cannot be observed as isolated free particles with non-zero color charges.

The strong interaction gets weaker at short distances. An isolated electric charge polarizes the vacuum around it and surrounds itself with electron positron pairs. Similarly an isolated color charge surrounds itself with quark-anti quark pairs. The virtual cloud of $q\overline{q}$ pairs increases the coupling constant at short distances. In addition to quark anti-quark pairs an isolated color charge can surround itself with gluons, decreasing the coupling constant at short distances (large momentum scales). The quarks at short distances behave like free particles, known as the property of “asymptotic freedom”. At low energies the coupling constant is nearly equal to 1 making it impossible to use methods of perturbation theory.

The third property of QCD that is of interest is the “Dynamical Chiral Symmetry

Breaking" which is discussed more in subsequent chapters. The chiral symmetry is spontaneously broken by the QCD interactions. This is indicated by the non-zero proton mass even under the assumption of massless quarks. The fact that the baryons do not occur in degenerate parity doublets is also a direct consequence of the chiral symmetry breaking by the QCD.

3.2.1 QCD Lagrangian

The Lagrangian describing the interaction among quarks and gluons is given as

$$\mathcal{L}_{\mathrm{QCD}} = -\frac{1}{4}F^{(a)}_{\mu\nu}F^{(a)\mu\nu} + i\sum_q \overline{\psi}^i_q \gamma^\mu (D_\mu)_{ij}\psi^j_q - \sum_q m_q \overline{\psi}^i_q \psi^i_q \,, \tag{3.4}$$

where

$$F^{(a)}_{\mu\nu} = \partial_\mu A^a_\nu - \partial_\nu A^a_\mu + g_s f_{abc} A^b_\mu A^c_\nu \,, \tag{3.5}$$

and

$$(D_\mu)_{ij} = \delta_{ij}\partial_\mu - ig_s \sum_a \frac{\lambda^a_{ij}}{2} A^a_\mu \,. \tag{3.6}$$

Here g_s is the QCD coupling constant, f_{abc} are the structure constants of the $SU(3)$ algebra, $\psi^i_q(x)$ are four-component Dirac spinors associated with each quark field of color i and flavor q and A^a_μ are the eight gluon fields. The eight 3×3 Gell-Mann matrices λ_a are the generators of the $SU(3)$ and obey the Clifford algebra,

$$[\lambda_a, \lambda_b] = 2i f_{abc}\lambda_c \,. \tag{3.7}$$

The kinetic term (Eq. 3.5) in QCD has an extra term compared to the kinetic term in QED (Eq. 3.2) due to the non-abelian nature of the gauge group $SU(3)$. This term implies that the gluons themselves carry the color charge. The Euler-Lagrangian equation corresponding to the free gluon fields produces the source terms when the Lagrangian is varied with respect to the gluon fields A_μ. In QED Lagrangian on the other hand, the free photon field Lagrangian depends solely on the derivatives of the photon fields.

All quarks and gluons couple to each other with the same coupling constant g_s, which depends on energy through renormalization.

The QCD Lagrangian is invariant under local non-abelian gauge transformations that transform its fields according to

$$\psi_i(x) \to \psi'_j(x) = U_{ij}(x)\psi_j(x) \,, \tag{3.8}$$

where

$$U(x) = exp{-}i\frac{g_s}{2}\lambda_a\theta_a(x)\,. \tag{3.9}$$

To ensure gauge invariance of the QCD theory the vector gluon fields transform as

$$A^a_\mu(x) \rightarrow A'^a_\mu(x) = A^a_\mu(x) + \partial_\mu\theta^a(x) - g_s f_{abc}\theta^b(x)A^c_\mu\,. \tag{3.10}$$

Here θ^a are the local parameters depending on x. The QCD Lagrangian includes the self-interactions among the gluon fields A^a_μ through the term $g f_{abc}A^b_\mu A^c_\nu$ in the $F_{\mu\nu}$ definition. This is the main source of asymptotic freedom in the QCD Lagrangian.

At large separations, the coupling constant increases due to the self-interacting gluons and gives rise to confinement. Vacuum polarization effects in QCD are very strong due to the massless gluons and the strong coupling constant. The QCD vacuum contains continuously appearing, interacting and disappearing gluons of virtual quark-anti quark pairs. This non-vanishing quark and gluon condensate does not render to a perturbative analytical treatment.

At high energies (short distances) experiments probe perturbative QCD successfully. At low and intermediate energies Lattice Gauge Theory is the only known first-principles technique for studying QCD.

The Chiral symmetry properties of QCD and their implications are discussed in Chapter 5.

Chapter 4

Lattice QCD

4.1 Introduction

The Lattice Gauge Theory provides a framework to study QCD non-perturbatively from first principles [5, 6]. The lattice formulation of QCD, based on path integral formalism is now well established. Different formulations of the lattice action have greatly reduced systematic uncertainties like errors associated with finite lattice spacing and volume. Lattice QCD uses the Euclidean space, which is obtained by a Wick rotation on Minkowski space,

$$t_M \to -it_E \,. \tag{4.1}$$

This makes the trace of the evolution operator look like the partition function, enabling one to use the standard techniques of Statistical Mechanics to extract physically relevant information.

In lattice QCD the space-time system is discretized into a four-dimensional grid. The quark fields $\psi(x)$ reside on the lattice sites designated as x. The quark fields carry the properties of the quarks viz., color, flavor and Dirac indices. The gluon fields are defined through the link variables $U_\mu(x)$ that connect the adjacent sites on the lattice. The Feynman path integral approach is used to calculate the physical observables [7]. The ground state that dominates the path integral is the QCD vacuum. Excitations of the ground state correspond to the hadrons.

4.2 Gluon Field Action

The gluon fields $A_\mu(x)$ of the QCD field are related to the link variables through

$$U_\mu(x) = \mathcal{P} \exp ig \int_0^a A_\mu(x + \lambda\hat{\mu}) d\lambda \,, \tag{4.2}$$

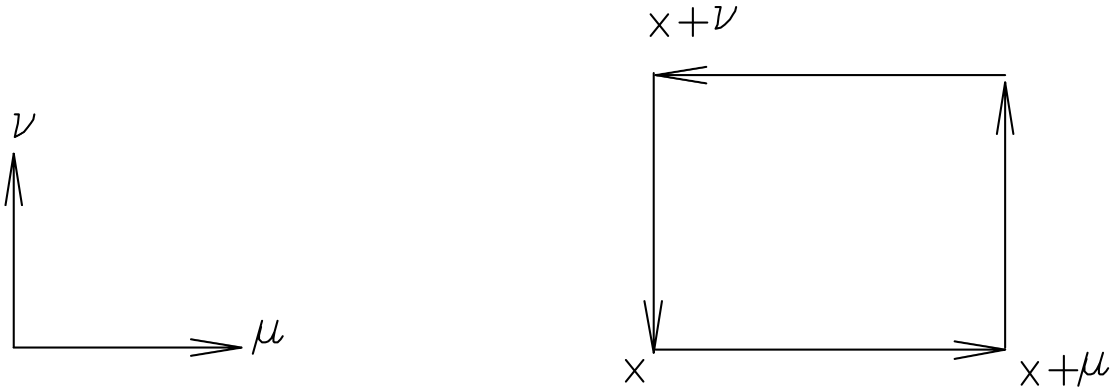

Figure 4.1: The smallest plaquette on lattice.

where the operator $\mathcal{P}$ path-orders the gluon fields along the integration path, a is the lattice spacing and g is the coupling constant and μ denotes the space-time directions. Note that $\mu = 1, 2, 3$ forms the three dimensional space while $\mu = 4$ refers to the time direction.

Under a gauge transformation $\Lambda(x)$, the various fields transform as

$$\begin{aligned} \psi(x) &\rightarrow \Lambda(x)\psi(x)\,, \\ U_\mu(x) &\rightarrow \Lambda(x)U_\mu(x)\Lambda(x+\hat{\mu})^{-1}\,, \\ \overline{\psi}(x) &\rightarrow \overline{\psi}(x)\Lambda(x)\,. \end{aligned} \tag{4.3}$$

Gauge invariant objects can be constructed on the lattice out of closed loops of gluon fields or strings of gluon fields with quark fields at one end and an anti quark field at the other. The simplest non-trivial gauge invariant object on the lattice is the plaquette (Fig. 4.1) which is constructed as the product of four link variables enclosing a unit square on the lattice,

$$P_{\mu\nu}(x) = \frac{1}{3}\mathcal{R}e\mathrm{Tr}\left(U_\mu(x)U_\nu(x+\hat{\mu})U_\mu^\dagger(x+\hat{\nu})U_\nu^\dagger(x)\right)\,. \tag{4.4}$$

Using the relation between the link variables and the gluon fields the above equation can be rewritten as

$$P_{\mu\nu}(x) = \frac{1}{3}\mathcal{R}e\mathrm{Tr}\mathcal{P}e^{ig\int_\Box A\cdot\mathrm{d}x}\,. \tag{4.5}$$

The box at the foot of the integral indicates that the integral is over the closed plaquette loop. On expanding the exponential the above equation becomes

$$P_{\mu\nu}(x) = \frac{1}{3}\mathcal{R}e\mathrm{Tr}\mathcal{P}\left[1 + ig\int_\Box A\cdot\mathrm{d}x - \frac{1}{2}\left(g\int_\Box A\cdot\mathrm{d}x\right)^2 + \mathcal{O}(A^3)\right]\,. \tag{4.6}$$

In the above integral path-ordering is essential in a non-abelian theory to ensure the action has errors which are $O(a^2g^2)$. Since we wish to remove classical $O(a^2)$ errors from the action, it is sufficient to work with the abelian theory.

From the Stokes' theorem we have for an abelian theory,

$$\begin{aligned}\int_\square A\cdot \mathrm{d}x &= \int_{-a/2}^{a/2} \mathrm{d}x_\mu \mathrm{d}x_\nu \left[\partial_\mu A_\nu\left(x_0+x\right)-\partial_\nu A_\mu\left(x_0+x\right)\right] \\ &= \int_{-a/2}^{a/2} \mathrm{d}x_\mu \mathrm{d}x_\nu F_{\mu\nu}\left(x_0+x\right) \\ &= a^2F_{\mu\nu}(x_0)+\frac{a^4}{24}\left(\partial_\mu^2+\partial_\nu^2\right)F_{\mu\nu}(x_0)+O\left(a^6,A^2\right)\,, \end{aligned} \tag{4.7}$$

where x_0 is the centre of the loop. In the above equation the definition of the abelian field strength tensor $F_{\mu\nu}$ is used and is Taylor expanded to give the final equation.

The above expression simplifies the plaquette operator as

$$P_{\mu\nu}(x)=1-\frac{1}{6}g^2a^4\mathrm{Tr}F_{\mu\nu}^2-\frac{1}{72}g^2a^6\mathrm{Tr}F_{\mu\nu}(\partial_\mu^2+\partial_\nu^2)F_{\mu\nu}+O(a^8)+O(g^4a^6)\,. \tag{4.8}$$

Using the above plaquette operator, one arrives at the traditional Wilson action [8] for the gluons on lattice, viz.,

$$S_{\mathrm{Wil}}=\beta\sum_{x,\mu>\nu}(1-P_{\mu\nu}(x));\quad \beta=\frac{6}{g^2}\,. \tag{4.9}$$

The sum in the Eq. (4.9) runs over all the plaquettes of all orientations in the lattice. β is the single input parameter for QCD calculations involving only gluon fields. The value of the lattice spacing a depends on the bare coupling constant g^2. Larger values of β gives smaller lattice spacing. The bare coupling constant g^2 tends to zero at small distances or high energies which is equivalent to taking β to infinity.

The S_{Wil} term is gauge invariant and hence the lattice QCD calculations using Wilson action do not need any gauge fixing. The calculations are done with a non-zero lattice spacing a and a finite lattice volume V. Hence corrections must be applied to account for the fact that lattice spacing should be zero and volume infinite ideally.

The purely gluonic part of the continuum QCD action (first term in Eq. (3.4)) is

$$S_{\mathrm{cont}}=-\frac{1}{4}F_{\mu\nu}F^{\mu\nu}\,. \tag{4.10}$$

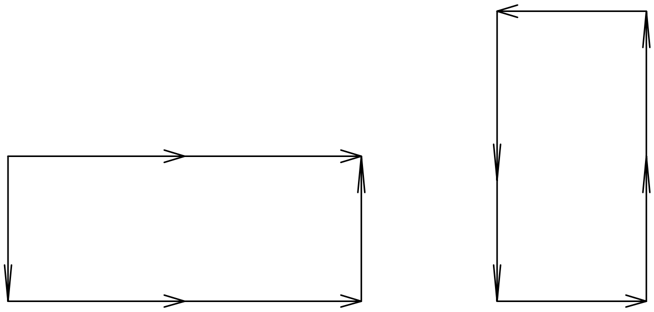

Figure 4.2: Rectangular plaquettes $R_{\mu\nu}$ on lattice.

The Wilson action differs from the continuous gluon action by terms which are $O(a^2)$ and $O(g^2a^2)$. The $O(a^2)$ terms can be removed by adding other products of links that form closed loops, known as Wilson loops. Considering the rectangular 1 × 2 loops (Fig. 4.2), they would have the expansion

$$\begin{aligned} R^{1\times2}_{\mu\nu} &= 1 - \frac{4}{6}g^2a^4\mathrm{Tr}F^2_{\mu\nu} - \frac{4}{72}g^2a^6\mathrm{Tr}(F_{\mu\nu}(4\partial^2_\mu + \partial^2_\nu)F_{\mu\nu}) - \ldots \\ R^{2\times1}_{\mu\nu} &= 1 - \frac{4}{6}g^2a^4\mathrm{Tr}F^2_{\mu\nu} - \frac{4}{72}g^2a^6\mathrm{Tr}(F_{\mu\nu}(\partial^2_\mu + 4\partial^2_\nu)F_{\mu\nu}) - \ldots . \end{aligned} \tag{4.11}$$

Adding the $R_{\mu\nu}$ and $P_{\mu\nu}$ terms gives the improved lattice action as, [9, 10]

$$\begin{aligned} S_{\mathrm{Imp}} &= \beta \sum_{x,\mu>\nu} \left\{ \frac{5}{3}(1 - P_{\mu\nu}) - \frac{1}{12}(1 - R^{1\times2}_{\mu\nu}) + \frac{1}{12}(1 - R^{2\times1}_{\mu\nu}) \right\} \\ &= a^4 \sum_{x,\mu>\nu} \left[\frac{1}{2}\mathrm{Tr}F^2_{\mu\nu} + O(a^4) + O(a^2g^2) \right] . \end{aligned} \tag{4.12}$$

In the continuum limit, the improved lattice action reduces to the continuum gluon action.

4.2.1 Mean Field Improvement

The link variables U_μ represent the gauge fields A_μ on the lattice related as shown by Eq. (4.2). The link variable can be Taylor-expanded about x to obtain

$$U_\mu(x) \approx 1 + iagA_\mu(x) - \frac{a^2g^2}{2}A^2_\mu(x) + \ldots . \tag{4.13}$$

The first two terms are lattice artifacts in the QCD action and give rise to quark-gluon vertices with two or more gluons. Contracting the two gluons in the third term produces tadpole diagrams.

For quantum fields, pairs of A_μ fields contracted with each other generate ultraviolet divergent factors of $\frac{1}{a^2}$ that precisely cancel the factors a [11]. As a result the contributions generated by the tadpole loops are suppressed only by powers of g^2, resulting in large renormalisations. Mean field improvement or tadpole improvement helps to largely compensate for these artifacts. Since the tadpole contributions are process independent, they can be measured in one quantity and then corrected for in all others.

Assuming that the lattice fields can be split into ultraviolet (UV) and infrared (IR) parts, mean field improvement suggests integrating out the UV part, i.e,

$$e^{iagA_\mu(x)} = e^{iag(A_\mu^{\mathrm{IR}}(x)+A_\mu^{\mathrm{UV}}(x))} \sim u_0 e^{iagA_\mu^{\mathrm{IR}}} \equiv u_O \tilde{U}_\mu(x)\,. \tag{4.14}$$

The link variables can be scaled by a constant $u_0 \leq 1$, leaving the theory gauge invariant. In such a case, every link variable U gets replaced by $\tilde{U}$ in all the lattice operators. These u_0's cancel a large part of the tadpole contributions, thus making the lattice operators and perturbation theory closer to the continuum behavior.

The mean link u_0 can be chosen to be real, since only the real part of the correlation functions is needed.

Generally the mean-field improvement parameter u_0 is chosen to be either the fourth root of the plaquette or the expectation value of the link in the Landau gauge. Both choices give nearly identical results on typical lattices and identical results in the continuum limit. In cases where gauge fixing is not needed, the mean-link is defined as

$$u_0 = (\mathcal{R}e\mathrm{Tr}\,\langle U_\Box\rangle)^{1/4}\ . \tag{4.15}$$

Hence the gluon action given in Eq. (4.12) can be tadpole improved by dividing each link U_μ by the mean link u_0 to yield [12]

$$S_{\,\mathrm{Imp}} = \beta \sum_{x,\mu>\nu} \left\{ \frac{5}{3}\left(1 - \frac{P_{\mu\nu}}{u_0^4}\right) - \frac{1}{12}\left(1 - \frac{R_{\mu\nu}^{1\times2}}{u_0^4}\right) + \frac{1}{12}\left(1 - \frac{R_{\mu\nu}^{2\times1}}{u_0^4}\right)\right\}\ . \tag{4.16}$$

To determine the mean-link u_0 self-consistently, it is computed numerically by initializing it to 1, then measuring it in a simulation and fine tuning the value used in action depending on the measured value. The mean-links are solely dependent on the lattice spacing and converge to 1 as the lattice spacing vanishes.

Introducing the mean links u_0 largely compensates for the tadpole contributions which spoil the weak-coupling perturbation theory. Without the tadpole improvement only approximately half of the $\mathcal{O}(a^2)$ are canceled [12].

4.3 Lattice Fermion Action

4.3.1 Naive Fermion Action

In Euclidean space-time the total QCD action is given by

$$S\,[A_\mu,\psi,\overline{\psi}] = \int d^4x\Big(-\frac{1}{4}F_{\mu\nu}F^{\mu\nu} + \overline{\psi}\,(\not{D}+m)\,\psi\Big) = S_G + S_F\,. \tag{4.17}$$

The quantity $\not{D}+m$ is the Dirac operator and the action is a sum of the gluonic and fermionic actions, S_G and S_F.

The gluonic and fermionic fields are made dimensionless on the lattice. The lattice points $(x+a\hat{\mu})$ will become $(x+\hat{\mu})$, since the fields are measured in units of lattice spacing a.

The Dirac (fermionic) action viz., $\overline{\psi}(\not{D}+m)\psi$ is discretized on lattice by replacing the covariant derivative with a symmetrised finite difference and including appropriate gauge links to give the lattice action. The gauge links U_μ contain the gluon fields A_μ and satisfy gauge invariance. Under such a scheme, the first term in the fermionic action becomes

$$\overline{\psi}\not{D}\psi = \frac{1}{2a}\overline{\psi}(x)\sum_\mu \gamma_\mu\left[U_\mu(x)\psi(x+\hat{\mu}) - U^\dagger(x-\hat{\mu})\psi(x-\hat{\mu})\right]. \tag{4.18}$$

Here a is the lattice spacing and the continuum Dirac action can be recovered in the limit $a \to 0$ by Taylor expansion of U_μ and $\psi(x+\hat{\mu})$ about x. The simplest fermion action, retaining only the leading terms in a is evaluated to be [5]

$$\begin{aligned} S_N &= m_q\sum_x \overline{\psi}(x)\psi(x) \\ &\quad +\frac{1}{2a}\sum_{x,\mu}\overline{\psi}(x)\gamma_\mu\Big[U_\mu(x)\psi(x+\hat{\mu})\psi - U^\dagger_\mu(x-\hat{\mu})\psi(x-\hat{\mu})] \\ &\equiv \sum_x \overline{\psi}(x)M_{xy}[U]\psi(y)\,. \end{aligned} \tag{4.19}$$

The interaction matrix M_{ij} is

$$M_{ij}[U] = m_q\delta_{ij} + \frac{1}{2a}\sum_\mu[\gamma_\mu U_{i,\mu}\delta_{i,j-\mu} - \gamma_\mu U^\dagger_{i-\mu,\mu}\delta_{i,j+\mu}]\,. \tag{4.20}$$

The γ matrices are Hermitian, $\gamma = \gamma^\dagger$ and satisfy the anti-commutator relation $\{\gamma_\mu,\gamma_\nu\} = 2\delta_{\mu\nu}$. The naive fermion action has errors of the order of $O(a^2)$. It preserves chiral symmetry. In the continuum limit it gives rise to 2^d fermions instead of

1. This “doubling problem” makes the action phenomenologically unacceptable. Various improvement schemes are available in literature [5, 6] to get around this doubling problem.

4.3.2 Wilson Fermion Action

Wilson [8] originally introduced an irrelevant dimension-five operator (“Wilson term”) to the naive fermion action (Eq. 4.19) which explicitly breaks the chiral symmetry at $\mathcal{O}(a)$. The irrelevant operator is given by $-\frac{1}{2}ra\triangle_\mu$. Adding this to the standard lattice fermion action gives the Wilson fermion action as

$$S_W = \overline{\psi}(x)\left[\sum_\mu\left(\not{D} - \frac{1}{2}ra\triangle_\mu\right) + m\right]\psi(x)\,, \tag{4.21}$$

where $\triangle_\mu$ is defined by

$$\triangle_\mu\psi(x) = \frac{1}{a^2}\left[U_\mu(x)\psi(x+\hat{\mu}) + U^\dagger_\mu(x-\hat{\mu})\psi(x-\hat{\mu}) - 2\psi(x)\right]. \tag{4.22}$$

The Wilson action in terms of link variables is written as

$$\begin{aligned} S_{\rm W} &= \left(m_q + \frac{4r}{a}\right)\sum_x \overline{\psi}(x)\psi(x) + \frac{1}{2a}\sum_{x,\mu}\overline{\psi}(x)\big[(\gamma_\mu - r)U_\mu(x)\psi(x+\hat{\mu}) \\ &\quad -(\gamma_\mu + r)U^\dagger_\mu(x-\hat{\mu})\psi(x-\hat{\mu})\big] \\ &\equiv \sum_{x,y}\overline{\psi}^L_x M^W_{xy}\psi^L_y\,. \end{aligned} \tag{4.23}$$

M^W_{xy} is the interaction matrix for the Wilson action and is written as

$$M^W_{xy}[U]a = \delta_{xy} - \kappa\sum_\mu\left[(r-\gamma_\mu)U_{x,\mu}\delta_{x,y-\mu} + (r+\gamma_\mu)U^\dagger_{x-\mu,\mu}\delta_{x,y+\mu}\right], \tag{4.24}$$

with a field renormalization

$$\begin{aligned} \kappa &= 1/(2m_q a + 8r) \\ \psi^L &= \psi/\sqrt{2\kappa}\,. \end{aligned} \tag{4.25}$$

The Wilson parameter r is generally taken as 1 and the quark mass is then given as

$$m_q a = \frac{1}{2}\left(\frac{1}{\kappa} - \frac{1}{\kappa_c}\right). \tag{4.26}$$

κ_c is the “critical” value of κ where the quark mass vanishes.

In the continuum limit the Wilson action becomes

$$S_{\mathrm{W}} = \int d^4x \overline{\psi}(x) \left(\not{D} + m - \frac{ar\not{D}^2}{2} \right) \psi(x) + \mathcal{O}(a^2)\,. \tag{4.27}$$

While lifting the doubling problem with a second derivative, the Wilson term introduces $\mathcal{O}(a)$ errors into the fermionic action. Though computationally inexpensive, its approach to the continuum is slow. The introduction of $\mathcal{O}(a)$ errors makes it necessary for the simulations to be performed at lattice spacing typically less than 0.1 fm and usage of very large four dimensional lattices in order to provide reasonable physical simulation volumes.

4.4 FLIC Fermion Action

4.4.1 Clover Action

The computational expense of lattice calculations increases with decrease in lattice spacing. Many improvements to quark action are suggested and implemented [13, 14].

The “clover” action introduced by Sheikhholaslami and Wohlert [14] introduces an additional irrelevant dimension-five operator to the standard Wilson action (Eq. 4.23). The clover action is given as

$$S_{\mathrm{SW}} = S_{\mathrm{Wil}} - \frac{iaC_{\mathrm{SW}}r}{4} \overline{\psi}(x)\sigma_{\mu\nu}F_{\mu\nu}\psi(x)\,. \tag{4.28}$$

In the above equation, S_{Wil} is the standard Wilson equation and C_{SW} is the clover coefficient which can be tuned to remove $\mathcal{O}(a)$ errors. Nonperturbative (NP) $\mathcal{O}(a)$ improvement tunes the clover coefficient to all powers in g^2 and displays excellent scaling [15, 16]. The linear behavior of the NP-improved clover actions with a^2 indicates that $\mathcal{O}(a)$ are removed.

However this formulation of the clover action is susceptible to problems due to exceptional configurations at low quark masses. Chiral symmetry breaking in the clover fermion action introduces an additive mass renormalization into the Dirac operator that can give rise to singularities in quark propagators at small quark masses. This prevents simulation at low quark masses and limits the clover action to coarse lattice sizes [17, 18]. The plaquette version of $F_{\mu\nu}$ in the clover action has $\mathcal{O}(a^2)$ errors, which can lead to errors of the order of 10% in the topological charge even on very smooth configurations [19].

4.4.2 Fat Link Irrelevant Clover Action

The idea of using fat links in the fermion action was explored by many groups [20, 17]. DeGrand *et al* [21, 22] showed that the exceptional configurations problem can be significantly reduced by using a fat-link (FL) clover action. J. M. Zanotti *et al* have used fat links to develop fermion actions with $\mathcal{O}(a)$ improvement [23, 24].

Fermion doublers of the naive theory are removed by the Wilson term at tree level. Instead of applying techniques to estimate the renormalization of the improvement coefficients induced by the gauge fields of QCD the gauge fields can be modified to suppress renormalizations such that tree-level knowledge of improvement coefficients is adequate.

There are many methods for minimizing short-distance fluctuations from gauge field configurations including APE smearing and HYP-smearing [25, 26].

The central feature of FLIC fermions is to construct the fermion action using two sets of gauge fields. In the lattice operators providing the relevant dimension-four operators of the continuum action, one works with the untouched gauge fields generated directly by Monte Carlo methods. The smoothed gauge fields are introduced only in the purely irrelevant lattice operators having dimension five or more.

The FLIC fermion action reduces the exceptional configuration problem of fat-link actions, while retaining short-distance quark interactions in the relevant operators of the fermion action. The improvement in the condition number of the FLIC fermion matrix allows more rapid calculations of fermion propagators and more efficient access to the chiral limit of full QCD [27].

Fat links [17, 21] are created by averaging or smearing links on the lattice with their nearest neighbors in a gauge covariant manner (APE smearing). The smearing procedure replaces a link U_μ with a sum of the link and α times its staples, i.e.,

$$\begin{aligned} U_\mu(x) \rightarrow U'_\mu(x) &= (1-\alpha)U_\mu(x) + \frac{\alpha}{6}\sum_{\nu=1,\nu\neq\mu}^{4}\Big[U_\nu(x)U_\mu(x+\nu a)U_\nu^\dagger(x+\mu a)\Big] \\ &\quad + U_\nu^\dagger(x-\nu\alpha)U_\mu(x-\nu a)U_\nu(x-\nu a+\mu a)\,, \end{aligned} \tag{4.29}$$

followed by projection back to $SU(3)$. A unitary matrix U_μ^{FL} is chosen to maximize the trace

$$\mathcal{R}e\,\mathrm{Tr}(U_\mu^{\mathrm{FL}}U_\mu^{'\dagger})\,, \tag{4.30}$$

by iterating over the three diagonal $SU(2)$ subgroups of $SU(3)$. Performing iterations over these subgroups gives gauge invariance up to seven significant figures. The combined procedure of smearing and projection is repeated to create a fat link. The mean-field improved FLIC action [23] now is

$$S_{\mathrm{SW}}^{\mathrm{FL}} = S_{\mathrm{W}}^{\mathrm{FL}} - \frac{igC_{\mathrm{SW}}\kappa r}{2(u_0^{\mathrm{FL}})^4}\overline{\psi}(x)\sigma_{\mu\nu}F_{\mu\nu}\psi(x)\,. \tag{4.31}$$

In the above equation $F_{\mu\nu}$ is constructed using fat links, u_0^{FL} is the mean-field improvement parameter or mean-link defined as the fourth root of the plaquette,

$$u_0 = \left(\frac{1}{3}\mathcal{R}\mathrm{tr}\,\langle U_{\square}\rangle\right)^4\,. \tag{4.32}$$

The mean-field improved Fat-link Irrelevant Wilson action is

$$\begin{aligned} S_{\mathrm{W}}^{FL} = \sum_x \overline{\psi}(x)\psi(x) \quad &+ \quad \kappa\sum_{x,\mu}\overline{\psi}(x)\Big[\gamma_\mu\Big(\frac{U_\mu(x)}{u_0}\psi(x+\hat{\mu}) - \frac{U_\mu^\dagger(x-\hat{\mu})}{u_0}\psi(x-\hat{\mu})\Big) \\ &- \quad r\Big(\frac{U_\mu^{\mathrm{FL}}(x)}{u_0^{\mathrm{FL}}}\psi(x+\hat{\mu}) + \frac{U_\mu^{\mathrm{FL}\dagger}(x-\hat{\mu})}{u_0^{\mathrm{FL}}}\psi(x-\hat{\mu})\Big)\Big]\,, \end{aligned} \tag{4.33}$$

with $\kappa = 1/(2m + 8r)$. The standard value for r is taken as 1. The notation used is the Sakurai representation of the Dirac matrices, which are hermitian.

The FLIC fermion action has very impressive convergence rates for matrix inversion, providing cost effective access to light quark mass region, closer to physical values. This will give valuable insight into the chiral behavior of hadron properties.

4.5 Expectation Values Of Observables

Expectation values of observables are calculated on the lattice by creating an ensemble of lattice gauge field configurations $\{U^{[i]}\}$ using Monte Carlo methods [5]. A configuration $U^{[i]}$ is generated from the preceding one using Monte Carlo probability methods. The probability of generating a configuration $U^{'}$ from another U depends on the value of $\beta = 6/g^2$, the parameter that fixes the lattice spacing. The initial configuration is chosen to be “cold” when all the links are set to unity, or ”hot” when each link is set randomly from a $SU(3)$ matrix.

Physical observables are obtained via expectation values

$$\langle\, O(....)\,\rangle = \frac{1}{Z}\int \mathcal{D}A_\mu O e^{-S} \simeq \frac{1}{N}\sum_i O\Big(...[U^{[i]}]\Big)\,, \tag{4.34}$$

where N is the number of configurations generated. The operator O can be any combination of operators expressed as time-ordered product of the quark and gluon fields. Wick's theorem can be used to contract fields. Hence the quark fields can be re-written in terms of quark propagators, removing any dependence on the quark fields as dynamical variables. Extraction of physical observables on lattice is discussed in more detail in Chapter 6.

The standard lattice definition of QCD implies that the chance of selecting two gauge-equivalent configurations is negligible. Hence calculation of physical observables is unaffected by arbitrary gauge transformations on the configurations. As a result there is no need for any gauge fixing while computing physical or gauge-invariant quantities on the lattice.

Physical quantities that are extracted like mass and form factors are renormalization point independent. For the calculation of form factors we work with a conserved vector current and ensure that its lattice version is also strictly conserved. Hence the form factors do not need any renormalization. Therefore for all of the lattice QCD calculation results considered here, we do not require any renormalization procedure.

Chapter 5

Chiral Perturbation theory

5.1 Introduction

Chiral Perturbation theory (χPT) is a model independent tool to study QCD at low energies. It is an effective field theory with low-energy degrees of freedom. The electromagnetic properties of baryons have been studied extensively using χPT, both in quenched and partially quenched approximations [28, 29].

χPT provides a framework for understanding the low energy manifestation of the strong interactions. It predicts the leading non-analytic quark mass dependence in the chiral limit of the hadron observables in terms of phenomenological parameters. In χPT one constructs an effective Lagrangian for the low energy sector which has hadronic degrees of freedom, and contains all the symmetries of the QCD Lagrangian. Electromagnetic properties like charge radii and magnetic moments are expanded about vanishing quark mass with coefficients that can be determined phenomenologically. We compare our lattice simulation results for the octet baryons with the predictions of the Quenched chiral perturbation theory (QχPT).

5.2 Chiral Symmetry

The QCD Lagrangian (Eq. 3.4) can be written in a compact form as

$$\mathcal{L}_{\mathrm{QCD}} = -\frac{1}{4} F_a^{\mu\nu} F_{\mu\nu}^a + \overline{\psi}(x)(i\not{D} - m)\psi(x)\,. \tag{5.1}$$

The QCD Lagrangian which contains all dynamical content of the theory is invariant under local $SU(3)_{\mathrm{color}}$ transformations. It is renormalizable, i.e., infinities which arise in QCD calculations can be handled in a systematic manner to give a finite result.

The quark wave function ψ can be written in terms of left and right handed wave functions, ψ_L and ψ_R, defined as

$$\begin{aligned} \psi_L &= \frac{1}{2}(1-\gamma_5)\psi \\ \psi_R &= \frac{1}{2}(1+\gamma_5)\psi \,. \end{aligned} \tag{5.2}$$

The Lagrangian written in terms of the left and right handed quark wave functions is

$$\mathcal{L}_{\mathrm{QCD}} = -\frac{1}{4}F_a^{\mu\nu}F^a_{\mu\nu}+\overline{\psi}_L(x)i\not{D}\psi_L(x)+\overline{\psi}_R(x)i\not{D}\psi_R(x)-\overline{\psi}_L(x)m\psi_R(x)-\overline{\psi}_R(x)m\psi_L(x)\,. \tag{5.3}$$

The left and right handed terms are mixed only through the quark mass matrix m. When the mass is zero, the Lagrangian is invariant under $SU(N_f)_L \otimes SU(N_f)_R$ transformations, N_f being the number of quark flavors. The quark wave functions under such transformations mix among themselves,

$$\begin{aligned} \psi_L(x) &\to g_L\psi_L(x) \\ \psi_R(x) &\to g_R\psi_R(x)\,, \end{aligned} \tag{5.4}$$

where (g_L, g_R) is an element of the group $SU(N_f)_L \otimes SU(N_f)_R$.

The invariance of the Lagrangian under such a transformation is called “chiral symmetry”. It is an approximate symmetry useful for very low quark masses. In two flavor QCD this is a good symmetry since the masses of the u and d quarks are small. Three flavor QCD includes the strange quark with larger mass, hence the chiral expansions must be treated cautiously. In 3-flavor QCD, chiral symmetry of the massless QCD Lagrangian gives rise to 16 conserved Noether currents, viz.,

$$J_X^{\mu a} = \overline{\psi}_X(x)\gamma^\mu\frac{\lambda^a}{2}\psi_X(x)\,, \tag{5.5}$$

where $a = 1...8$ and $X = L, R$. The 16 conserved currents can be written in terms of conserved Vector and Axial currents, i.e.,

$$\begin{aligned} J_V^{\mu a} &= J_L^{\mu a} + J_R^{\mu a} \\ J_A^{\mu a} &= J_L^{\mu a} - J_R^{\mu a}\,. \end{aligned} \tag{5.6}$$

Corresponding to the conserved Vector and Axial currents, there are 16 conserved charges,

$$\begin{aligned} Q_V^a &= \int d^3x J_V^{0a} \\ Q_A^a &= \int d^3x J_A^{0a}\,. \end{aligned} \tag{5.7}$$

These charges are the generators of the vector and axial symmetries of the QCD Lagrangian.

The massless QCD vacuum is not chirally symmetric. The vacuum state $|0\rangle$ contains an arbitrary number of massless pseudo-scalar particles known as Goldstone bosons. The $SU(N_f)_L \otimes SU(N_f)_R$ symmetry of the QCD Lagrangian is dynamically broken to $SU(N_f)_V$ by the vacuum state $|0\rangle$ and this produces massless Goldstone bosons. For the three flavor symmetry there are 16 generators of the chiral symmetry, 8 of which are broken in the dynamical breaking to $SU(3)_V$. Hence a (nearly massless) octet of pseudo-scalar Goldstone bosons appears. These eight particles are created by the axial currents and obey

$$\langle 0|J_A^{\mu a}(0)|\pi_b(p)\rangle = i f_\pi p^\mu \delta_b^a \,, \tag{5.8}$$

where π_a is the a^{th} Goldstone boson field and f_π is the pseudoscalar decay constant. Experimentally f_π is found to be 93 MeV [30].

If the quarks were massless the chiral symmetry would be an exact symmetry of the QCD Lagrangian and the Goldstone bosons produced by chiral symmetry breaking would be completely massless. The small quark masses result in the eight pseudo-scalar Goldstone bosons acquiring small masses (meson-octet).

5.3 Chiral Lagrangian

The chiral Lagrangian is constructed to represent all the symmetries of the QCD Lagrangian. Hence it contains both the symmetric and symmetry breaking terms. In the chiral Lagrangian, written as sum of the right and left handed quark wave functions, Eq. (5.3), the first three terms are the symmetric terms while the last two are the symmetry breaking terms. The symmetric part is symmetric under the chiral Lie group $SU(N_f)_L \otimes SU(N_f)_R$. The chiral symmetry is spontaneously broken, which gives rise to massless Goldstone bosons (eight mesons for $SU(3)_f$ symmetry).

The full chiral Lagrangian is written as a sum of the Lagrangians of the Meson-Baryon sector and the Meson sector [31], i.e.,

$$\mathcal{L}_{\mathrm{eff}} = \mathcal{L}_{\mathrm{MB}} + \mathcal{L}_{\mathrm{M}} \,. \tag{5.9}$$

To construct the effective chiral Lagrangian for the meson-octet, it is necessary to introduce the unitary matrix U that contains the 8 Goldstone boson (meson-octet) fields. This matrix is defined as [32]

$$U = e^{2i\phi/f} \,, \tag{5.10}$$

where f is the pseudoscalar decay constant with the dimensions of mass and ϕ is a 3×3 matrix, defined in terms of the eight Gell-Mann matrices, λ_a as

$$\phi = \frac{1}{2}\lambda_a\pi^a = \frac{1}{\sqrt{2}}\begin{pmatrix} \frac{1}{\sqrt{6}}\eta + \frac{1}{\sqrt{2}}\pi^0 & \pi^+ & K^+ \\ \pi^- & \frac{1}{\sqrt{6}}\eta - \frac{1}{\sqrt{2}}\pi^0 & K^0 \\ K^- & \overline{K}^0 & -\frac{2}{\sqrt{6}}\eta \end{pmatrix} . \tag{5.11}$$

In the above equation, π^a represent the eight Goldstone boson fields. U transforms linearly under $SU(3)_L \otimes SU(3)_R$. Under the global chiral transformation of the fermion fields of the type in Eq. (5.4), the boson fields U transform as

$$U \to U' = e^{-i\alpha_L^a\lambda_a/2}Ue^{i\alpha_R^a\lambda_a/2} = g_L U g_R^\dagger . \tag{5.12}$$

In the low energy sector of QCD, meson momenta and quark masses are assumed to be small. Hence the effective Lagrangian can be expressed as a Taylor expansion about $p_\mathrm{M}/\Lambda_\chi$ and $\mu m/\Lambda_\chi$. Here p_M is the momenta of the meson and Λ_χ is the scale of chiral symmetry breaking. Generally $\Lambda_\chi \simeq 4\pi f \simeq 1\mathrm{GeV}$ from renormalization arguments.

Expanding about the mass term $\mu m/\Lambda_\chi$ produces the symmetry breaking terms giving rise to the Goldstone boson masses. The parameter μ is determined phenomenologically and relates the quark and meson masses.

The chiral Lagrangian for the meson sector retains only terms with even numbers of derivatives to ensure Lorentz invariance. Hence the effective Lagrangian for the meson sector can be expressed as,

$$\mathcal{L}_{\chi\mathrm{M}} = \mathcal{L}_\mathrm{M}^{(2)} + \mathcal{L}_\mathrm{M}^{(4)} + \mathcal{L}_\mathrm{M}^{(6)} + \ldots\ldots . \tag{5.13}$$

where $\mathcal{L}_\mathrm{M}^{(d)}$ contains terms with d derivatives (or d powers of momentum) and $d/2$ powers of the quark mass matrix.

The first term in the above equation includes the kinetic energy of the mesons and meson-mass terms and can be expressed as a sum of symmetric and a symmetry-breaking terms [33], i.e.,

$$\mathcal{L}_M^{(2)} = \frac{f^2}{4}\mathrm{Tr}\left[\partial^\mu U^\dagger \partial^\mu U\right] + \frac{f^2}{2}\mathrm{Tr}\left[\mu m\left(U + U^\dagger\right)\right] . \tag{5.14}$$

The second term in the above equation is the symmetry breaking term and gives rise to leading contribution to the pseudo-Goldstone boson masses.

The chiral Lagrangian for the meson-baryon interaction, $\mathcal{L}_\mathrm{MB}$ can be obtained by defining a matrix B containing the octet baryon fields and a tensor field T^μ_{abc} to represent the decuplet baryon fields. The octet baryon field B is given by [34]

$$B = \frac{1}{\sqrt{2}}\lambda_a B^a = \begin{pmatrix} \frac{1}{\sqrt{6}}\Lambda + \frac{1}{\sqrt{2}}\Sigma^0 & \Sigma^+ & p \\ \Sigma^- & \frac{1}{\sqrt{6}}\Lambda - \frac{1}{\sqrt{2}}\Sigma^0 & n \\ \Xi^- & \Xi^0 & -\frac{2}{\sqrt{6}}\Lambda \end{pmatrix}, \tag{5.15}$$

where B^a represent the 8 baryon fields.

The Rarita-Schwinger field tensor T^μ_{abc} contains the decuplet baryon fields and obeys the relation $\gamma_\mu T^\mu_{abc} = 0$. The $3 \times 3 \times 3$ matrix T_{abc} is given by [35]

$$\begin{pmatrix} \Delta^{++} & \frac{1}{\sqrt{3}}\Delta^+ & \frac{1}{\sqrt{3}}\Sigma^{*+} \\ \frac{1}{\sqrt{3}}\Delta^+ & \frac{1}{\sqrt{3}}\Delta^0 & \frac{1}{\sqrt{6}}\Sigma^{*0} \\ \frac{1}{\sqrt{3}}\Sigma^{*+} & \frac{1}{\sqrt{6}}\Sigma^{*0} & \frac{1}{\sqrt{3}}\Xi^{*0} \end{pmatrix} \begin{pmatrix} \frac{1}{\sqrt{3}}\Delta^+ & \frac{1}{\sqrt{3}}\Delta^0 & \frac{1}{\sqrt{6}}\Sigma^{*0} \\ \frac{1}{\sqrt{3}}\Delta^0 & \Delta^- & \frac{1}{\sqrt{3}}\Sigma^{*-} \\ \frac{1}{\sqrt{6}}\Sigma^{*0} & \frac{1}{\sqrt{3}}\Sigma^{*-} & \frac{1}{\sqrt{3}}\Xi^{*-} \end{pmatrix} \begin{pmatrix} \frac{1}{\sqrt{3}}\Sigma^{*+} & \frac{1}{\sqrt{6}}\Sigma^{*0} & \frac{1}{\sqrt{3}}\Xi^{*0} \\ \frac{1}{\sqrt{6}}\Sigma^{*0} & \frac{1}{\sqrt{3}}\Sigma^{*-} & \frac{1}{\sqrt{3}}\Xi^{*-} \\ \frac{1}{\sqrt{3}}\Xi^{*0} & \frac{1}{\sqrt{3}}\Xi^{*-} & \Omega^- \end{pmatrix}. \tag{5.16}$$

In the above tensor, the three matrices indicate the values of c being equal to 1, 2 and 3. In each matrix, the rows are labeled by $a = 1, 2, 3$ and the columns by $b = 1, 2, 3$.

It is more convenient to use an alternative representation of the Goldstone bosons, given by

$$\xi \equiv (U)^{1/2} = e^{i\phi/f}. \tag{5.17}$$

Under chiral transformation, this field transforms as

$$\xi \to g_L \xi g_H^\dagger, \tag{5.18}$$

where g_H is a member of the chiral group given by

$$g_H = \sqrt{g_R U g_L^\dagger g_L}\,\sqrt{U^\dagger} = \sqrt{g_L U^\dagger g_R^\dagger g_R}\,\sqrt{U}. \tag{5.19}$$

The matrix g_H is a function of the pseudo-Goldstone boson fields, $U(x)$. The octet and decuplet fields transform under $SU(3)_L \otimes SU(3)_R$ according to

$$\begin{aligned} B &\to g_H B g_H^\dagger, \\ T^{abc} &\to g_H^{aa\prime} g_H^{bb\prime} g_H^{cc\prime} T^{a\prime b\prime c\prime}. \end{aligned} \tag{5.20}$$

The axial vector current A_μ transforms under the action of the same group as

$$A_\mu \to g_H A_\mu g_H^\dagger. \tag{5.21}$$

A generalization of the free Dirac Lagrangian allows one to write the free field Lagrangian for the octet and the decuplet fields as

$$\mathcal{L}_{\text{oct}} = \mathrm{Tr}\left[\overline{B}\left(i\gamma^\mu\partial_\mu - \mathcal{M}_B\right)B\right], \tag{5.22}$$

$$\mathcal{L}_{\text{dec}} = \mathrm{Tr}\left[\overline{T}^\mu\left(i\gamma^\mu\partial_\mu - \mathcal{M}_T\right)T_\mu\right], \tag{5.23}$$

where $\mathcal{M}_B$ and $\mathcal{M}_T$ are the octet and decuplet masses respectively, which are degenerate in the $SU(3)$ limit.

The complete χPT Lagrangian for the low energy sector looks like

$$\mathcal{L}_\chi = \mathcal{L}^{(2)}_{\rm M} + \mathcal{L}^{(4)}_{\rm M} + \ldots\ldots. + \mathcal{L}^{(1)}_{\rm MB} + \mathcal{L}^{(2)}_{\rm MB} + \mathcal{L}^{(3)}_{\rm MB} + \mathcal{L}^{(4)}_{\rm MB} + \ldots\ldots. \,. \tag{5.24}$$

The lowest order chiral Lagrangian for octet-decuplet baryons interacting with the Goldstone bosons is given by [33, 36]

$$\begin{aligned}
\mathcal{L}^{(1)}_{\rm MB} &= \mathcal{L}^{(1)}_{\rm oct} + \mathcal{L}^{(1)}_{\rm dec} \\
&= {\rm Tr}\left(\overline{B}(i\gamma^\mu\partial_\mu - \mathcal{M}_B)B\right) + D\,{\rm Tr}\left(\overline{B}\gamma_\mu\gamma_5\{A^\mu, B\}\right) \\
&\quad +F\,{\rm Tr}\left(\overline{B}\gamma_\mu\gamma_5\,[A^\mu, B]\right) \\
&\quad +\overline{T}^\mu(i\gamma^\mu\partial_\mu - \mathcal{M}_T)T_\mu + \mathcal{C}\left(\overline{T}^\mu A_\mu B + \overline{B}A_\mu T^\mu\right) \\
&\quad +\mathcal{H}\left(\overline{T}^\mu\gamma_\nu\gamma_5 A^\nu T_\mu\right)\,.
\end{aligned} \tag{5.25}$$

In the above equation the first and the fourth terms are the free octet and decuplet field Lagrangians respectively. The second and third terms represent the meson-octet interaction. The axial vector-coupling g_A is the sum of the axial coupling constants D and F. The fifth term is the octet-decuplet interaction term with coupling constant $\mathcal{C}$. The last term with coupling constant $\mathcal{H}$ is the meson-decuplet interaction term. All the coupling constants must be determined phenomenologically.

The symmetry breaking terms in the meson-baryon sector due to non zero quark masses appear only in the higher order $\mathcal{L}_{\rm MB}$ terms. These terms include the quark mass matrix m and hence the baryon masses are no longer degenerate.

5.4 Form Factors in Chiral Perturbation Theory

The calculation of electromagnetic properties using the chiral Lagrangian is discussed in detail in the literature [37, 38, 39].

Generally the Sachs forms of the electric and magnetic form factors, $\mathcal{G}_E(q^2)\ \mathcal{G}_M(q^2)$ are calculated. The 4-vector q is the momentum transfer. The charge radius and magnetic moment can be extracted from the form factors using the following relations,

$$\begin{aligned}
\langle r^2_{\rm E}\rangle &= -6\frac{d}{dq^2}\mathcal{G}_E(q^2)\bigg|_{q^2=0}\,, \\
\vec{\mu} &= \mathcal{G}_M(0)\frac{e}{2M_B}\,,
\end{aligned} \tag{5.26}$$

where M_B is the mass of the baryon. In the Breit frame the energy part of the four vector momentum, q^0 is zero. Hence in this frame the photon interactions with mesons and baryons transfer only momentum and not energy. In this frame $G(q^2)$ is the Fourier transform of the charge distribution.

The form factors are related to the electromagnetic current derived from the chiral Lagrangian. For the baryons with $SU(3)$ symmetry, the chiral expansions for the charge radius and magnetic moment are given by [38, 37]

$$\begin{aligned} \langle r_B^2 \rangle &= \delta_B + \sum_{X=\pi,K} \frac{6\alpha_B^X}{16\pi^2 f_\pi^2} \ln\left(\frac{m_X}{\lambda}\right) + \ldots. , \\ \mu_B &= \gamma_B + \sum_{X=\pi,K} \beta_B^X \frac{m_N}{8\pi^2 f_\pi^2} m_X + \ldots. . \end{aligned} \tag{5.27}$$

In the above set of equations B labels the baryon, λ is the scale of the dimensional regularization and m_N is the nucleon mass. δ_B and γ_B contain the analytic part of the chiral expansion. Coefficients of the analytic terms are not constrained by chiral symmetry. The summation in the non-analytic part of the chiral expansion is over all the possible virtual meson-baryon transitions.

The meson cloud that surrounds a baryon has its origin in the short lived meson-baryon intermediate states. For example,the proton can have a short-lived virtual transitions in any of the following channels, $p \rightarrow n\pi^+$, $p \rightarrow \Delta^{++}\pi^-$ or $p \rightarrow \Sigma^0 K^+$ as well as many others illustrated in Fig. 5.1. It is the presence of the meson cloud that gives rise to the non-analytic behavior of the electromagnetic observables. For a proper understanding of the chiral behavior, the chiral coefficients in the chiral expansion of observables have to be computed for each of the virtual transition channels.

5.5 Quenched Chiral Perturbation Theory

Separation of the valence and sea quark-loop contributions to the meson cloud enables one to compare with the quenched approximation where the contribution from the sea quarks is ignored. Diagrammatic methods to calculate the meson cloud contributions and the formal theory of the quenched chiral perturbation theory are well discussed in literature. [40, 41, 42]. Calculation of quenched chiral coefficients for charge radii in terms of phenomenologically fixed constants is done by Arndt *et al* for both the octet and the decuplet baryons [28, 29]. Quenched chiral coefficients have been calculated by Leinweber and Savage [43, 46] for the individual quark sector contributions and at the baryon level. We use the chiral coefficients in [43] to compare our results with theoretical predictions. Here we give a brief review of the calculation and interpretation

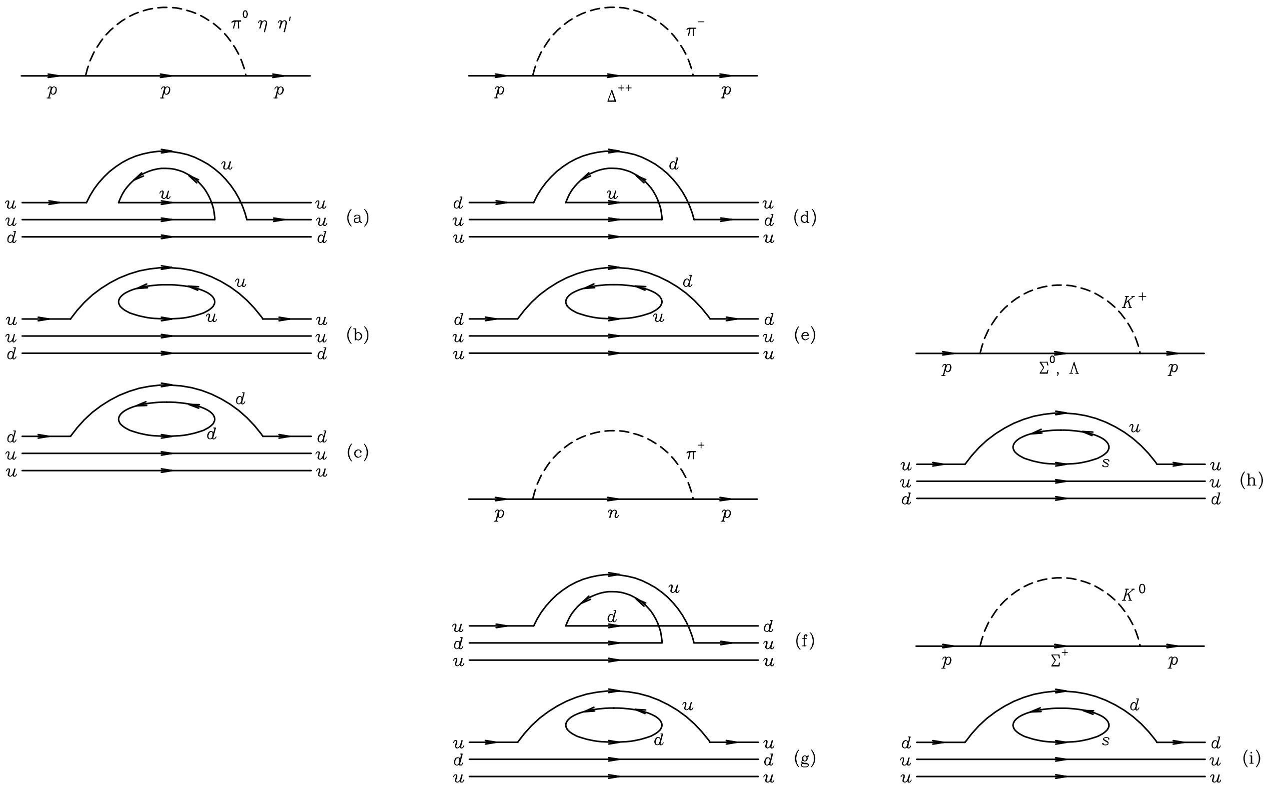

Figure 5.1: The pseudo-Goldstone meson cloud of the proton and associated quark flow diagrams.

of the chiral coefficients.

The effective field theory formalism of quenched chiral perturbation theory (QχPT) predicts significant contributions to the charge radii which have their origin in virtual meson-baryon loop transitions. These loops give rise to contributions which have a non-analytic dependence on the quark mass or squared pion mass. While the absence of sea-quark loops generally acts to suppress the magnitude coefficients of these terms (and occasionally the sign is reversed), there are several channels in which these contributions remain significant.

The leading nonanalytic (LNA) and next-to-leading nonanalytic (NLNA) behavior of charge distribution radii in full QCD are

$$\begin{aligned} \langle r_E^2 \rangle \;=\; & \frac{1}{16\pi^2 f^2} \sum_i \left[5\beta_i \log\left(\frac{m_i^2}{\mu^2}\right) - 10\beta_i' \mathcal{G}(m_i, \Delta, \mu) \right. \\ & \left. + c_0 + c_2\, m_i^2 + c_4\, m_i^4 \ldots \right] . \end{aligned} \tag{5.28}$$

Here the sum over i includes the π and K pseudoscalar mesons. The contributions of the various charge states of these mesons are contained in the coefficients β and β' reflecting electric charge and $SU(3)$ axial couplings, D, F and C. In quenching the theory, the coefficients β and β' are modified to reflect the absence of sea-quark loops.

The first term arises from octet baryon to octet-baryon – meson transitions. Thus charge radii are characterized by a logarithmic divergence [44] in the chiral limit ($m_\pi^2 \to 0$). In this simple form, the mass splittings between baryon octet members is neglected.

The second term of Eq. (5.28) arises from octet baryon to decuplet-baryon – meson transitions. As the splitting between the baryon octet and decuplet does not vanish in the chiral limit, the mass splitting, $\Delta = M_\Delta - M_N$, between the nucleon and Δ for example, plays an important role. The function $\mathcal{G}(m_i, \Delta, \mu)$ is

$$\begin{aligned} \mathcal{G}(m, \Delta, \mu) = & \log\left(\frac{m_i^2}{\mu^2}\right) - \\ & \frac{\Delta}{\sqrt{\Delta^2 - m_i^2}} \log \frac{\Delta - \sqrt{\Delta^2 - m_i^2 + i\epsilon}}{\Delta + \sqrt{\Delta^2 - m_i^2 + i\epsilon}} . \end{aligned} \tag{5.29}$$

$$\tag{5.30}$$

As the tadpole graph contributing to the LNA term of charge radii in full QCD vanishes in quenched QCD [28], the coefficients β and β' for charge radii are identical to those for magnetic moments in quenched QCD [45, 46]. Figure 5.2 displays the nonanalytic contributions from QχPT as given in Eq. (5.28), plotted for the sample case of the proton. In this case, the values of β and β' are $-\frac{4}{3}D^2$ and $-\frac{1}{6}C^2$ respectively [45, 46]. Here the axial couplings D and C are related by $C = 2D$ and D is taken as 0.76. The scale μ^2 is taken to be 1 GeV^2 and serves only to define c_0.

Because these nonanalytic contributions are complemented by terms analytic in the quark mass or pion-mass squared, the slope and curvature at large m_π^2 of these contributions is not significant. What is significant is the curvature at small m_π^2 and we see that this curvature is dominated by the LNA term. Here there is no mass splitting to mask the effects of dynamical chiral symmetry breaking. Thus, we will examine the extent to

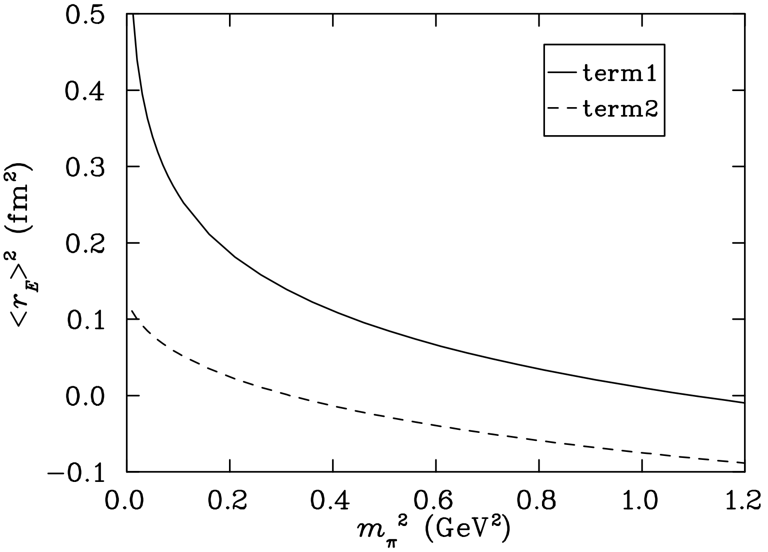

Figure 5.2: The leading (upper curve) and next-to-leading (lower curve) nonanalytic contributions to the charge radius of the proton as given by quenched chiral perturbation theory in Eq. (5.28).

which our simulation results are consistent with the LNA behavior of QχPT.

The coefficient β is related to the coefficient of the leading non-analytic (LNA) contribution to the magnetic moment, χ, via the relation [45]

$$\beta \frac{m_N}{8\pi f_\pi^2} = \chi \, . \tag{5.31}$$

The coefficients χ have been determined for octet baryons and their individual quark sector contributions in Ref. [45] and numerical values are reproduced in Tables A.38 and A.39 for ready reference.

Since $m_\pi^2 < 1$ GeV^2 in our simulations, the logarithmic term is negative for all quark masses considered here. Hence, the charge radius will exhibit a logarithmic divergence in chiral limit to either positive or negative infinity, depending on the whether β (or χ) is negative or positive respectively.

In the quenched approximation, the flavor-singlet η' meson remains degenerate with the pion and makes important contributions to quenched chiral nonanalytic behavior. The neutrality of its charge prevents it from contributing to the coefficients of Tables A.38 and A.39. However, the double hair-pin diagram in which the vector current couples to the virtual baryon intermediary does give rise to chirally-singular behavior. However the relatively small couplings render these contributions small at the quark masses probed here.

Similarly, it is interesting to compare our results with the LNA and NLNA terms of χPT which survive to some extent in QχPT. The expansion of baryon magnetic moment about the chiral limit can be written as [47]

$$\begin{aligned} \mu_B &= a_0^B + a_2^B m_\pi^2 + a_4^B m_\pi^4 + \dots \\ & \quad \chi_B I_\pi + \dots . & (5.32) \\ & & (5.33) \end{aligned}$$

As for the charge radii, the NLNA contributions provide little curvature [47] and we turn our attention to the LNA contributions [45]. These LNA contributions to baryon magnetic moments have their origin in couplings of the electromagnetic current to the virtual meson propagating in the intermediate meson-baryon state.

For virtual pion transitions, the LNA terms have the very simple form $\chi\, m_\pi \sim {m_q}^{1/2}$, with values for χ as summarized in Tables A.38 and A.39. While this contribution is finite in the chiral limit, the rate of change of this contribution does indeed diverge in the chiral limit. The less singular nature of this contribution should allow its contributions to be observed at larger pion masses, making magnetic moments an excellent observable to consider in searching for evidence of chiral curvature. Kaon contributions take on the same form in the limit in which baryon mass splittings are neglected.

As for the charge radii, negative values of χ provide curvature towards more positive values as the chiral limit is approached, and vice versa for positive values of χ. However, the reason for this is more subtle than in the case of the charge radii and is due to the dependence of μ on $\chi {m_q}^{1/2}$. In this case μ is a parabolic function of m_q with two wings as seen in Fig. 5.3. Since m_q being the quark mass is always positive, the two wings of the parabola arise due to the positive and negative values of χ. The upper wing with χ positive has a negative curvature towards the chiral limit and the lower wing with negative χ has a positive curvature towards the chiral limit.

As emphasized earlier in our discussion of charge radii, the flavor-singlet η' meson remains degenerate with the pion in the quenched approximation and makes important contributions to quenched chiral nonanalytic behavior. The neutrality of its charge prevents it from contributing to the coefficients of Tables A.38 and A.39. However, the double hair-pin diagram in which the vector current couples to the virtual baryon intermediary does give rise to a logarithmic divergence in baryon magnetic moments. However the relatively small couplings of the η' render these contributions negligible at the quark masses probed here [47].

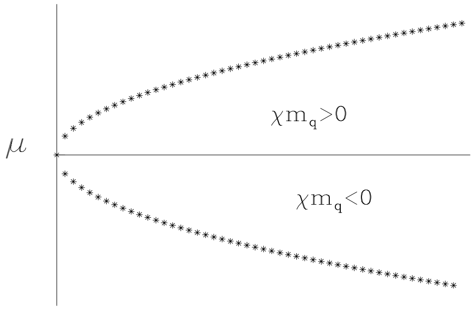

Figure 5.3: LNA behavior of μ.

The decuplet magnetic moments in χPT have been studied extensively, [48, 29, 49]. Cloet *et al* [49] gave expressions for the magnetic moments of the decuplet baryons in terms of phenomenological constants and established relations between magnetic moments of various decuplet baryons. The leading loop contributions seen in χPT and Partially Quenched Chiral Perturbation Theory (PχPT) are not seen in QχPT [50].

The meson cloud can never carry a direct contribution to the decuplet magnetic moments unlike the octet case and hence any chiral non-analytic behavior is not expected to a first order.

In the current study we compare the results of octet baryons with the QχPT.

Chapter 6

Form Factors on the Lattice

6.1 Introduction

The calculation of the electric and magnetic form factors is the first step in understanding the electromagnetic structure of hadrons. Charge radii, magnetic moments and magnetic radii can then all be extracted from the electric and magnetic form factors once known.

The octet baryons, being spin $1/2$ particles, have two form factors, $F_1(q^2)$ and $F_2(q^2)$, called the Pauli and Dirac form factors, defined at momentum transfer q^2. These are related to the Sachs form of electromagnetic form factors, viz., $\mathcal{G}_E(q^2)$, and $\mathcal{G}_M(q^2)$ via the relations

$$\begin{aligned} \mathcal{G}_E(q^2) &= F_1(q^2) - \frac{q^2}{(2M)^2} F_2(q^2)\,, \\ \mathcal{G}_M(q^2) &= F_1(q^2) + F_2(q^2)\,. \end{aligned} \tag{6.1}$$

The decuplet baryons being spin 3/2 particles have four form factors designated as $\mathcal{G}_{E0}(q^2)$, $\mathcal{G}_{E2}(q^2)$, $\mathcal{G}_{M1}(q^2)$ and $\mathcal{G}_{M3}(q^2)$.

The charge radius of a baryon depends on the electric form factor $\mathcal{G}_E(q^2)$ and is given by

$$\langle r_{\mathrm{E}}^2 \rangle = -6 \frac{d}{dq^2} \mathcal{G}_E(q^2) \bigg|_{q^2=0} . \tag{6.2}$$

The magnetic radius has a similar relation with the magnetic form factor and is given by

$$\langle r_{\mathrm{M}}^2 \rangle = -6 \frac{d}{dq^2} \mathcal{G}_M(q^2) \bigg|_{q^2=0} . \tag{6.3}$$

Magnetic moment is the magnetic form factor calculated at zero momentum transfer i.e.,

$$\vec{\mu} = \mathcal{G}_M(0)\,. \tag{6.4}$$

The extraction of baryon mass and electromagnetic form factors proceeds through the calculation of the ensemble average (denoted $\langle \,\cdots\, \rangle$) of two and three-point Green functions. The two-point function is defined as

$$\langle\, G^{BB}(t;\vec{p},\Gamma)\,\rangle = \sum_{\vec{x}} e^{-i\vec{p}\cdot\vec{x}}\Gamma^{\beta\alpha}\,\langle\, \Omega \,\big|\, T\left(\chi^{\alpha}(x)\overline{\chi}^{\beta}(0)\right) \big|\, \Omega \,\rangle\,. \tag{6.5}$$

Here Ω represents the QCD vacuum, Γ is a 4×4 matrix in Dirac space and α, β are Dirac indices.

Similarly the three-point correlation function for the electromagnetic current, $j^{\mu}(x)$, is defined as

$$\langle\, G^{Bj^{\mu}B}(t_2,t_1;\vec{p}\,',\vec{p};\Gamma)\,\rangle = \sum_{\vec{x}_2,\vec{x}_1} e^{-i\vec{p}\,'\cdot\vec{x}_2}e^{+i\left(\vec{p}\,'-\vec{p}\right)\cdot\vec{x}_1}\Gamma^{\beta\alpha}\,\langle\, \Omega \,\big|\, T\left(\chi^{\alpha}(x_2)\,j^{\mu}(x_1)\overline{\chi}^{\beta}(0)\right) \big|\, \Omega \,\rangle\;. \tag{6.6}$$

The electric and magnetic form factors can be expressed as ratios of the three point to two point correlation functions, which will be explained in the following sections.

6.2 Interpolating Fields

In this analysis we work with the standard established interpolating fields commonly used in lattice QCD simulations. The notation adopted is similar to that of [51].

6.2.1 Octet Interpolating Fields

To access the proton we use the positive parity interpolating field

$$\chi^{p+}(x) \;=\; \epsilon^{abc}\left(u^{aT}(x)\,C\gamma_5\,d^{b}(x)\right)u^{c}(x)\,, \tag{6.7}$$

where the fields u, d are evaluated at Euclidean space-time point x, C is the charge conjugation matrix, a, b and c are color labels, and the superscript T denotes the transpose. This interpolating field transforms as a spinor under a parity transformation. That is, if the quark fields $q^{a}(x)$ ($q = u, d, \cdots$) transform as

$$\mathcal{P}\,q^{a}(x)\,\mathcal{P}^{\dagger} = +\gamma_0\,q^{a}(\tilde{x})\,, \tag{6.8}$$

where $\tilde{x} = (x_0, -\vec{x})$, then

$$\mathcal{P}\,\chi^{p+}(x)\,\mathcal{P}^{\dagger} = +\gamma_0\,\chi^{p+}(\tilde{x})\,. \tag{6.9}$$

The neutron interpolating field is obtained via the exchange $u \leftrightarrow d$, and the strangeness -2, Ξ interpolating fields are obtained by replacing the doubly represented u or d quark fields in Eq. (6.7) by s. Similarly, the charged strangeness -1, Σ interpolating files are obtained by replacing the singly represented u or d quark fields in Eq. (6.7) by s. For the Σ^0 hyperon one uses [51]

$$\chi^{\Sigma^0}(x) = \frac{1}{\sqrt{2}}\epsilon^{abc} \quad \Big\{ \quad \Big(u^{aT}(x)\, C\gamma_5\, s^b(x)\Big)\, d^c(x) \\ + \quad \Big(d^{aT}(x)\, C\gamma_5\, s^b(x)\Big)\, u^c(x)\Big\}\,. \tag{6.10}$$

Note that χ^{Σ^0} transforms as a triplet under $SU(2)$ isospin. An $SU(2)$ isosinglet interpolating field for the Λ can be constructed by the replacement “$+$” $\longrightarrow$ “$-$” in Eq. (6.10). For the $SU(3)$ octet Λ interpolating field used exclusively in the following, one has

$$\chi^{\Lambda}(x) = \frac{1}{\sqrt{6}}\epsilon^{abc}\Big\{2\Big(u^{aT}(x)\, C\gamma_5\, d^b(x)\Big)\, s^c(x) \quad + \quad \Big(u^{aT}(x)\, C\gamma_5\, s^b(x)\Big)\, d^c(x) \\ - \quad \Big(d^{aT}(x)\, C\gamma_5\, s^b(x)\Big)\, u^c(x)\Big\}\,. \tag{6.11}$$

6.2.2 Decuplet Interpolating Fields

The commonly used interpolating field for exciting the Δ^{++} resonance from the QCD vacuum takes the long established [52, 53] form of

$$\chi_\mu^{\Delta^{++}}(x) = \epsilon^{abc}\Big(u^{Ta}(x) C\gamma_\mu u^b(x)\Big)\, u^c(x)\,. \tag{6.12}$$

The generalization of this interpolating field for the Δ^+ composed of two u quarks and one d quark has the form

$$\chi_\mu^{\Delta^{+}}(x) = \frac{1}{\sqrt{3}}\,\epsilon^{abc}\Big[\quad 2 \quad \Big(u^{Ta}(x) C\gamma_\mu d^b(x)\Big)\, u^c(x) \\ + \quad \Big(u^{Ta}(x) C\gamma_\mu u^b(x)\Big)\, d^c(x)\ \Big]\,. \tag{6.13}$$

Other decuplet baryon interpolating fields are obtained with the appropriate substitutions of $u(x),\ d(x)\ \to\ u(x),\ d(x)$ or $s(x)$. The interpolating field for Σ^{*0} is given by the symmetric generalization

$$\chi_\mu^{\Sigma^{*0}}(x) = \sqrt{\frac{2}{3}}\,\epsilon^{abc} \quad \Big[\quad \Big(u^{Ta}(x) C\gamma_\mu d^b(x)\Big)\, s^c(x) \\ + \quad \Big(d^{Ta}(x) C\gamma_\mu s^b(x)\Big)\, u^c(x) \\ + \quad \Big(s^{Ta}(x) C\gamma_\mu u^b(x)\Big)\, d^c(x)\ \Big]\,. \tag{6.14}$$

The $SU(2)$-isospin symmetry relationship for the Σ^* form factors is given by

$$\Sigma^{*0} = \frac{\Sigma^{*+} + \Sigma^{*-}}{2} \,, \tag{6.15}$$

which may be easily seen from the Σ^{*0} interpolating field by noting

$$\begin{aligned} &\epsilon^{abc} \left(s^{Ta}(x) C \gamma_\mu u^b(x) \right) d^c(x) = \\ &\qquad\qquad \epsilon^{abc} \left(u^{Ta}(x) C \gamma_\mu s^b(x) \right) d^c(x). \end{aligned} \tag{6.16}$$

6.3 Correlation functions at the hadronic level

As discussed earlier, extraction of baryon masses and electromagnetic form factors proceeds through the calculation of the ensemble average (denoted as $\langle \, \cdots \, \rangle$) of two and three-point correlation functions.

The two-point function is defined as

$$\langle \, G^{BB}(t; \vec{p}, \Gamma) \, \rangle = \sum_{\vec{x}} e^{-i\vec{p}\cdot\vec{x}} \, \Gamma^{\beta\alpha} \; \langle \, \Omega \, \big| \, T \left(\chi^\alpha(x) \overline{\chi}^\beta(0) \right) \big| \, \Omega \, \rangle \; . \tag{6.17}$$

Here Ω represents the QCD vacuum, Γ is a 4×4 matrix in Dirac space and α, β are Dirac indices.

6.3.1 Octet Correlation Functions

At the hadronic level we insert a complete set of states $\big| \, B, p, s \, \rangle$ and define

$$\langle \, \Omega \, \big| \, \chi(0) \, \big| \, B, p, s \, \rangle = Z_B(p) \sqrt{\frac{M}{E_p}} u(p, s) \,, \tag{6.18}$$

where $Z_B(p)$ represents the coupling strength of $\chi(0)$ to baryon B, and $E_p = \sqrt{\vec{p}^2 + M^2}$. A momentum dependence for $Z_B(p)$ is included for the case where a smeared sink is employed. The spin 1/2 Dirac matrices obey

$$\sum_p \sum_s u(p, s) \overline{u}(p, s) = \gamma \cdot p - M \,. \tag{6.19}$$

For large Euclidean time the ground state dominates and we find

$$\langle \, G^{BB}(t; \vec{p}, \Gamma) \, \rangle \simeq \frac{Z_B(p) \overline{Z}_B(p)}{2E_p} e^{-E_p t} \, tr \left[\Gamma(-i\gamma \cdot p + M) \right] \; . \tag{6.20}$$

Here $\overline{Z}_B(p)$ is the coupling strength of the source $\overline{\chi}(0)$ to the baryon. The momentum dependence allows for the use of smeared fermion sources in the creation of the quark propagators and the differentiation between source and sink allows for our use of smeared sources and point sinks in the following.

Similarly the three-point correlation function for the electromagnetic current, $j^\mu(x)$, is defined as

$$\langle\, G^{Bj^\mu B}(t_2, t_1; \vec{p}\,', \vec{p}; \Gamma)\,\rangle = \sum_{\vec{x}_2, \vec{x}_1} e^{-i\vec{p}\,'\cdot\vec{x}_2} e^{+i\left(\vec{p}\,'-\vec{p}\right)\cdot\vec{x}_1} \Gamma^{\beta\alpha} \,\langle\, \Omega \,\big|\, T\left(\chi^\alpha(x_2) j^\mu(x_1) \overline{\chi}^\beta(0)\right) \big|\, \Omega \,\rangle\ . \tag{6.21}$$

For large Euclidean time separations $t_2 - t_1 \gg 1$ and $t_1 \gg 1$, the three-point function at the hadronic level is dominated by the contribution from the ground state

$$\begin{aligned}\langle\, G^{Bj^\mu B}(t_2, t_1; \vec{p}\,', \vec{p}; \Gamma)\,\rangle = \ & \textstyle\sum_{s,s'} \ e^{-E_{p'}(t_2-t_1)} e^{-E_p t_1} \Gamma^{\beta\alpha} \,\langle\, \Omega \,\big|\, \chi^\alpha \,\big|\, p', s' \,\rangle \\ & \langle\, p', s' \,\big|\, j^\mu \,\big|\, p, s \,\rangle\langle\, p, s \,\big|\, \overline{\chi}^\beta \,\big|\, \Omega \,\rangle\ .\end{aligned} \tag{6.22}$$

The matrix element of the electromagnetic current has the general form

$$\langle\, p', s' \,\big|\, j^\mu \,\big|\, p, s \,\rangle = \left(\frac{M^2}{E_p E_{p'}}\right)^{1/2} \overline{u}(p', s') \left(F_1(q^2)\gamma^\mu - F_2(q^2)\sigma^{\mu\nu}\frac{q^\nu}{2M}\right) u(p, s)\,, \tag{6.23}$$

where $q = p' - p$. To eliminate the time dependence of the three-point functions we construct the following ratio,

$$R(t_2, t_1; \vec{p}\,', \vec{p}; \Gamma, \Gamma'; \mu) = \left[\frac{\langle\, G^{Bj^\mu B}(t_2, t_1; \vec{p}\,', \vec{p}; \Gamma)\,\rangle\langle\, G^{Bj^\mu B}(t_2, t_1; -\vec{p}, -\vec{p}\,'; \Gamma)\,\rangle}{\langle\, G^{BB}(t_2; \vec{p}\,'; \Gamma')\,\rangle\langle\, G^{BB}(t_2; -\vec{p}; \Gamma')\,\rangle}\right]^{1/2} . \tag{6.24}$$

We further define a reduced ratio $\overline{R}(\vec{p}\,', \vec{p}; \Gamma, \Gamma'; \mu)$ as

$$\overline{R}(\vec{p}\,', \vec{p}; \Gamma, \Gamma'; \mu) = \left[\frac{2E_p}{E_p + M}\right]^{1/2} \left[\frac{2E_{p'}}{E_{p'} + M}\right]^{1/2} R(t_2, t_1; \vec{p}\,', \vec{p}; \Gamma, \Gamma'; \mu)\,, \tag{6.25}$$

from which the Sachs forms for the electromagnetic form factors

$$\mathcal{G}_E(q^2) = F_1(q^2) - \frac{q^2}{(2M)^2} F_2(q^2)\,, \tag{6.26}$$

$$\mathcal{G}_M(q^2) = F_1(q^2) + F_2(q^2)\,, \tag{6.27}$$

may be extracted though an appropriate choice of Γ and Γ'. A straight forward calculation reveals

$$\mathcal{G}_E(q^2) = \overline{R}(\vec{q}, \vec{0}; \Gamma_4, \Gamma_4, 4)\,, \tag{6.28}$$

$$|\epsilon_{ijk} q^i|\, \mathcal{G}_M(q^2) = (E_q + M)\, \overline{R}(\vec{q}, \vec{0}; \Gamma_j, \Gamma_4, k)\,, \tag{6.29}$$

$$|q^k|\, \mathcal{G}_E(q^2) = (E_q + M)\, \overline{R}(\vec{q}, \vec{0}; \Gamma_4, \Gamma_4, k)\,, \tag{6.30}$$

where

$$\begin{aligned} \Gamma_j &= \frac{1}{2}\begin{pmatrix} \sigma_j & 0 \\ 0 & 0 \end{pmatrix} \\ \Gamma_4 &= \frac{1}{2}\begin{pmatrix} I & 0 \\ 0 & 0 \end{pmatrix}. \end{aligned} \tag{6.31}$$

For large time separations $t_2 - t_1 \gg 1$ and $t_1 \gg 1$ these ratios are constant in time and are proportional to the electromagnetic form factors.

6.3.2 Decuplet Correlation Functions

For the spin-3/2 decuplet case one proceeds by inserting a complete set of states $\big|\, B, p, s \,\rangle$ and defining

$$\langle\, \Omega \,\big|\, \chi_\sigma(0) \,\big|\, B, p, s \,\rangle = Z_B(p)\sqrt{\frac{M}{E_p}}\, u_\sigma(p, s)\,, \tag{6.32}$$

where Z_B represents the coupling strength of $\chi(0)$ to baryon B. Momentum is denoted by p, spin by s, and $u_\alpha(p, s)$ is a spin-vector in the Rarita-Schwinger formalism. $E_p = \sqrt{\vec{p}^2 + M^2}$ and Dirac indices have been suppressed. Using the Rarita-Schwinger spin sum,

$$\begin{aligned} \sum_s u_\sigma(p, s)\overline{u}_\tau(p, s) &= -\frac{\gamma \cdot p + M}{2M}\left\{ g_{\sigma\tau} - \frac{1}{3}\gamma_\sigma\gamma_\tau - \frac{2p_\sigma p_\tau}{3M^2} + \frac{p_\sigma\gamma_\tau - p_\tau\gamma_\sigma}{3M} \right\} \\ &\equiv \Lambda_{\sigma\tau}, \end{aligned} \tag{6.33}$$

and $\vec{p} = (p, 0, 0)$, the large Euclidean time limit of the two point function takes the form

$$\langle\, G^{BB}_{\sigma\tau}(t; \vec{p}, \Gamma_4) \,\rangle = Z_B(p)\overline{Z_B(p)}\frac{M}{E_p}e^{-E_p t}\, tr\,[\, \Gamma_4\, \Lambda_{\sigma\tau}\,]\,, \tag{6.34}$$

where

$$\langle\, G^{BB}_{00}(t; \vec{p}, \Gamma_4) \,\rangle = Z_B(p)\overline{Z_B(p)}\,\frac{2}{3}\,\frac{|\vec{p}|^2}{M_B^2}\left(\frac{E_p + M_B}{2E_p}\right)e^{-E_p t}, \tag{6.35}$$

$$\langle\, G^{BB}_{11}(t; \vec{p}, \Gamma_4) \,\rangle = Z_B(p)\overline{Z_B(p)}\,\frac{2}{3}\,\frac{E_p^2}{M_B^2}\left(\frac{E_p + M_B}{2E_p}\right)e^{-E_p t}, \tag{6.36}$$

$$\langle\, G^{BB}_{22}(t; \vec{p}, \Gamma_4) \,\rangle = Z_B(p)\overline{Z_B(p)}\,\frac{2}{3}\left(\frac{E_p + M_B}{2E_p}\right)e^{-E_p t}, \tag{6.37}$$

$$\langle\, G^{BB}_{33}(t; \vec{p}, \Gamma_4) \,\rangle = Z_B(p)\overline{Z_B(p)}\,\frac{2}{3}\left(\frac{E_p + M_B}{2E_p}\right)e^{-E_p t}. \tag{6.38}$$

In determining the appropriate forms suitable for calculations using Sakurai's conventions the definitions of the γ-matrices used in the interpolating fields are taken into account. Since the non vanishing terms of $G^{BB}_{\sigma\tau}$ are diagonal in σ and τ, the γ-matrices are paired with their Hermitian conjugates. Since the γ-matrix notations differ only by factors of i and -1, there are no required alterations for calculations using the notation of Sakurai.

Equations (6.35) through (6.38) provide four correlation functions from which a baryon mass may be extracted. All baryon masses extracted from the different selections of Lorentz indices agree within statistical uncertainties. The combination providing the smallest statistical fluctuations is $\langle\ G^{BB}_{22}(t;\vec{p},\Gamma_4) + G^{BB}_{33}(t;\vec{p},\Gamma_4)\ \rangle$ and these results are presented in Chapter (8).

It should be noted that the spin-3/2 interpolating field also has overlap with spin-1/2 baryons. For the Δ baryons and Ω^- this poses no problem as these baryons are the lowest lying baryons in the mass spectrum having the appropriate isospin and strangeness quantum numbers. However, Σ^* and Ξ^* correlation functions may have lower lying spin-1/2 components and therefore it is desirable to use the spin-3/2 projection operator [54]

$$P^{3/2}_{\mu\nu}(p) = g_{\mu\nu} - \frac{1}{3}\gamma_\mu\gamma_\nu - \frac{1}{3p^2}\left(\gamma\cdot p\,\gamma_\mu\, p_\nu + p_\mu\,\gamma_\nu\,\gamma\cdot p\right)\,. \tag{6.39}$$

However, to use this operator, one must calculate the full 4^4 matrix in Dirac and Lorentz spaces of $G^{BB}_{\sigma\tau}(t;\vec{p},\Gamma)$ which exceeds the computation time of our current analysis of 4 Lorentz terms and 2 Dirac terms by a factor of 32.

QCD sum rule investigations of Σ^* and Ξ^* hyperons suggest that the spin-1/2 component of the spin-3/2 interpolating field is small relative to the spin-3/2 component [55]. However, the analysis does not determine whether the spin-1/2 component lies above or below the lowest lying spin-3/2 state. Our lattice results for baryon two-point functions give no indication of a low-lying spin-1/2 component being excited by the spin-3/2 interpolating fields.

6.4 Correlation functions at the quark level

Here the two and three-point functions of Sec. 6.3 are calculated at the quark level by using the explicit forms of the interpolating fields of Sec. 6.2 and contracting out all possible pairs of quark field operators. These become quark propagators in the ensemble average. For convenience, we introduce the shorthand notation for the correlation functions $\mathcal{G}$ of quark propagators S

$$\begin{aligned}\mathcal{G}(S_{f_1}, S_{f_2}, S_{f_3}) \equiv \epsilon^{abc}\epsilon^{a'b'c'} \quad \Big\{ \quad & S_{f_1}^{aa'}(x,0)\,\mathrm{tr}\left[S_{f_2}^{bb'\,T}(x,0) S_{f_3}^{cc'}(x,0)\right] \\ & + S_{f_1}^{aa'}(x,0)\, S_{f_2}^{bb'\,T}(x,0)\, S_{f_3}^{cc'}(x,0)\Big\}\,, \end{aligned} \tag{6.40}$$

where $S_{f_{1-3}}^{aa'}(x,0)$ are the quark propagators in the background link-field configuration U corresponding to flavors f_{1-3}.This allows us to express the correlation functions in a compact form.

The quark level correlation function for χ^{p+} can be written as

$$G^{p+}(t,\vec{p};\Gamma) = \left\langle \sum_{\vec{x}} e^{-i\vec{p}\cdot\vec{x}} \mathrm{tr}\left[\Gamma\ \mathcal{G}\left(S_u,\ \widetilde{C}S_d\widetilde{C}^{-1},\ S_u\right)\right]\right\rangle\,, \tag{6.41}$$

where $\langle \cdots \rangle$ is the ensemble average over the link fields, Γ is the $\Gamma_\pm$ projection operator that separates the positive and negative parity states, and $\widetilde{C} = C\gamma_5$. For ease of notation, we will drop the angled brackets, $\langle \cdots \rangle$, and in the following all correlation functions will be understood to be ensemble averages.

Two-point correlation functions for other octet baryons composed of a doubly-represented quark flavor and a singly-represented quark flavor follow from Eq. (6.42) with the appropriate substitution of flavor subscripts. The correlation function for the neutral member Σ^0 is given by the average of correlation functions for the charged states Σ^+ and Σ^-. Finally the correlation function for Λ obtained from the octet-interpolating field of Eq. (6.11) is

$$\begin{aligned} G^{\Lambda^8}(t,\vec{p};\Gamma) = \frac{1}{6}\sum_{\vec{x}} e^{-i\vec{p}\cdot\vec{x}} \mathrm{tr}\Big[\Gamma\ \Big\{ \ & 2\,\mathcal{G}\left(S_s,\ \widetilde{C}S_u\widetilde{C}^{-1},\ S_d\right) + 2\,\mathcal{G}\left(S_s,\ \widetilde{C}S_d\widetilde{C}^{-1},\ S_u\right) \\ + \ & 2\,\mathcal{G}\left(S_d,\ \widetilde{C}S_u\widetilde{C}^{-1},\ S_s\right) + 2\,\mathcal{G}\left(S_u,\ \widetilde{C}S_d\widetilde{C}^{-1},\ S_s\right) \\ - \ & \mathcal{G}\left(S_d,\ \widetilde{C}S_s\widetilde{C}^{-1},\ S_u\right) - \mathcal{G}\left(S_u,\ \widetilde{C}S_s\widetilde{C}^{-1},\ S_d\right)\Big\}\Big]\,. \end{aligned} \tag{6.42}$$

Considering the Δ^+ correlation function at the quark level and contracting out pairs

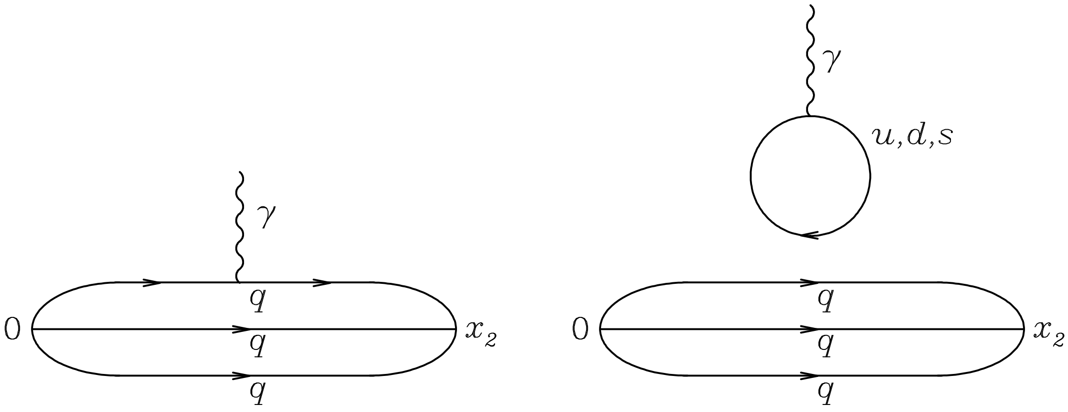

Figure 6.1: Diagrams illustrating the two topologically different insertions of the current within the framework of lattice QCD.

of quark field operators gives the two-point function as

$$
\begin{aligned}
\left\langle T\left(\chi_\mu^{\Delta^+}(x), \overline{\chi}_\nu^{\Delta^+}(0)\right)\right\rangle = & \ \frac{1}{3}\,\epsilon^{abc}\epsilon^{a'b'c'}\Big\{ \\
& 4S_u^{aa'}\,\gamma_\nu\, C S_u^{Tbb'} C\,\gamma_\mu\, S_d^{cc'} \\
& + 4S_u^{aa'}\,\gamma_\nu\, C S_d^{Tbb'} C\,\gamma_\mu\, S_u^{cc'} \\
& + 4S_d^{aa'}\,\gamma_\nu\, C S_u^{Tbb'} C\,\gamma_\mu\, S_u^{cc'} \\
& + 2S_u^{aa'}\, tr\left[\gamma_\nu\, C S_u^{Tbb'} C\,\gamma_\mu\, S_d^{cc'}\right] \\
& + 2S_u^{aa'}\, tr\left[\gamma_\nu\, C S_d^{Tbb'} C\,\gamma_\mu\, S_u^{cc'}\right] \\
& + 2S_d^{aa'}\, tr\left[\gamma_\nu\, C S_u^{Tbb'} C\,\gamma_\mu\, S_u^{cc'}\right]\Big\}
\end{aligned}
\tag{6.43}
$$

where the quark-propagator $S_u^{aa'} = T\left(u^a(x), \overline{u}^{a'}(0)\right)$ and similarly for other quark flavors. $SU(3)$-flavor symmetry is clearly displayed in this equation.

6.4.1 Three-point Functions at the quark level - Octet

In determining the three point function, one encounters two topologically different ways of performing the current insertion. Figure 6.1 displays skeleton diagrams for these two insertions. These diagrams may be dressed with an arbitrary number of gluons (and additional sea-quark loops in full QCD). Diagram (a) illustrates the connected insertion of the current to one of the quarks created via the baryon interpolating field. This simple skeleton diagram does indeed contain a sea-quark component, as upon dressing the diagram with gluon exchange, quark-loop and Z-diagrams flows become possible. It is here that “Pauli-blocking” in the sea contributions, central to obtaining violation of the Gottfried sum rule, are taken into account. Diagram (b) accounts for an alternative quark-field contraction where the current first produces a disconnected $q\,\overline{q}$ loop-pair which in turn interacts with the valence quarks of the baryon via gluons. Thus, the number of terms in the three-point function is four times that in Eq. (6.41).

The correlation function for proton matrix elements obtained from Eq. (6.7) is

$$\begin{aligned}
T\left(\chi^{p+}(x_2)\, j^{\mu}(x_1)\overline{\chi}^{\,p+}(0)\right) = & \\
& \mathcal{G}\left(\widehat{S}_u(x_2,x_1,0),\, \widetilde{C}S_d(x_2,0)\widetilde{C}^{-1},\, S_u(x_2,0)\right) \\
+ \quad & \mathcal{G}\left(S_u(x_2,0),\, \widetilde{C}S_d(x_2,0)\widetilde{C}^{-1},\, \widehat{S}_u(x_2,x_1,0)\right) \\
+ \quad & \mathcal{G}\left(S_u(x_2,0),\, \widetilde{C}\widehat{S}_d(x_2,x_1,0)\widetilde{C}^{-1},\, S_u(x_2,0)\right) \\
+ \sum_{q=u,d,s} e_q \quad \textstyle\sum_i \quad & tr\left[S_q^{ii}(x_1,x_1)\,\gamma_\mu\right] \mathcal{G}\left(\widehat{S}_u(x_2,0),\, \widetilde{C}S_d(x_2,0)\widetilde{C}^{-1},\, S_u(x_2,0)\right)\,, \qquad (6.44)
\end{aligned}$$

where

$$\widehat{S}_q^{aa'}(x_2,x_1,0) = e_q \sum_i S_q^{ai}(x_2,x_1)\,\gamma_\mu\, S_q^{ia'}(x_1,0)\,, \qquad (6.45)$$

denotes the connected insertion of the electromagnetic current to a quark of charge e_q.

The first two terms of Eq. (6.44) provide the connected insertion contribution of the u-quark sector to the proton’s electromagnetic properties, whereas the third term provides the connected d-quark contribution. The latter term of Eq. (6.44) accounts for the “disconnected” loop contribution depicted in Fig. 6.1b. Here, the sum over the quarks running around the loop has been restricted to the flavors relevant to the ground state baryon octet. In the $SU(3)$-flavor limit the sum vanishes for the electromagnetic current. However, the heavier strange quark mass allows for a nontrivial result.

The “disconnected” current insertion requires a numerical estimate of $S_q^{ii}(x_1,x_1)$ for the lattice volume of diagonal spatial indices at $q_1^2 \neq 0$. As this requires numerous source vectors in the fermion-matrix inversion, determination of this propagator is numerically intensive [56, 57, 58]. Indeed, an indirect method using experimental results, chiral effective field theory and the lattice results from the connected current insertion presented herein, provides the most precise determinations of these quark loop contributions to the nucleon’s electromagnetic structure [59, 60, 61] at present. However, this approach should be viewed as complementary to an *ab initio* determination via lattice QCD which awaits a next-generation dynamical-fermion simulation of QCD [45].

It is interesting to examine the structure of the connected insertion contributions to the proton's structure. Here, we see very different roles played by u and d quarks in the correlation function, in that only the d-quark appears in the second position of $\mathcal{G}$. The absence of equivalence for u and d contributions allows the connected quark sector to give rise to a nontrivial neutron charge radius, a large neutron magnetic moment, or a violation of the Gottfried sum rule. As each term of Eq. (6.44) can be calculated individually, it is a simple task to isolate the quark sector contributions to the baryon electromagnetic properties.

Another interesting point to emphasize, is that there is no simple relationship between the properties of a particular quark flavor bound in different baryons. For example, the correlator for Σ^+ is given by Eq. (6.44) with $d \to s$. Hence, a u-quark propagator in Σ^+ is multiplied by an s-quark propagator, whereas in the proton the u-quark propagators are multiplied by a d-quark propagator. The different mass of the neighboring quark gives rise to an environment sensitivity in the u-quark contributions to observables[51, 62, 63, 64, 65, 66, 59]. This point is sharply in contrast with the naive concept of an intrinsic quark property which is independent of the quark's environment. This concept of an intrinsic quark property is a fundamental foundation of many constituent based quark models and is not in accord with real QCD calculations.

The correlation function relevant to the Δ^+ current matrix element is

$$
\begin{aligned}
&T\left(\chi_\mu^{\Delta^+}(x_2)\, j^\mu(x_1)\overline{\chi}_\nu^{\Delta^+}(0)\right) = \frac{1}{3}\,\epsilon^{abc}\epsilon^{a'b'c'}\Big\{ \\
&\quad 4\widehat{S}_u^{aa'}\,\gamma_\nu\, CS_u^{Tbb'} C\,\gamma_\mu\, S_d^{cc'} + 4\widehat{S}_u^{aa'}\,\gamma_\nu\, CS_d^{Tbb'} C\,\gamma_\mu\, S_u^{cc'} + 4\widehat{S}_d^{aa'}\,\gamma_\nu\, CS_u^{Tbb'} C\,\gamma_\mu\, S_u^{cc'} \\
&\quad +4S_u^{aa'}\,\gamma_\nu\, C\widehat{S}_u^{Tbb'} C\,\gamma_\mu\, S_d^{cc'} + 4S_d^{aa'}\,\gamma_\nu\, C\widehat{S}_u^{Tbb'} C\,\gamma_\mu\, S_u^{cc'} + 4S_u^{aa'}\,\gamma_\nu\, C\widehat{S}_d^{Tbb'} C\,\gamma_\mu\, S_u^{cc'} \\
&\quad +4S_u^{aa'}\,\gamma_\nu\, CS_d^{Tbb'} C\,\gamma_\mu\, \widehat{S}_u^{cc'} + 4S_d^{aa'}\,\gamma_\nu\, CS_u^{Tbb'} C\,\gamma_\mu\, \widehat{S}_u^{cc'} + 4S_u^{aa'}\,\gamma_\nu\, CS_u^{Tbb'} C\,\gamma_\mu\, \widehat{S}_d^{cc'} \\
&\quad +2\widehat{S}_u^{aa'}\, tr\left[\gamma_\nu\, CS_u^{Tbb'} C\,\gamma_\mu\, S_d^{cc'}\right] + 2\widehat{S}_u^{aa'}\, tr\left[\gamma_\nu\, CS_d^{Tbb'} C\,\gamma_\mu\, S_u^{cc'}\right] + 2\widehat{S}_d^{aa'}\, tr\left[\gamma_\nu\, CS_u^{Tbb'} C\,\gamma_\mu\, S_u^{cc'}\right] \\
&\quad +2S_u^{aa'}\, tr\left[\gamma_\nu\, C\widehat{S}_u^{Tbb'} C\,\gamma_\mu\, S_d^{cc'}\right] + 2S_d^{aa'}\, tr\left[\gamma_\nu\, C\widehat{S}_u^{Tbb'} C\,\gamma_\mu\, S_u^{cc'}\right] + 2S_u^{aa'}\, tr\left[\gamma_\nu\, C\widehat{S}_d^{Tbb'} C\,\gamma_\mu\, S_u^{cc'}\right] \\
&\quad +2S_u^{aa'}\, tr\left[\gamma_\nu\, CS_d^{Tbb'} C\,\gamma_\mu\, \widehat{S}_u^{cc'}\right] + 2S_d^{aa'}\, tr\left[\gamma_\nu\, CS_u^{Tbb'} C\,\gamma_\mu\, \widehat{S}_u^{cc'}\right] + 2S_u^{aa'}\, tr\left[\gamma_\nu\, CS_u^{Tbb'} C\,\gamma_\mu\, \widehat{S}_d^{cc'}\right]\Big\} \\
&\quad + \sum_{q=u,d,s} e_q \sum_i tr\left[S_q^{ii}(x_1, x_1)\,\gamma_\mu\right] \frac{1}{3}\,\epsilon^{abc}\epsilon^{a'b'c'}\Big\{ \\
&\quad 4S_u^{aa'}\,\gamma_\nu\, CS_u^{Tbb'} C\,\gamma_\mu\, S_d^{cc'} + 4S_u^{aa'}\,\gamma_\nu\, CS_d^{Tbb'} C\,\gamma_\mu\, S_u^{cc'} + 4S_d^{aa'}\,\gamma_\nu\, CS_u^{Tbb'} C\,\gamma_\mu\, S_u^{cc'} \\
&\quad +2S_u^{aa'}\, tr\left[\gamma_\nu\, CS_u^{Tbb'} C\,\gamma_\mu\, S_d^{cc'}\right] + 2S_u^{aa'}\, tr\left[\gamma_\nu\, CS_d^{Tbb'} C\,\gamma_\mu\, S_u^{cc'}\right] + 2S_d^{aa'}\, tr\left[\gamma_\nu\, CS_u^{Tbb'} C\,\gamma_\mu\, S_u^{cc'}\right]\Big\}
\end{aligned}
\tag{6.46}
$$

where

$$\widehat{S}_q^{aa'}(x_2, x_1, 0) = e_q \sum_i S_q^{ai}(x_2, x_1)\, \gamma_\mu\, S_q^{ia'}(x_1, 0)\,, \tag{6.47}$$

denotes the connected insertion of the probing current to a quark of charge e_q. Here we have explicitly selected the electromagnetic current. However, the following discussion may be generalized to any quark-field-based conserved current operator bilinear in the quark fields.

The latter term of Eq. (6.46) accounts for the loop contribution depicted in Fig. 6.1b. The sum over the quarks running around the loop has been restricted to the flavors relevant to the ground state baryon octet and decuplet. In the $SU(3)$-flavor limit the sum vanishes for the electromagnetic current. However, the heavier strange quark mass allows for a nontrivial result. Due to the technical difficulties of numerically estimating M^{-1} for the squared lattice volume of diagonal spatial indices at $q^2 \neq 0$, these contributions have been omitted from previous lattice calculations of electromagnetic structure. For other observables such as the scalar density or forward matrix elements of the axial vector current relevant to the spin of the baryon, the “charges” running around the loop do not sum to zero. In this case the second term of Eq. (6.46) can be just as significant as the connected term [67, 68].

An examination of Eq. (6.46) reveals complete symmetry among the quark flavors in the correlation function. For example, wherever a d quark appears in the correlator, a u quark also appears in the same position in another term. An interesting consequence of this is that the connected insertion of the electromagnetic current for Δ^0 vanishes. All electromagnetic properties of the Δ^0 have their origin strictly in the disconnected loop contribution. Physically, what this means is that the valence wave function for each of the quarks in the Δ resonances are identical.

6.4.2 Three-point functions and multipole form factors - Decuplet

Here we begin with a brief overview of the results of Ref. [69], where the multipole form factors are defined in terms of the covariant vertex functions and in terms of the current matrix elements. The Dirac representation of the γ-matrices as defined in Itzykson and Zuber [70] continues to be used to facilitate calculations of the γ-matrix algebra. Finally, the results are reported in Sakurai’s notation in a form suitable for calculation in lattice field theory.

The electromagnetic current matrix element for spin-3/2 particles may be written as

$$\langle\, p', s' \,\big|\, j^\mu(0) \,\big|\, p, s \,\rangle = \sqrt{\frac{M_B^2}{E_p E_{p'}}}\, \overline{u}_\alpha(p', s') O^{\alpha\mu\beta} u_\beta(p, s). \tag{6.48}$$

Here $p,\ p'$ denote momenta, $s\ s'$ spins, and $u_\alpha(p,s)$ is a Rarita-Schwinger spin-vector. The following Lorentz covariant form for the tensor

$$O^{\alpha\mu\beta} = -g^{\alpha\beta}\left\{a_1\gamma^\mu + \frac{a_2}{2M_B}P^\mu\right\} - \frac{q^\alpha q^\beta}{(2M_B)^2}\left\{c_1\gamma^\mu + \frac{c_2}{2M_B}P^\mu\right\}, \qquad (6.49)$$

where $P = p' + p$, $q = p' - p$ and M_B is the mass of the baryon, satisfies the standard requirements of invariance under time reversal, parity, G-parity and gauge transformations. The parameters a_1, a_2, c_1 and c_2 are independent covariant vertex function coefficients which are related to the multipole form factors.

The multipole expansion of the electromagnetic current matrix element, defined in terms of angular momentum recoupling algebra, has the following form

$$\begin{aligned}&\langle\, p', s' \,|\, j^0(0) \,|\, p, s \,\rangle = \\ &\qquad A\,\langle\, \tfrac{3}{2}\, s' \,\Big|\, G_{E0}(q^2) + 2\sqrt{5}\tau G_{E2}(q^2)\left[\Sigma^{(2)} \times [\widehat{q}\times\widehat{q}]^{(2)}\right]^{(0)} \Big|\, \tfrac{3}{2}\, s \,\rangle, \qquad (6.50)\end{aligned}$$

$$\begin{aligned}&\langle\, p', s' \,|\, \vec{j}(0) \,|\, p, s \,\rangle = \\ &\qquad \sqrt{\tau}\,\langle\, \tfrac{3}{2}\, s' \,\Big|\, \left\{G_{E0}(q^2) + 2\sqrt{5}\tau G_{E2}(q^2)\left[\Sigma^{(2)} \times [\widehat{q}\times\widehat{q}]^{(2)}\right]^{(0)}\right\}\widehat{P} \\ &\qquad + i\left\{\frac{1}{3}G_{M1}(q^2)\Sigma^{(1)} + 3\tau G_{M3}(q^2)\left[\Sigma^{(3)} \times [\widehat{q}\times\widehat{q}]^{(2)}\right]^{(1)}\right\}\times\widehat{q}\,\Big|\, \tfrac{3}{2}\, s \,\rangle, \qquad (6.51)\end{aligned}$$

where $\tau = -q^2/(2M_B)^2$ (≥ 0), and $\widehat{P}$ and $\widehat{q}$ are unit vectors. $A = \sqrt{1+\tau}$ in the laboratory frame ($\vec{p} = 0$) and $A = 1$ in the baryon Breit frame ($\vec{P} = \vec{p}\,' + \vec{p} = 0$). The spin matrix elements are defined by Clebsch-Gordan coefficients,

$$\langle\, \tfrac{3}{2}\, s' \,|\, \tfrac{3}{2}\, s \,\rangle = \delta_{s's}\,, \qquad (6.52)$$

$$\langle\, \tfrac{3}{2}\, s' \,|\, \Sigma^{(1)}_m \,|\, \tfrac{3}{2}\, s \,\rangle = \sqrt{15}\left(\tfrac{3}{2}s'1m \,\Big|\, \tfrac{3}{2}1\tfrac{3}{2}s\right), \qquad (6.53)$$

$$\langle\, \tfrac{3}{2}\, s' \,|\, \Sigma^{(2)}_m \,|\, \tfrac{3}{2}\, s \,\rangle = -\sqrt{\frac{5}{6}}\left(\tfrac{3}{2}s'2m \,\Big|\, \tfrac{3}{2}2\tfrac{3}{2}s\right), \qquad (6.54)$$

$$\langle\, \tfrac{3}{2}\, s' \,|\, \Sigma^{(3)}_m \,|\, \tfrac{3}{2}\, s \,\rangle = -\frac{7}{6}\sqrt{\frac{2}{3}}\left(\tfrac{3}{2}s'3m \,\Big|\, \tfrac{3}{2}3\tfrac{3}{2}s\right), \qquad (6.55)$$

where the Condon and Shortley phase convention has been used [71].

The multipole form factors are defined in terms of the covariant vertex function coefficients a_1, a_2, c_1 and c_2 through the following Lorentz invariant expressions [69],

$$\begin{aligned}
\mathcal{G}_{E0}(q^2) &= (1+\frac{2}{3}\tau)\,\{a_1+(1+\tau)a_2\} - \frac{1}{3}\tau(1+\tau)\,\{c_1+(1+\tau)c_2\}\ , && (6.56)\\
\mathcal{G}_{E2}(q^2) &= \{a_1+(1+\tau)a_2\} - \frac{1}{2}(1+\tau)\,\{c_1+(1+\tau)c_2\}\ , && (6.57)\\
\mathcal{G}_{M1}(q^2) &= (1+\frac{4}{5}\tau)a_1 - \frac{2}{5}\tau(1+\tau)c_1\,, && (6.58)\\
\mathcal{G}_{M3}(q^2) &= a_1 - \frac{1}{2}(1+\tau)c_1\,. && (6.59)
\end{aligned}$$

The multipole form factors $\mathcal{G}_{E0}$, $\mathcal{G}_{E2}$, $\mathcal{G}_{M1}$ and $\mathcal{G}_{M3}$ are referred to as charge ($E0$), electric-quadrupole ($E2$), magnetic-dipole ($M1$) and magnetic-octupole ($M3$) multipole form factors, respectively.

In a manner similar to that for the two-point function, the three-point Green function for the electromagnetic current is defined as

$$\begin{aligned}
&\langle\, G^{Bj^\mu B}_{\sigma\tau}(t_2,t_1;\vec{p}\,',\vec{p};\Gamma)\,\rangle = \\
&\qquad \sum_{\vec{x}_2,\vec{x}_1} e^{-i\vec{p}\,'\cdot\vec{x}_2}e^{+i\left(\vec{p}\,'-\vec{p}\right)\cdot\vec{x}_1}\Gamma^{\beta\alpha}\,\langle\,\Omega\,\big|\,T\left(\chi^\alpha_\sigma(x_2)\,j^\mu(x_1)\overline{\chi}^\beta_\tau(0)\right)\big|\,\Omega\,\rangle\ . \qquad (6.60)
\end{aligned}$$

Once again, the subscripts σ, τ are the Lorentz indices of the spin-3/2 interpolating fields. For large Euclidean time separations $t_2 - t_1 \gg 1$ and $t_1 \gg 1$ the three-point function at the hadronic level takes the limit

$$\begin{aligned}
&\langle\, G^{Bj^\mu B}_{\sigma\tau}(t_2,t_1;\vec{p}\,',\vec{p};\Gamma)\,\rangle = \sum_{s,s'} e^{-E_{p'}(t_2-t_1)}e^{-E_p t_1} \\
&\qquad \Gamma^{\beta\alpha}\,\langle\,\Omega\,\big|\,\chi^\alpha_\sigma\,\big|\,p',s'\,\rangle\langle\,p',s'\,\big|\,j^\mu\,\big|\,p,s\,\rangle\langle\,p,s\,\big|\,\overline{\chi}^\beta_\tau\,\big|\,\Omega\,\rangle\,, \qquad (6.61)
\end{aligned}$$

where the matrix element of the electromagnetic current is defined in Eq. (6.48), and the matrix elements of the interpolating fields are defined by Eq. (6.32).

In Ref. [69] it was noted that the time dependence of the three-point function may be eliminated by use of the two-point functions. However the appropriate combination of the two-point function Lorentz indices was not specified. Maintaining the lattice Ward identity, which guarantees the lattice electric form factor reproduces the total charge of the baryon at $q^2 = 0$, provides an indispensable guide to the optimum ratio of Green functions. The preferred ratio of two- and three-point Green functions is

$$
\begin{aligned}
&R_\sigma{}^\mu{}_\tau(t_2, t_1; \vec{p}\,', \vec{p}; \Gamma) = \\
&\qquad \left(\frac{\langle\, G^{Bj^\mu B}_{\sigma\tau}(t_2, t_1; \vec{p}\,', \vec{p}; \Gamma)\,\rangle \langle\, G^{Bj^\mu B}_{\sigma\tau}(t_2, t_1; -\vec{p}, -\vec{p}\,'; \Gamma)\,\rangle}{\langle\, G^{BB}_{\sigma\tau}(t_2; \vec{p}\,'; \Gamma_4)\,\rangle \langle\, G^{BB}_{\sigma\tau}(t_2; -\vec{p}; \Gamma_4)\,\rangle} \right)^{1/2} , && (6.62) \\
&\qquad \simeq \left(\frac{E_p + M}{2E_p} \right)^{1/2} \left(\frac{E_{p'} + M}{2E_{p'}} \right)^{1/2} \overline{R}_\sigma{}^\mu{}_\tau(\vec{p}\,', \vec{p}; \Gamma) , && (6.63)
\end{aligned}
$$

where we have defined the reduced ratio $\overline{R}_\sigma{}^\mu{}_\tau(\vec{p}\,', \vec{p}; \Gamma)$. Note that there is no implied sum over σ and τ in Eq. (6.62). In the continuum limit the approximate equality in Eq. 6.63 becomes an exact equality.

Using our standard definitions for Γ given in Eq. (6.31) and the Rarita-Schwinger spin sum of Eq. (6.33), the multipole form factors may be isolated and extracted. The appropriate combinations of $\overline{R}_\sigma{}^\mu{}_\tau(\vec{p}\,', \vec{p}; \Gamma)$ suitable for calculations employing the γ-matrix and metric conventions of Sakurai are

$$
\begin{aligned}
\mathcal{G}_{E0}(q^2) &= \frac{1}{3} \left(\overline{R}_1{}^4{}_1(\vec{q}_1, 0; \Gamma_4) + \overline{R}_2{}^4{}_2(\vec{q}_1, 0; \Gamma_4) + \overline{R}_3{}^4{}_3(\vec{q}_1, 0; \Gamma_4) \right) , && (6.64) \\
\mathcal{G}_{E2}(q^2) &= 2 \frac{M(E + M)}{|\vec{q}_1|^2} \left(\overline{R}_1{}^4{}_1(\vec{q}_1, 0; \Gamma_4) + \overline{R}_2{}^4{}_2(\vec{q}_1, 0; \Gamma_4) - 2\, \overline{R}_3{}^4{}_3(\vec{q}_1, 0; \Gamma_4) \right) , && (6.65) \\
\mathcal{G}_{M1}(q^2) &= -\frac{3}{5} \frac{E + M}{|\vec{q}_1|} \left(\overline{R}_1{}^3{}_1(\vec{q}_1, 0; \Gamma_2) + \overline{R}_2{}^3{}_2(\vec{q}_1, 0; \Gamma_2) + \overline{R}_3{}^3{}_3(\vec{q}_1, 0; \Gamma_2) \right) , && (6.66) \\
\mathcal{G}_{M3}(q^2) &= -4 \frac{M(E + M)^2}{|\vec{q}_1|^3} \left(\overline{R}_1{}^3{}_1(\vec{q}_1, 0; \Gamma_2) + \overline{R}_2{}^3{}_2(\vec{q}_1, 0; \Gamma_2) - \frac{3}{2}\, \overline{R}_3{}^3{}_3(\vec{q}_1, 0; \Gamma_2) \right) , && (6.67)
\end{aligned}
$$

where $\vec{q}_1 = (q, 0, 0)$. Equation (6.65) for $\mathcal{G}_{E2}$ isolates the spin matrix element $\langle\, \frac{3}{2} s' \,\big|\, \Sigma^{(2)}_0 \,\big|\, \frac{3}{2} s \,\rangle$. Smaller statistical uncertainties may be obtained by using the symmetry

$$
\overline{R}_2{}^4{}_2(\vec{q}_1, 0; \Gamma_4) = \overline{R}_3{}^4{}_3(\vec{q}_1, 0; \Gamma_4) . \tag{6.68}
$$

We define an average $\overline{R}^4_{\rm avg}$ as

$$
\overline{R}^4_{\rm avg}(\vec{q}_1, 0; \Gamma_4) = \frac{1}{2} \left[\overline{R}_2{}^4{}_2(\vec{q}_1, 0; \Gamma_4) + \overline{R}_3{}^4{}_3(\vec{q}_1, 0; \Gamma_4) \right] . \tag{6.69}
$$

With this definition the expression for $\mathcal{G}_{E2}(q^2)$ used in our simulations is

$$
\mathcal{G}_{E2}(q^2) = 2 \frac{M(E + M)}{|\vec{q}_1|^2} \left(\overline{R}_1{}^4{}_1(\vec{q}_1, 0; \Gamma_4) - \overline{R}^4_{\rm avg}(\vec{q}_1, 0; \Gamma_4) \right) . \tag{6.70}
$$

6.5 Lattice Techniques

The simulations are performed using the mean-field $\mathcal{O}(a^2)$-improved Luscher-Weisz [10] plaquette plus rectangle gauge action on a $20^3 \times 40$ lattice with periodic boundary conditions. The lattice spacing $a = 0.128$ fm is determined by the Sommer scale $r_0 = 0.50$ fm [72]. This large volume lattice ensures a good density of low-lying momenta which are key to giving rise to chiral nonanalytic behavior in the observables simulated on the lattice [59, 60, 61].

We perform a high-statistics analysis using a large sample of 400 configurations for our lightest eight quark masses. We also consider a subset of 200 configurations for our three heaviest quark masses to explore the approach to the heavy-quark regime. A subensemble bias correction is applied multiplicatively to the heavy quark results, by matching the central values of the ensemble averages at $\kappa = 0.12780$.

The error analysis is performed by a third-order, single-elimination jackknife.

For the quark fields, we use the Fat-Link Irrelevant Clover fermion action discussed in Chapter 4. Our notation uses the Pauli representation of the Dirac γ-matrices [73], where the γ-matrices are hermitian and $\sigma_{\mu\nu} = [\gamma_\mu, \ \gamma_\nu]/(2i)$. Fat links are constructed by performing $n_{\text{APE}} = 6$ sweeps of APE smearing, where in each sweep the weights given to the original link and the six transverse staples are 0.3 and $(0.7/6)$ respectively. The FLIC action is closely related to the mean-field improved clover (MFIC) fermion action in that the latter is described by Eqs. (4.31) and (4.33) with all fat-links replaced by untouched thin links and $F_{\mu\nu}$ defined by the 1×1-loop clover definition.

For fat links, the mean link $u_0 \approx 1$, indicating that perturbative renormalizations are small for smeared links and are accurately accounted for by small mean-field improvement corrections. As a result, mean-field improvement of the coefficients of the clover and Wilson terms of the fermion action is sufficient to accurately match these terms and eliminate $\mathcal{O}(a)$ errors from the fermion action [24]. An added advantage is that access to the light quark mass regime is enabled by the improved chiral properties of the FLIC fermion action [74].

Time slices are labeled from 1 to 40, and a fixed boundary condition at $t = 40$ is used for the fermions. An analysis of the pion correlator indicates that the effects of this boundary condition are negligible for $t \leq 30$, and all of our correlation-function fits are performed well within this regime.

Gauge-invariant Gaussian smearing [75, 76] in the spatial dimensions is applied at the source at $t = 8$ to increase the overlap of the interpolating operators with the ground

Table 6.1: Hadron masses in appropriate powers of GeV for various values of the hopping parameter, κ. Experimental values are indicated at the end of the table.

κ	m_π^2	N	Λ	Σ	Ξ
0.12630	0.9972(55)	1.829(8)	1.728(10)	1.700(9)	1.612(11)
0.12680	0.8947(54)	1.763(9)	1.681(10)	1.656(10)	1.586(12)
0.12730	0.7931(53)	1.695(9)	1.632(11)	1.566(11)	1.558(12)
0.12780	0.6910(35)	1.629(10)	1.584(10)	1.570(10)	1.531(10)
0.12830	0.5925(33)	1.554(10)	1.530(10)	1.521(10)	1.502(10)
0.12885	0.4854(31)	1.468(11)	1.468(11)	1.468(11)	1.468(11)
0.12940	0.3795(31)	1.383(11)	1.406(11)	1.417(11)	1.435(11)
0.12990	0.2839(33)	1.301(11)	1.347(11)	1.371(11)	1.404(11)
0.13205	0.2153(35)	1.243(12)	1.303(12)	1.341(12)	1.382(11)
0.13060	0.1384(43)	1.190(15)	1.256(13)	1.313(12)	1.359(11)
0.13080	0.0939(44)	1.159(21)	1.226(16)	1.296(14)	1.346(11)
experiment	0.0196	0.939	1.116	1.189	1.315

state while suppressing excited state contributions.

Tables 6.1 and 6.2 provide the kappa values used in our simulations, together with the calculated π, octet and the decuplet baryon masses. While we refer to m_π^2 to infer the quark masses, we note that the critical value where the pion mass vanishes is $\kappa_{\rm cr} = 0.13135$.

We select $\kappa = 0.12885$ to represent the strange quark in this simulation. At this κ the $s\bar{s}$ pseudoscalar mass is 0.697 GeV, which compares well with the experimental value of $2\,m_{\rm K}^2 - m_\pi^2 = (0.693\ {\rm GeV})^2$, motivated by leading order chiral perturbation theory.

6.5.1 Improved Conserved Vector Current

For the construction of the $\mathcal{O}(a)$-improved conserved vector current, we follow the technique proposed by Martinelli *et al.* [77]. The standard conserved vector current for Wilson-type fermions is derived via the Noether procedure

$$\begin{aligned} j_\mu^{\rm C} &\equiv \frac{1}{4}[\overline{\psi}(x)(\gamma_\mu - r)U_\mu(x)\psi(x+\hat{\mu}) \\ &+ \overline{\psi}(x+\hat{\mu})(\gamma_\mu + r)U_\mu^\dagger(x)\psi(x) \\ &+ (x \to x-\hat{\mu})]. \end{aligned} \tag{6.71}$$

Table 6.2: Decuplet baryon Masses in GeV for different quark masses indicated by the values of m_π^2 in GeV^2. Experimental values are indicated at the end of the table.

κ	${m_\pi}^2$	Δ	Σ^*	Ξ^*
0.12630	0.9972(55)	1.999(9)	1.908(10)	1.815(12)
0.12680	0.8947(54)	1.944(9)	1.871(11)	1.797(12)
0.12730	0.7931(53)	1.890(10)	1.834(11)	1.778(13)
0.12780	0.6910(35)	1.845(10)	1.807(11)	1.770(11)
0.12830	0.5925(33)	1.791(11)	1.771(11)	1.752(12)
0.12885	0.4854(31)	1.732(12)	1.732(12)	1.732(12)
0.12940	0.3795(31)	1.673(14)	1.693(13)	1.712(13)
0.12990	0.2839(33)	1.622(16)	1.659(15)	1.695(13)
0.13205	0.2153(35)	1.592(17)	1.638(15)	1.685(13)
0.13060	0.1384(43)	1.565(18)	1.620(16)	1.676(14)
0.13080	0.0939(44)	1.549(19)	1.609(16)	1.670(13)
experiment	0.0196	1.232	1.382	1.531

The $O(a)$-improvement term is also derived from the fermion action and is constructed in the form of a total four-divergence, preserving charge conservation. The $O(a)$-improved conserved vector current is

$$j_\mu^{\mathrm{CI}} \equiv j_\mu^{\mathrm{C}}(x) + \frac{r}{2} C_{CVC}\, a \sum_\rho \partial_\rho(\overline{\psi}(x)\sigma_{\rho\mu}\psi(x)) \,, \tag{6.72}$$

where C_{CVC} is the improvement coefficient for the conserved vector current and we define

$$\partial_\rho(\overline{\psi}(x)\psi(x)) \equiv \overline{\psi}(x)(\overleftarrow{\nabla}_\rho + \overrightarrow{\nabla}_\rho)\psi(x) \,, \tag{6.73}$$

where the forward and backward derivatives are defined as

$$\begin{aligned}
\overrightarrow{\nabla}_\mu \psi(x) &= \frac{1}{2a}\Big[U_\mu(x)\,\psi(x+\hat{\mu}) \\
&\qquad\qquad -U_\mu^\dagger(x-\hat{\mu})\,\psi(x-\hat{\mu})\Big] \,, \\
\overline{\psi}(x)\overleftarrow{\nabla}_\mu &= \frac{1}{2a}\Big[\overline{\psi}(x+\hat{\mu})\,U_\mu^\dagger(x) \\
&\qquad\qquad -\overline{\psi}(x-\hat{\mu})\,U_\mu(x-\hat{\mu})\Big] \,.
\end{aligned}$$

The terms proportional to the Wilson parameter r in Eq. (6.71) and the four-divergence in Eq. (6.72) have their origin in the irrelevant operators of the fermion action and vanish in the continuum limit. Nonperturbative improvement is achieved by constructing these terms with fat-links. As we have stated, perturbative corrections are small for fat-links and the use of the tree-level value for $C_{CVC} = 1$ together with small mean-field improvement corrections ensures that $\mathcal{O}(a)$ artifacts are accurately removed from the vector current. This is only possible when the current is constructed with fat-links. Otherwise, C_{CVC} needs to be appropriately tuned to ensure all $\mathcal{O}(a)$ artifacts are removed.

In order to suppress contributions from excited states, large Euclidean times are required, both following the source at t_0, and following the current insertion at t_1. Our two-point function analysis indicates that the ground state is isolated well by $t = 14$, largely due to an excellent selection for the source smearing parameters. Therefore the current insertion is performed at $t_1 = 14$.

6.5.2 Improved Unbiased Estimators

The two and three-point correlation functions are defined as averages over an infinite ensemble of equilibrium gauge field configurations, but are approximated by an average over a finite number of configurations.

To minimize the noise in the results, we exploit the parity of the correlation functions [78]

$$G(\vec{p}\,', \vec{p}, \vec{q}; \Gamma) = s_P\, G(-\vec{p}\,', -\vec{p}, -\vec{q}; \Gamma), \qquad s_P = \pm 1, \tag{6.74}$$

and calculate them for both $\vec{p}$, $\vec{p}\,'$, $\vec{q}$ and $-\vec{p}$, $-\vec{p}\,'$, $-\vec{q}$.

While this requires an extra matrix inversion to determine $\widehat{S}(x_2, 0; t_1, -\vec{q}, \mu)$, the ratio of three- to two-point functions is determined with a substantial reduction in the statistical uncertainties. The improvement is better than that obtained by doubling the number of configurations.

Similarly, the link variables $\{U\}$ and $\{U^*\}$ are gauge field configurations of equal weight, and therefore we account for both sets of configurations in calculating the correlation functions [79].

With the fermion matrix property

$$M(\{U^*\}) = \left(\widetilde{C} M(\{U\}) \widetilde{C}^{-1}\right)^*, \tag{6.75}$$

it follows that

$$S(x, 0; \{U^*\}) = \left(\widetilde{C} S(x, 0; \{U\}) \widetilde{C}^{-1}\right)^*, \tag{6.76}$$

$$\widehat{S}(x, 0; t, \vec{q}, \mu; \{U^*\}) = \left(\widetilde{C} \widehat{S}(x, 0; t, -\vec{q}, \mu; \{U\}) \widetilde{C}^{-1}\right)^*, \tag{6.77}$$

and therefore the correlation functions are purely real provided

$$\Gamma = s_C \left(\widetilde{C} \Gamma \widetilde{C}^{-1} \right)^* \quad \text{and} \quad s_C = s_P . \tag{6.78}$$

These conditions are satisfied with the selections for Γ indicated in Eq. (6.31).

In summary, the inclusion of both $\{U\}$ and $\{U^*\}$ configurations in the calculation of the correlation functions provides an improved unbiased estimate of the ensemble average properties incorporating parity symmetry and significantly reducing statistical fluctuations.

6.5.3 Fit Regime Selection Criteria

In fitting the correlation functions, the covariance-matrix based χ^2 per degree of freedom (dof) plays a central role. The correlated χ^2/dof is given by

$$\begin{aligned} \frac{\chi^2}{\text{dof}} &= \frac{1}{N_t - M} \sum_{i=1}^{N_t} \sum_{j=1}^{N_t} \\ &\quad (y(t_i) - T(t_i))\, C^{-1}(t_i, t_j) \left(y(t_j) - T(t_j) \right) , \end{aligned} \tag{6.79}$$

where, M is the number of parameters to be fitted, N_t is the number of time slices considered, $y(t_i)$ is the configuration average value of the dependent variable at time t_i that is being fitted to a theoretical value $T(t_i)$, and $C(t_i, t_j)$ is the covariance matrix.

The elements of the covariance matrix are estimated via the jackknife method [80]

$$C(t_i, t_j) = \frac{N_c - 1}{N_c} \sum_{m=1}^{N_c} \left[\overline{y_m}(t_i) - \overline{\overline{y}}(t_i) \right] \left[\overline{y_m}(t_j) - \overline{\overline{y}}(t_j) \right] , \tag{6.80}$$

$$= (N_c - 1) \times \left\{ \frac{1}{N_c} \sum_{m=1}^{N_c} \overline{y_m}(t_i)\, \overline{y_m}(t_j) - \overline{\overline{y}}(t_i)\, \overline{\overline{y}}(t_j) \right\} \tag{6.81}$$

where N_c is the total number of configurations and $\overline{y_m}(t_i)$ is the jackknife ensemble average of the system after removing the m_{th} configuration. $\overline{\overline{y}}(t_i)$ is the average of all such jackknife averages, given by

$$\overline{\overline{y}}(t_i) = \frac{1}{N_c} \sum_{m=1}^{N_c} \overline{y_m}(t_i) . \tag{6.82}$$

In the process of selecting the fit regimes, numerous fits are performed over a variety of start times and a variety of time durations. The following criteria are taken into account in selecting the preferred fit regime:

1. The χ^2/dof is monitored and plays a significant role in determining the start time of the fit. Values within the range 0.5 to 1.5 are preferred and it is often possible to select a regime providing a perfect fit measure of 1. Start times for which the χ^2/dof increases significantly as the duration of the regime is increased are discarded. In practice, the χ^2/dof sets a lower bound for the start time, and other criteria may lead to a later start time for the fit.

2. In some cases a monotonic systematic drift can be observed in the ratio of correlation functions Eq. (6.62) which otherwise should be constant in time. Often the drift is sufficiently small to provide a $\chi^2/dof < 1.5$. In these few cases, a later start time is selected to ensure that sufficient Euclidean time evolution has occurred to accurately isolate the ground state, suppressing systematic errors at the expense of larger statistical errors.

3. As the quarks become lighter, the spacing between the ground and first excited states of the baryon spectrum becomes larger [79, 81], due to the more rapid reduction in the mass of the lower-lying state. This provides improved exponential suppression of excited-state contaminations. Hence, as one approaches the light quark mass regime, a monotonic reduction in the starting time-slice of the fit regime may be possible.

4. As the quark masses become lighter, the signal is lost to noise at earlier times. Hence the final time slice of the fit window is also monotonically decreased as the quarks become lighter. We typically consider fit regimes of three to five time slices and preferably the latter when the signal is not obviously lost to noise.

5. For quark masses lighter than the strange quark mass, the splittings between adjacent quark masses are calculated and fit using the same techniques. By considering adjacent splittings, excited-state contributions which are less dependent on the quark mass (see item 3 above) are suppressed. In practice, good χ^2/dof are found one to two time slices earlier.

A precise examination of the environment sensitivity of quark-sector contributions to baryon electromagnetic properties lies at the core of this investigation.

For example, the doubly-represented u quark in the proton is to be compared with the doubly-represented u quark in Σ^+; the singly-represented u quark in the neutron with the u quark in Ξ^0. Similarly, it is interesting to compare the strange and light quark sectors of Ξ^- with those of Λ. Conventional models reverse the ordering of the observed magnetic moments.

After the consideration of the preceding criteria, the fit regimes are unified for each of the quark sector contributions wherever possible.

This comparison is done for each value of κ governing the quark mass, reducing systematic errors associated with choosing different time-fitting regimes for similar quantities.

For example, for the case of the doubly-represented u quark in the proton and Σ^+, it is possible to equate the fit regimes for all but the two lightest quark masses where the χ^2/dof insists on different fit regimes.

Chapter 7

Results-Octet baryons

7.1 Form Factors

In general, the baryon form factors are calculated on a quark-sector by quark-sector basis with each sector normalized to the contribution of a single quark with unit charge. Hence to calculate the corresponding baryon property, each quark sector contribution should be multiplied by the appropriate charge and quark number. Under such a scheme for a generic form factor f, the proton form factor f_p is obtained from the u- and d-quark sectors normalized for a single quark of unit charge via

$$f_p = 2 \times \frac{2}{3} \times f_u + 1 \times \left(-\frac{1}{3}\right) \times f_d \,. \tag{7.1}$$

The electric form factor of the proton and contributions from the u- and d-quark sectors are plotted in Fig. 7.1 as a function of Euclidean time at the $SU(3)$-flavor limit. Here, charge and quark number factors have been included such that the proton result is simply the sum of the illustrated quark sectors. The lines indicate the time slices selected for the fit using the considerations of Sec. 6.5.3.

We find that substantial Euclidean time evolution is required following the current insertion to obtain acceptable values of the χ^2/dof; in this case seven time slices following the current insertion at $t_1 = 14$.

For light quark masses lighter than the strange quark mass, we fit the change in the form factor ratios of Eq. (6.62) from one quark mass to the next and add this to the previous result at the heavier quark mass. All the data that is used to calculate the form factors is originating from the same system and hence the data is highly likely to be extremely correlated. Taking difference of successive quark masses removes the correlated errors and leaves a clean signal to fit. This is more important in the lower quark

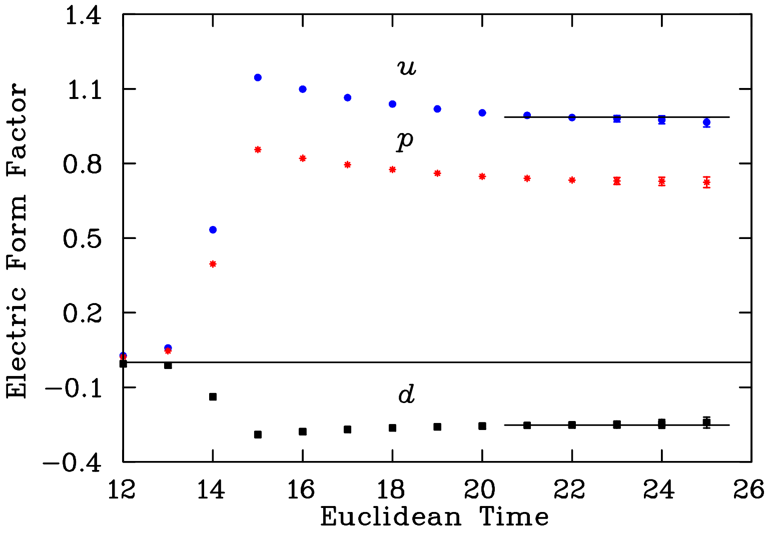

Figure 7.1: Electric form factor of the proton and its quark sectors (including charge and quark number factors) at $Q^2 = 0.227(2)$ GeV^2 as a function of Euclidean time (t_2) for $m_\pi^2 = 0.4854(31)$ GeV^2, which corresponds to the $SU(3)$-flavor limit. The lines indicate the fitting windows and the best fit value.

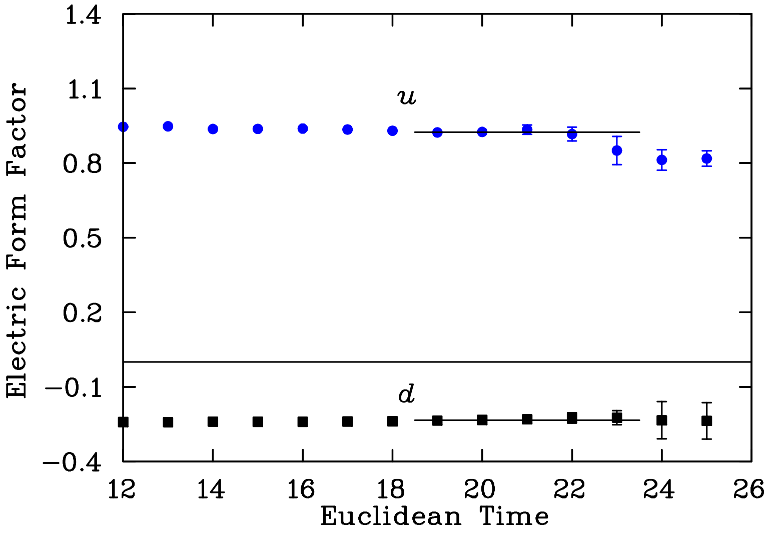

Figure 7.2: Quark sector contributions (including charge and quark number factors) to the electric form factor of the proton at $Q^2 = 0.227(2)$ GeV^2 as a function of Euclidean time, t_2, for the ninth quark mass where $m_\pi^2 = 0.2153(35)$ GeV^2. The correlator is obtained from the splitting between the ninth and eighth quark mass states. The lines indicate the fitting windows and the best fit value.

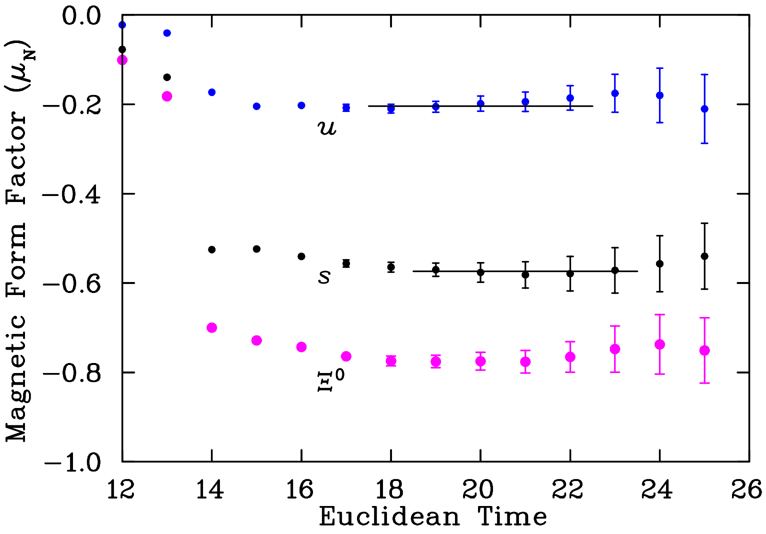

Figure 7.3: Magnetic form factors of Ξ^0 and its quark sectors (including charge and quark number factors) at $Q^2 = 0.227(2)$ GeV^2 as a function of Euclidean time (t_2) for $m_\pi^2 = 0.4854(31)$ GeV^2, which corresponds to the $SU(3)$-flavor limit. The lines indicate the fitting windows and the best fit value.

masses where it is more difficult to realize a reasonable flattening of data conducive for fitting. Therefore we used this technique for quark masses lighter than the strange quark mass.

Figure 7.2 shows the fitting of the electric form factor splitting for the proton between the eighth and ninth quark masses, the latter having $m_\pi^2 = 0.2153$ GeV^2. The improvement of the plateau is apparent in Fig. 7.2. Still, substantial Euclidean time evolution is required to obtain an acceptable χ^2/dof. The onset of noise at this lighter quark mass is particularly apparent at time slice 24 for the d sector. Tables A.1 to A.4 list the electric form factors for all the octet baryons at the quark level for the eleven quark masses considered. In the tables, the selected time frame, the fit value and the associated χ^2/dof are indicated.

Turning now to the magnetic form factors, Fig. 7.3 shows the magnetic form factor of Ξ^0 and its quark sectors (including charge and quark number factors) as a function of Euclidean time at the $SU(3)$-flavor limit. Preferred fit windows following from the criteria of Sec. 6.5.3 and best fit values are indicated.

Here the conversion from the natural magneton, $e/(2\,m_B)$ where the mass of the baryon under investigation appears, to the nuclear magneton, $e/(2\,m_N)$ where the phys-

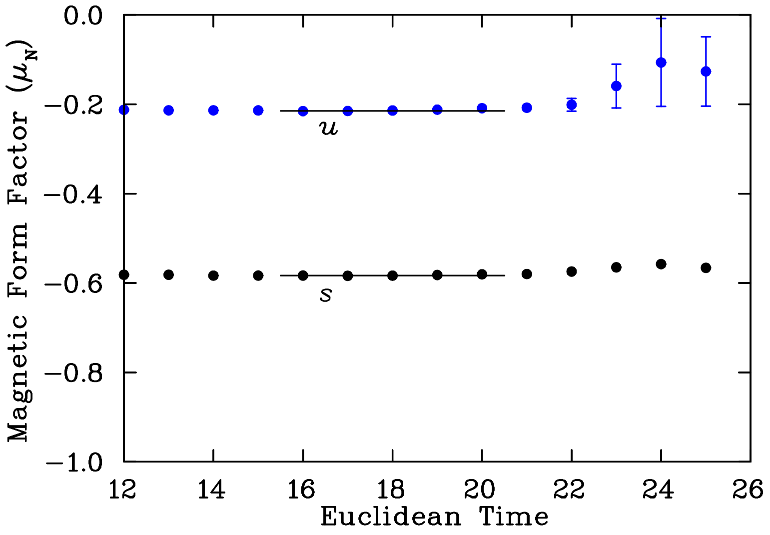

Figure 7.4: Quark sector contributions (including charge and quark number factors) to the magnetic form factor of Ξ^0 at $Q^2 = 0.227(2)$ GeV^2 as a function of Euclidean time, t_2, for the ninth quark mass where $m_\pi^2 = 0.2153(35)$ GeV^2. The correlator is obtained from the splitting between the ninth and eighth quark mass states. The lines indicate the fitting windows and the best fit value.

ical nucleon mass appears, has been done by multiplying the lattice form factor results by the ratio m_N/m_B. In this way the form factors are presented in terms of a constant unit *i.e.* the nuclear magneton.

The negative contribution of the u quark to the total form factor indicates that its spin is on average opposite to that of the doubly represented s quarks. This, as well the relative magnitude of the contributions, is in qualitative agreement with simple constituent quark models based on $SU(6)$ spin-flavor symmetry.

In Fig. 7.4 we present the Euclidean time dependence of the the magnetic form factors of Ξ^0 calculated at the ninth quark mass where $m_\pi^2 = 0.2153(35)$ GeV^2. Again the early onset of acceptable plateau behavior is apparent here.

Results for the quark-sector contributions to the magnetic form factors of octet baryons are summarized in Tables A.5 to A.8.

7.2 Charge Radii

To make contact with the extensive phenomenology of the field, our results for the electric form factors are expressed in terms of charge radii. It is well known that the experimentally measured electric (and magnetic) form factor of the proton is described well by a dipole ansatz at small Q^2

$$\mathcal{G}_E(Q^2) = \frac{\mathcal{G}_E(0)}{\left(1 + Q^2/m^2\right)^2} \, ; \quad Q^2 \geq 0 \, , \tag{7.2}$$

where m characterizes the size of the proton. This behavior has also been observed in recent lattice calculations [82] where many momentum transfers have been considered. Using this observation, together with

$$\left\langle r_E^2 \right\rangle = -6 \, \frac{d}{dQ^2} \, \mathcal{G}_E(Q^2) \, \Big|_{Q^2=0} \, , \tag{7.3}$$

we arrive at an expression which allows us to calculate the electric charge radius of a baryon using our two available values of the Sachs electric form factor ($\mathcal{G}_E(Q^2_{\rm min})$, $\mathcal{G}_E(0)$), namely

$$\frac{\left\langle r_E^2 \right\rangle}{\mathcal{G}_E(0)} = \frac{12}{Q^2} \left(\sqrt{\frac{\mathcal{G}_E(0)}{\mathcal{G}_E(Q^2)}} - 1 \right) . \tag{7.4}$$

While Eq. (7.2) is suitable for a charged baryon, alternative forms must be considered for neutral baryons where $\mathcal{G}_E(0) = 0$.

However, we have direct access to the charge distributions of the individual quark sectors, a subject receiving tremendous experimental attention in the search for the role of hidden flavor in baryon structure. In this case Eq. (7.4) may be applied to each quark sector providing an opportunity to determine the charge radii on a sector by sector basis.

For neutral baryons it becomes a simple matter to construct the charge radii by first calculating the charge radii for each quark sector. These quark sectors are then combined using the appropriate charge and quark number factors as described in Sec. 7.1 to obtain the total baryon charge radii. Indeed, all baryon charge radii including the charged states are calculated in this manner.

Tables A.9 to A.12 provide the electric charge radii of the octet baryons and their quark sector contributions normalized to single quarks of unit charge.

7.2.1 Quark sector charge radii

We begin with an examination of the quark contributions to baryon charge radii. The results are reported for single quarks of unit charge. Of particular interest are the contributions of similar quarks experiencing different environments. Traditionally, quark models of hadron structure neglected such environment sensitivity. However, such environment sensitivity is manifest in chiral effective field theory. The finite kaon mass

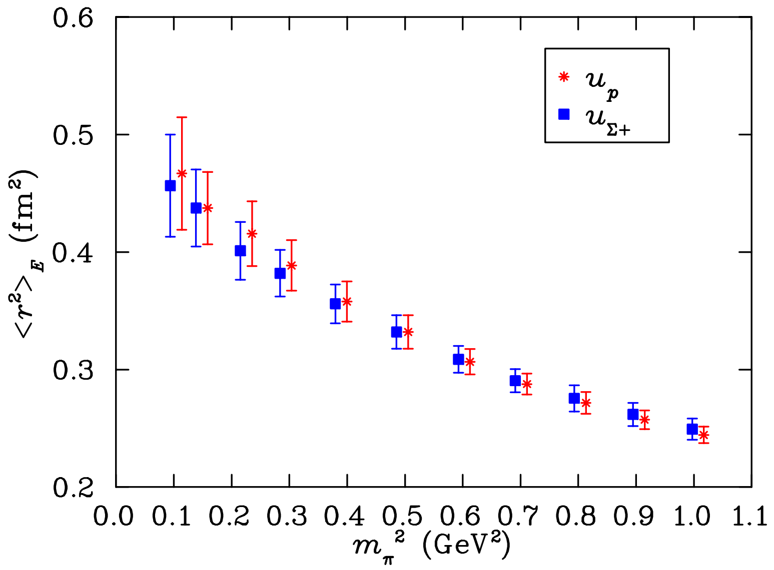

Figure 7.5: Electric charge radii of u_p, and u_{Σ^+} as a function of m_π^2 representing the quark masses considered in the simulation. The results for u_p are offset for clarity.

in the chiral limit renders the kaon's contributions to curvature almost trivial relative to the pion.

Figure 7.5 displays the charge radii of the u-quark distribution in the proton and compares this with the u-quark distribution in Σ^+. The $SU(3)$-flavor limit is manifest at $m_\pi^2 \sim 0.5$ GeV^2. The replacement of a d-quark in the proton, by an s quark in Σ^+ gives rise to only a small environment sensitivity in the u-quark properties.

Referring to the chiral coefficients of Table A.38, the negative value of χ for u_p indicates that the charge radius of the u quark distribution in the proton should diverge to positive infinity in the chiral limit. A physical understanding of this is made obvious by considering the virtual transition $p \to n\pi^+$, which at the quark level can be understood as $(uud) \to (udd)(\bar{d}u)$. In the chiral limit, the π^+ carries the u quark to infinity such that u-quark charge distribution radius in the proton diverges.

In the case of the u quark in Σ^+, the coefficient of the logarithmic divergence is zero in the π channel and hence no divergence is expected. While there is a significant coefficient for transitions to ΞK, the increased mass of the Ξ baryon makes this channel unfavorably suppressed.

The results in Fig. 7.5 for u_p exhibit an upward trend and increasing curvature with reducing quark mass. The u_{Σ^+} rises more slowly. Hence these results are in qualitative

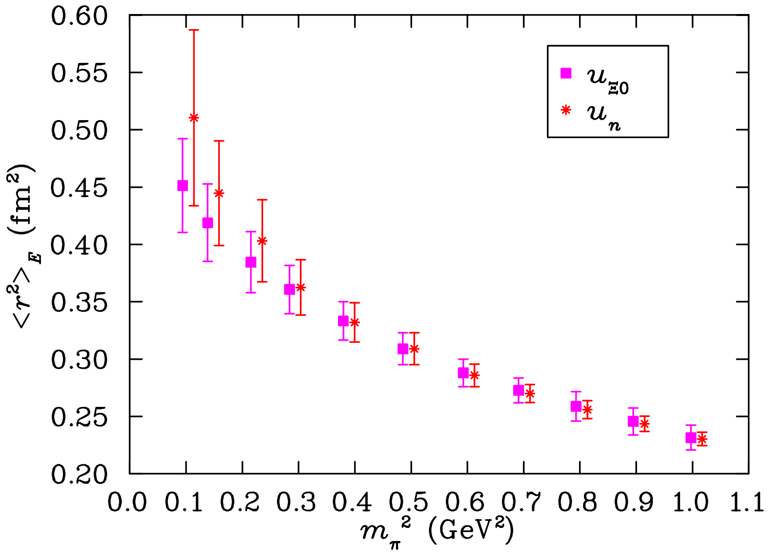

Figure 7.6: Charge radii of u_n and u_{Ξ^0} as a function of m_π^2. The data for the u_n are offset for clarity.

agreement with the LNA expectations of chiral effective field theory.

Figure 7.6 displays the electric charge radii of the u quark in the neutron (u_n) and in Ξ^0 (u_{Ξ^0}) as a function of m_π^2.

Here we observe that the charge radii of u_n and u_{Ξ^0} are nearly equal at heavy quark masses, but in the approach to the chiral limit they differ. The light d-quark environment of the u quark in the neutron provides enhanced chiral curvature as the chiral limit is approached.

The true nature of the underlying physics is much more subtle. From Table A.38, we see that the quenched coefficient (last column) for the u quark in the neutron is positive in the π channel, from which we can deduce that the charge radius should actually diverge to negative infinity in the chiral limit.

Physically this can be understood by looking at the quark contributions to the virtual transition $n \rightarrow p\pi^-$ which gives rise to this divergence. In this case one has $(ddu) \rightarrow (duu)(\overline{u}d)$. In the chiral limit, the mass of the pion approaches zero such that the π^- carries a $\overline{u}$ quark to infinity. Since the d quark is ignored while calculating the u quark contribution (*i.e.* the electric charge of the d quark may be thought of as zero), the entire charge of the pion comes from the $\overline{u}$ quark, thus taking the u-quark charge distribution radius to negative infinity. However, Fig. 7.6 shows no such trend.

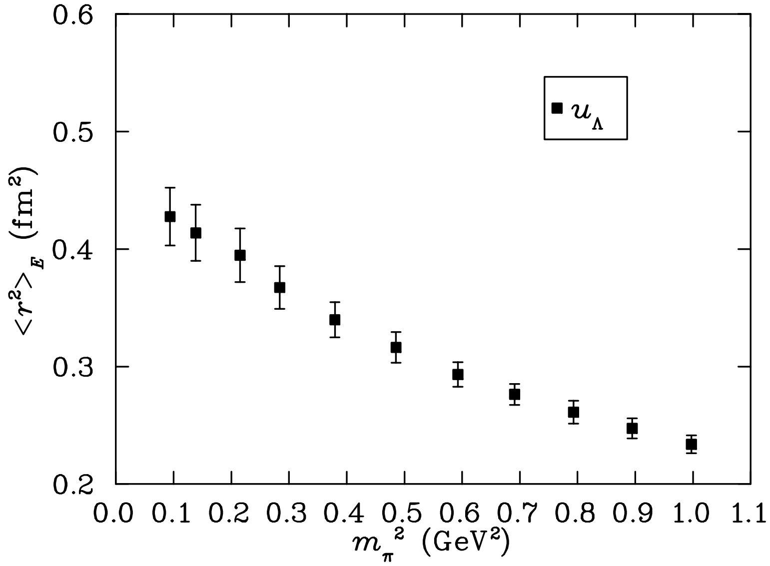

Figure 7.7: Charge radius of u_{Λ^0} as a function of m_π^2.

The coefficient χ for u_{Ξ^0} is zero in the π channel, indicating that there should be no logarithmic divergence in the chiral limit. However it does have a substantial positive coefficient in the favorable ΣK channel, indicating the possibility of downward curvature as the chiral limit is approached. Again, Fig. 7.6 shows no hint of downward curvature.

While the statistical error bars are sufficiently large to hide such a turn over, there are other interpretations. One possibility is that we are not yet in the true chiral regime where such physics is manifest. Indeed, the divergence of the *u*-quark charge distribution to negative infinity may only reveal itself at quark masses *lighter* than the physical quark masses.

Alternatively, one might regard this particular case to be somewhat exceptional. It is the only channel in which chiral-loop physics is expected to oppose the natural broadening of a distribution's Compton wavelength. On the lattice, the finite volume restricts the low momenta of the effective field theory to discrete values. It may be that this lattice artifact prevents one from building up sufficient strength in the loop integral to counter the Compton broadening. In this case it would be impossible to observe the divergence of $u_n \to -\infty$ at any quark mass. It will be interesting to resolve this discrepancy with quantitative effective field theory calculations.

Figure 7.7 reports our results for the charge distribution radius of a *u* quark in Λ as a function of m_π^2. The chiral coefficient for this is zero in the π channel and hence no

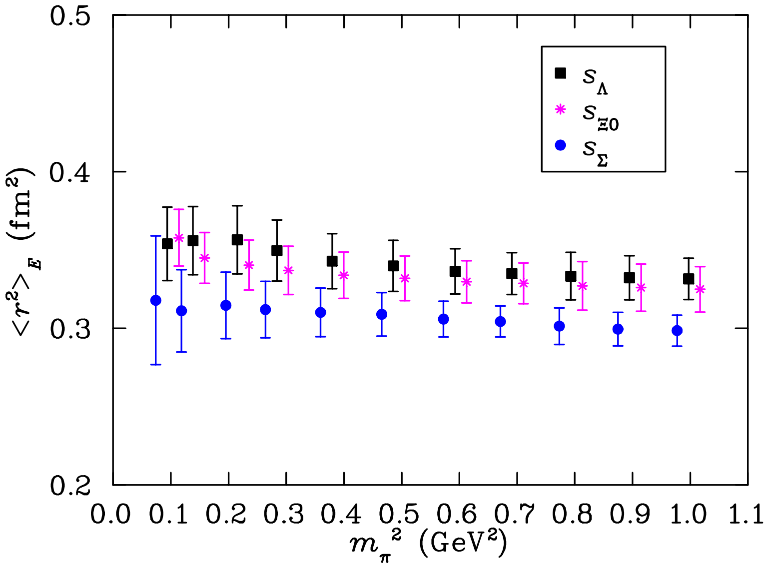

Figure 7.8: Charge distribution radii of s_Λ, s_{Ξ^0} and s_{Σ^0} as a function of m_π^2. The data for s_{Ξ^0} and s_Λ are plotted for shifted m_π^2 values.

divergence is expected. However, there is significant strength for downward curvature in the energetically favorable NK channel. Indeed, the approach to the chiral limit is remarkably linear and contrasts the upward curvature observed for other light quark flavor s. Hence our results are in qualitative agreement with the expectations of QχPT. Figure 7.8 illustrates the charge distribution radius of strange quarks in Λ^0, Ξ^0 and Σ^0. In our simulations the strange quark mass is held fixed and therefore any variation observed in the results is purely environmental in origin. All three distributions suggest a gentle dependence on the mass of the environmental light quarks.

However, the environmental flavor -symmetry dependence of the strange quark distributions is quite marked. When the environmental quarks are in an isospin 0 state in the Λ, the strange quark distribution is broad. On the other hand, when the environmental quarks are in an isospin 1 state in Σ baryons, the distribution radius is significantly smaller.

In the case of strange quark distributions, the LNA contributions are exclusively from transitions involving the kaon. Therefore significant curvature is not expected. On the other hand, one might expect broader distributions in cases where a virtual transition is possible in quenched QCD. Referring to Table A.38, one sees that both s_Λ and s_Ξ have strong transitions to the energetically favorable KN and $K\Sigma$ channels respectively. The coefficients are negative such that the virtual transitions will act to enhance the charge distributions. This is not the case for s_Σ where the sign is positive and the

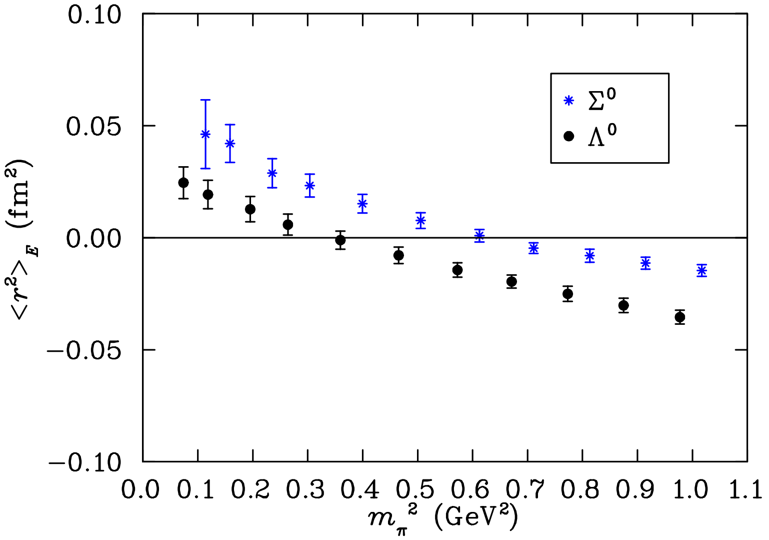

Figure 7.9: Charge radii of Σ^0 and Λ^0 as a function of m_π^2. The data for Σ^0 is offset to the right for clarity.

transition is to the energetically unfavored $K\Xi$ channel. In summary, QχPT suggests the charge distributions for s_Λ and s_Ξ will be larger than for s_Σ. This is exactly what is observed in Figure 7.8.

7.2.2 Baryon charge radii

The flavor -symmetry dependence of *uds*-quark distributions in Σ^0 and Λ^0 is particularly manifest in Fig. 7.9. Here the interplay between the light-quark sector with effective charge 1/3 and the strange sector with charge −1/3 is revealed.

At the $SU(3)$ flavor -symmetric point ($m_\pi^2 \sim 0.5$ GeV^2) where the strange and light quarks have the same mass and the Λ and Σ are degenerate in mass, neither charge radius is zero. This very nicely reveals different charge distributions for the quark sectors described in the previous section.

In constituent quark models, this flavor dependence would be described in terms of spin-dependent forces. In the Λ^0 where a scalar diquark can form between the non-strange pair, the charge radius is dominated by the broader strange-quark distribution at the $SU(3)$-flavor symmetric point. This is contrasted by the Σ^0 where scalar-diquark pairing would occur between strange and non-strange quarks, acting to constrict the strange quark distribution in Σ as seen in Fig. 7.8. In addition, hyperfine repulsion in the non-strange quark sector leads to a broader distribution for the light quark sector

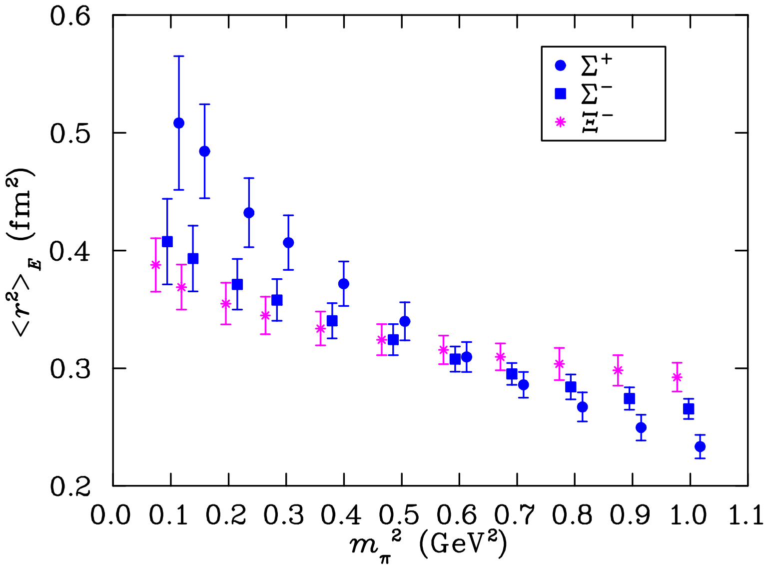

Figure 7.10: Charge radii of Σ^+, Σ^- and Ξ^- as a function of m_π^2. The Ξ^- and Σ^- are offset to the left and right respectively. For the Σ^- and Ξ^- the magnitudes are plotted without considering the negative charge factor.

as indicated in Tables A.11 and A.10. As compelling as this discussion is, this line of reasoning suggests the decuplet baryon states should have broader quark distributions [65] as scalar-diquark clusters do not dominate there. However, the results from analysis of decuplet baryon structure on the same lattice configurations explored here and discussed in Chapter 8, do not reveal broader quark distributions. For this reason, we consider our discussion of virtual transitions in the context of effective field theory in the previous section to be a more relevant description of the underlying physics.

Ultimately, as the chiral limit is approached, the light quark distribution broadens and dominates the charge radii for both baryons. However, the charge distribution of the Σ^0 is much broader and reflects our discussion of the quark sector contributions. In particular, the LNA contributions of QχPT act to suppress the distribution of u_Λ and enhance s_Λ, whereas the LNA contributions to Σ^0 are relatively suppressed either by having small coefficients or having energetically unfavorable transitions in the kaon channel. This suppression of u_Λ and enhancement s_Λ combines to give a strong net effect of suppressing the charge radius of the Λ^0.

The hyperon charge states, Σ^- and Ξ^- have chiral coefficients which vanish in quenched QCD. Similarly, Σ^+ has no contributions from virtual pion transitions. The one case, where there is a substantial coefficient, is suppressed energetically. Figure 7.10 displays our simulation results for the electric charge distribution radii of these

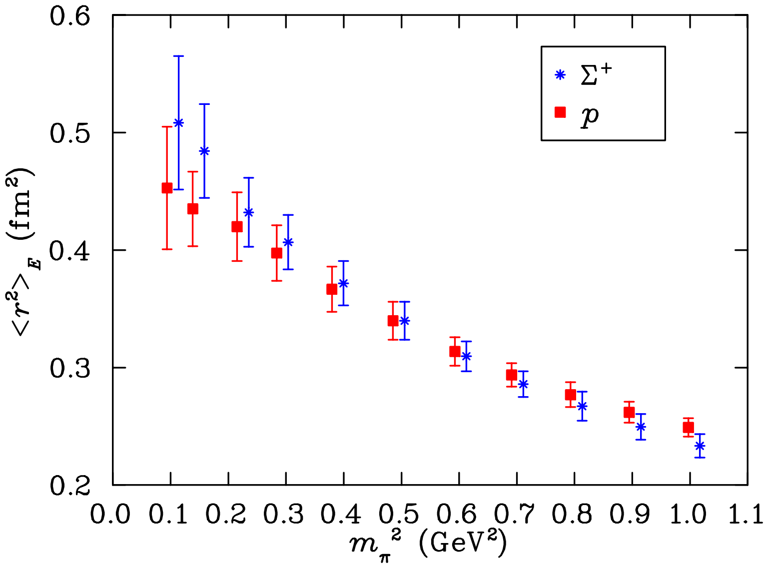

Figure 7.11: Charge radii of the proton and Σ^+ as a as a function of m_π^2. Σ^+ charge radius is offset for clarity.

hyperons as a function of m_π^2. The ordering of the charge radii as the chiral limit is approached is explained by the more localized strange quark distribution.

Figures 7.9 and 7.10 show our results for the electric charge radius of Σ^0, Λ^0, Σ^+, Σ^- and Ξ^- charge radii as a function of m_π^2. The quenched chiral coefficients for these baryons are zero in the π channel, and hence we expect no divergence in the chiral limit. None of them show any tendency to diverge, and they exhibit a monotonic increase with decreasing quark mass.

The quenched chiral coefficients for Σ^- and Ξ^- are identically zero in all channels, so they should ideally have no non-analytic behavior and should be completely analytic functions of m_π^2.

Experimentally measured value of $\langle r_E^2 \rangle$ for Σ^- is 0.608 ± 0.12 fm^2. The magnitude of the lattice result for the same at the lightest quark mass is 0.410(37) fm^2. The charge radius needs a lot of curvature to reach the experimental value in the chiral limit. This loss of information would be mainly due to the quenching effects.

Figure 7.11 compares the charge radii of Σ^+ with the proton. The charge radii of these baryons match at the $SU(3)$ flavor limit where $m_\pi^2 \sim 0.5$ GeV^2 as required. As the chiral limit is approached, the smaller charge distribution of the heavier negatively-charged strange quark acts to make the Σ^+ larger. This is manifest in the simulation

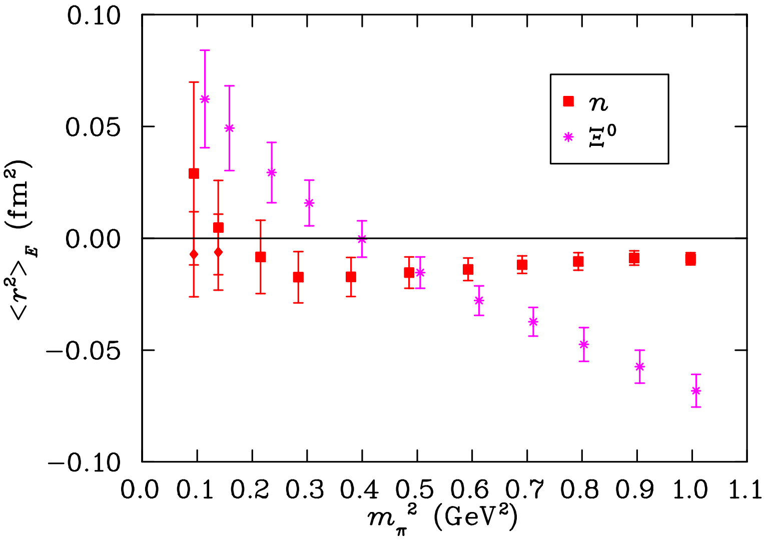

Figure 7.12: Charge radii of the neutron and Ξ^0 as a function of m_π^2. Charge radius of the Ξ^0 are shifted to the right for clarity. Diamonds at the lowest two quark masses denote the neutron charge radii calculated using slightly different time slices for fitting. Asymmetric error bars for the neutron charge radius are described in the text.

results.

While the Σ^+ is not expected to display chiral curvature, the proton charge radius presents one of the more favorable opportunities to observe a hint of the logarithmic divergence to be encountered in the chiral and infinite-volume limits of quenched QCD. However, there is no hint of chiral curvature in favor of the proton over the Σ^+.

The origin of this discrepancy is once again traced to the singly-represented *u*-quark in the neutron, or more specifically in this case, the singly-represented *d*-quark in the proton. As highlighted in the discussion surrounding Fig. 7.5, there is a hint of increased curvature for the doubly-represented *u*-quark in the proton over that in Σ, in accord with chiral effective field theory. But this is hidden in the proton charge radius due to the absence of the anticipated curvature of the singly-represented quark in the nucleon, as highlighted in the discussion surrounding Fig. 7.6.

Similarly, the ultimate divergence of the neutron charge radius to negative infinity via $n \to p\pi^-$ is not yet manifest. Rather a crossing of the central values into positive values of squared charge radii is revealed in Fig. 7.12. Still, the statistical errors remain consistent with negative values.

The crossing of the central values of the squared neutron charge radius into positive values led us to further examine our selection of fit regime in our correlation function analysis. Our concern is that noise in the correlation function may be distorting the fit. Hence, we have also considered fits including $t = 15$, immediately following the point-split current insertion centered at $t = 14$. While we prefer to allow some Euclidean time evolution following the current insertion, this systematic uncertainty is reflected in the asymmetric error bar of Fig. 7.12 for the lightest two neutron charge radii.

To summarize, we have explored the electric form factors of the baryon octet and their quark sector contributions at light quark masses approaching the chiral regime. The unprecedented nature of our quark masses is illustrated in Fig. 7.13 which compares the present results for the proton charge radius with the previous state of the art [51, 83]. Here the static quark potential has been used to uniformly set the scale among all the results. The small values of the early results are most likely due to the small physical lattice volumes necessitated at that time. The precision afforded by 400 $20^3 \times 40$ lattices is manifest.

We have discovered that all baryons having non-vanishing energetically-favorable couplings to virtual meson-baryon transitions tend to be broader than those which do not. This qualitative realization provides a simple explanation for the patterns revealed in our quenched-QCD simulations.

Still, evidence of chiral *curvature* on our large-volume lattice is rather subtle in general and absent in the exceptional case of the singly-represented quark in the neutron or Ξ. In this case, it is thought that the restriction of momenta to discrete values on the finite-volume lattice prevents the build up of strength in the loop integral of effective field theory. Without sufficient strength, the Compton broadening of the distribution will not be countered as the chiral limit is approached.

7.3 Magnetic Moments

The magnetic moment μ is provided by the magnetic form factor at $Q^2 = 0$, $\mathcal{G}_M(0)$, with units of the natural magneton, $\mu_B = e/(2\,M_B)$, where M_B is the mass of the baryon

$$\mu = \mathcal{G}_M(0)\,\frac{e}{2M_B}\,. \tag{7.5}$$

While we could present a detailed discussion of the magnetic form factors summarized in Sec. 7.1, a more interesting discussion of the results is facilitated via the magnetic moment where chiral nonanalytic behavior takes on a simple functional form and a vast collection of phenomenology is available to provide a context for our results.

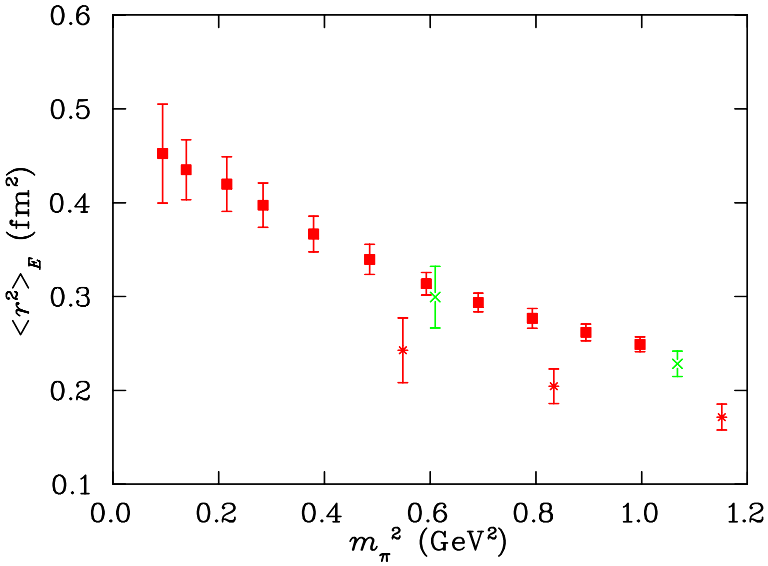

Figure 7.13: The proton charge radius is compared with previous state of the art lattice simulation results in quenched QCD. The solid squares indicate current lattice QCD results with FLIC fermions. The stars indicate the lattice results of [51] while the crosses indicate the results of [83], both of which use the standard Wilson actions for the gauge and fermion fields.

Since the magnetic form factors must be calculated at a finite value of momentum transfer, Q^2, the magnetic moment must be inferred from our results, $\mathcal{G}_M(Q^2)$, obtained at the minimum non-vanishing momentum transfer available on our periodic lattice. The Q^2 dependence of lattice results from the QCD-SF collaboration [82] are described well by a dipole. Phenomenologically this is a well established fact for the nucleon at low momentum transfers.

However, we will take an even weaker approximation and assume only that the Q^2 dependence of the electric and magnetic form factors is similar, without stating an explicit functional form for the Q^2 dependence. This too is supported by experiment where the proton ratio $\frac{\mathcal{G}_M(Q^2)}{\mu \mathcal{G}_E(Q^2)} \simeq 1$ for values of Q^2 similar to that probed here. In this case

$$\mathcal{G}_M(0) = \frac{\mathcal{G}_M(Q^2)}{\mathcal{G}_E(Q^2)} \mathcal{G}_E(0) . \tag{7.6}$$

The strange and light sectors of hyperons will scale differently, and therefore we apply Eq. (7.6) to the individual quark sectors. Octet baryon properties are then reconstructed as described in the discussion surrounding Eq. (7.1) in Sec. 7.1. Results for baryon magnetic moments and their quark sector contributions are summarized in Tables A.13 through A.16.

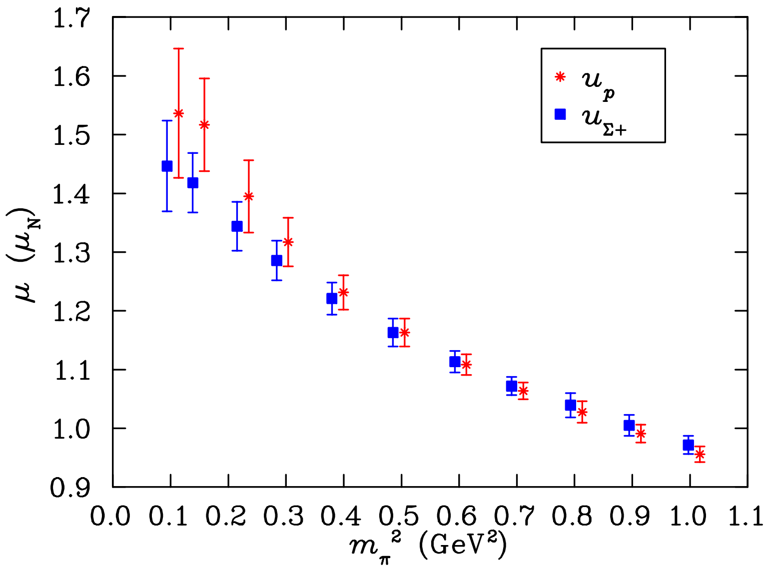

Figure 7.14: Magnetic moment contributions of u_p and u_{Σ^+} as a function of m_π^2. The contribution of u_p is plotted at shifted quark masses.

7.3.1 Quark Sector Magnetic Moments

The u-quark contribution to the proton and Σ^+ magnetic moments are illustrated in Fig. 7.14. The contribution u_p was described as the most optimal channel for directly observing chiral nonanalytic curvature in quenched lattice QCD simulations [45] and this curvature is evident in Fig. 7.14.

The value of χ for u_p is large and negative predicting LNA curvature towards positive values as the chiral limit is approached. The value of χ for u_{Σ^+} vanishes in the π channel. Similarly, strength in the ΞK channel is energetically suppressed. Hence the chiral curvature is predicted to be negligible for u_{Σ^+} and will contrast the upward curvature for u_p. This is observed in our lattice simulations. Figure 7.14 reveals curvature in u_p relative to a rather linear approach for u_{Σ^+} to the chiral limit.

The results for u_p and u_{Σ^+} are highly correlated and therefore the enhancement of the magnetic moment of u in the proton over the Σ^+ provides significant evidence of chiral nonanalytic behavior in accord with the LNA predictions of chiral perturbation theory. The strong correlation of these results is evident in the $SU(3)$ flavor-symmetric point at $m_\pi^2 \simeq 0.5$ GeV^2 where the results are identical. To expose the significance of this result, we present Fig. 7.15 illustrating the correlated ratio of magnetic moment contributions u_p/u_{Σ^+}. There, the significance exceeds two standard deviations for quark masses between the lightest quark mass considered and the $SU(3)$ flavor limit at $m_\pi^2 \simeq 0.5$ GeV^2.

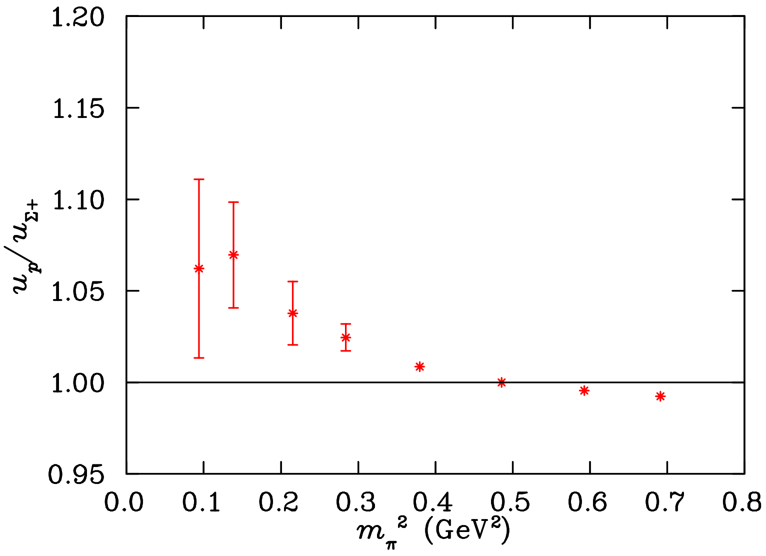

Figure 7.15: Ratio of u-quark contribution to the magnetic moments of the proton to that of u quark in Σ^+. Chiral curvature in the u-quark contribution to the proton's moment gives rise to significant enhancement in u_p.

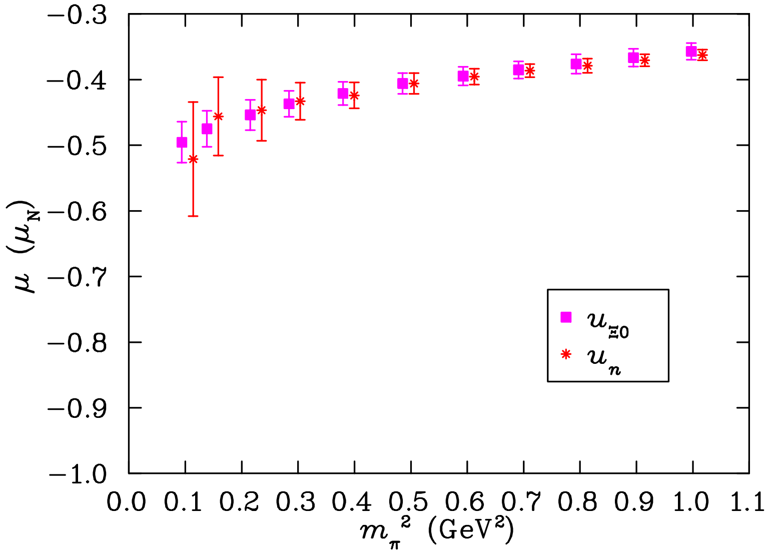

Figure 7.16: The u-quark contribution (single quark of unit charge) to the magnetic moments of the neutron, u_n, and Ξ^0, u_{Ξ^0}. The magnetic moment of u_n is shifted to the right for clarity.

Figure 7.16 illustrates the magnetic moment contribution of the single u quark in the neutron and the Ξ^0, normalized to unit charge. The magnetic moments match at the $SU(3)$-flavor limit where $m_\pi^2 \simeq 0.5$ GeV^2 as required. The environment sensitivity of the u quark contribution is subtle and is most evident in the size of the statistical error bar.

The chiral coefficient, χ, of the nonanalytic term $\sim m_\pi$ for u_n is large and greater than zero, predicting curvature towards negative values as the chiral limit is approached. While the coefficient for u_{Ξ^0} vanishes in the π channel, a substantial coefficient resides in the energetically favored ΣK channel and therefore some curvature towards negative values are again predicted as the chiral limit is approached. Fig. (7.16) is in accord with these predictions for the chiral curvature.

We note that for this case of magnetic moments, the anticipated chiral curvature is indeed observed for this sector. This contrasts the case of charge distribution radii, where chiral curvature was to oppose the Compton-broadening of the distribution and was not manifest in the simulation results.

It is interesting to examine the ratio of of singly (u_n) and doubly (u_p) represented quark contributions (for single quarks of unit charge) to nucleon magnetic moments [51]. The $SU(6)$ spin-flavor symmetry of the simple quark model provides

$$\mu_p = \frac{4}{3}\mu_u - \frac{1}{3}\mu_d \tag{7.7}$$

$$= \frac{2}{3}\,2\,\frac{2}{3}\mu_q^{\mathrm{QM}} - \frac{1}{3}\,1\left(-\frac{1}{3}\right)\mu_q^{\mathrm{QM}} \tag{7.8}$$

where μ_q^{QM} is the constituent quark moment. The quark moment pre-factors in Eq. (7.8) are respectively, $SU(6)$, quark number and charge factors. Discarding quark number and charge factors, one arrives at the $SU(6)$ prediction for u_n/u_p for single quarks of unit charge of $-1/2$. This prediction is to be compared with Fig. 7.17 which reveals this ratio is substantially smaller than the $SU(6)$ prediction, even at the $SU(3)$ flavor -symmetry limit where $m_\pi^2 \simeq 0.5$ GeV^2. This result is in accord with Ref. [51] where this effect was first observed in lattice QCD.

The gentle slope of the results in Fig. 7.17 at larger quark masses suggests that the $SU(6)$ spin-flavor symmetric quark model prediction of $-1/2$ will be realized only at much heavier quark masses than that examined here.

Figure 7.18 shows the magnetic moment contribution of the u-quark sector (or equivalently the d-quark sector) to the Λ^0 magnetic moment, normalized for a single

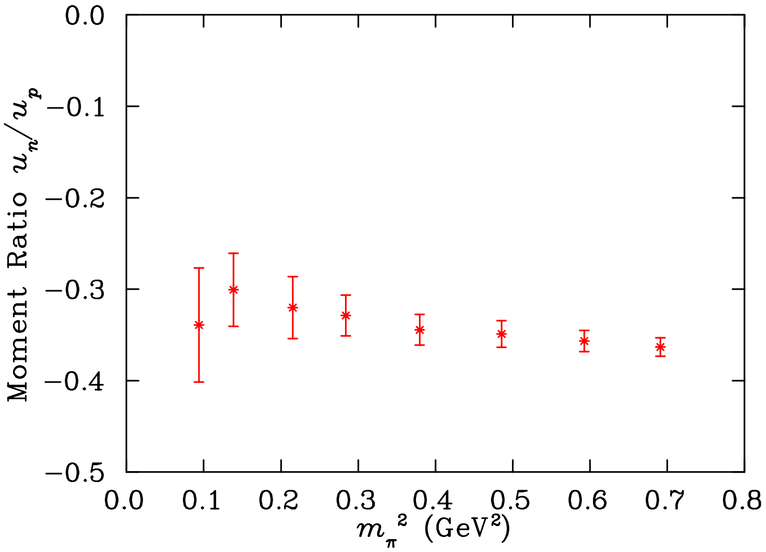

Figure 7.17: The ratio of singly (u_n) and doubly (u_p) represented quark contributions for single quarks of unit charge to nucleon magnetic moments. In the simple $SU(6)$ spin-flavor symmetric quark model the predicted ratio is constant at $-1/2$.

quark of unit charge. In simple quark models, this contribution is zero as the u and d quarks are in a spin-0, isospin-0 state. Our simulation results reveal that the dynamics of QCD, even in the quenched approximation, are much more complex. The contribution of u_Λ differs from zero by more than 8 standard deviations at the $SU(3)$ flavor -symmetric point and confirms earlier findings [51] of a non-trivial role for the light quark sector in the magnetic moment of Λ^0.

The chiral coefficient for u_Λ vanishes in the pion channel and has only small strength in the energetically favored NK channel. Hence little curvature is anticipated and this is supported by our findings in Fig. 7.18.

Turning our attention to the strange quark sectors, Figs. 7.19 and 7.20 present results for s_Λ, s_Ξ and s_Σ magnetic moments. In our simulations the strange quark mass is held fixed and therefore any variation observed in the results is purely environmental in origin. While s_Ξ and s_Σ display only a mild environment sensitivity, s_Λ shows significant dependence on its light quark environment.

Recall that in our examination of the environmental flavor -symmetry dependence of the strange quark distribution, a strong sensitivity is found. When the environmental quarks are in an isospin-0 state in the Λ, the strange quark distribution is broad. On the other hand, when the environmental quarks are in an isospin-1 state in Σ baryons, the

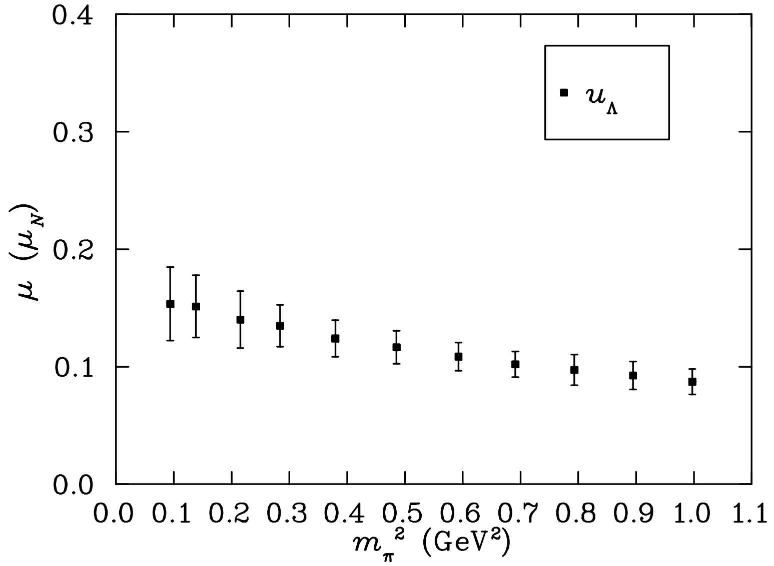

Figure 7.18: Magnetic moment contribution of the *u*-quark sector (or equivalently the *d*-quark sector) to the Λ^0 magnetic moment as a function of m_π^2.

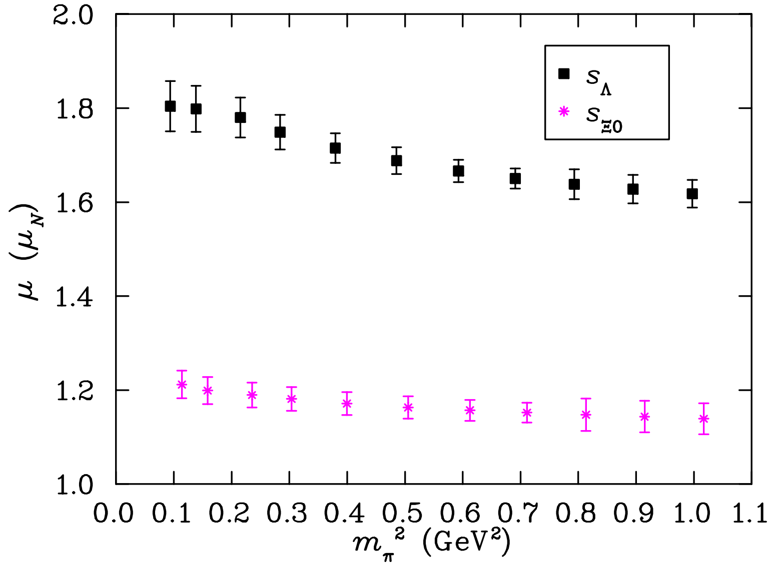

Figure 7.19: Magnetic moments of s_Λ and s_{Ξ^0} as a function of m_π^2. Results for s_{Ξ^0} are shifted to the right.

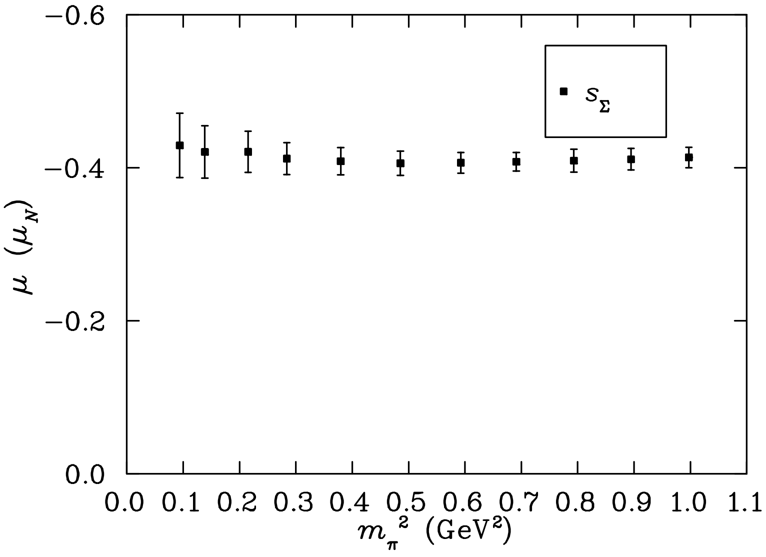

Figure 7.20: Magnetic moment contribution of s_Σ, as a function of m_π^2 as a function of m_π^2.

distribution radius is significantly smaller. It appears that the broad distribution of the strange quark in Λ makes it sensitive to the dynamics of its neighbors.

In the case of strange-quark moments, the LNA contributions are exclusively from transitions involving the kaon. Referring to Table A.38, one sees that both s_Λ and s_Ξ have strong transitions to the energetically favorable KN and $K\Sigma$ channels respectively. The coefficients are negative such that the virtual transitions will act to provide curvature towards positive values, enhancing the magnetic moments in these cases. This is not the case for s_Σ where the sign is positive and the transition is to the energetically unfavored $K\Xi$ channel. In summary, QχPT suggests the magnetic moments for s_Λ and s_Ξ will display curvature that acts to enhance the magnetic moment whereas s_Σ will display little curvature. These predictions are exactly as observed in Figs. 7.19 and 7.20.

7.3.2 Baryon Magnetic Moments

Figure 7.21 depicts the magnetic moments of Λ^0, Σ^- and Ξ^-. As the magnetic moments of Λ^0, and Ξ^- are dominated by the strange quark contribution, these moments show only a gentle dependence on the quark mass. These contrast Σ^- where the light d quarks dominate the moment.

The hyperon charge states, Σ^- and Ξ^- have LNA chiral coefficients which vanish in

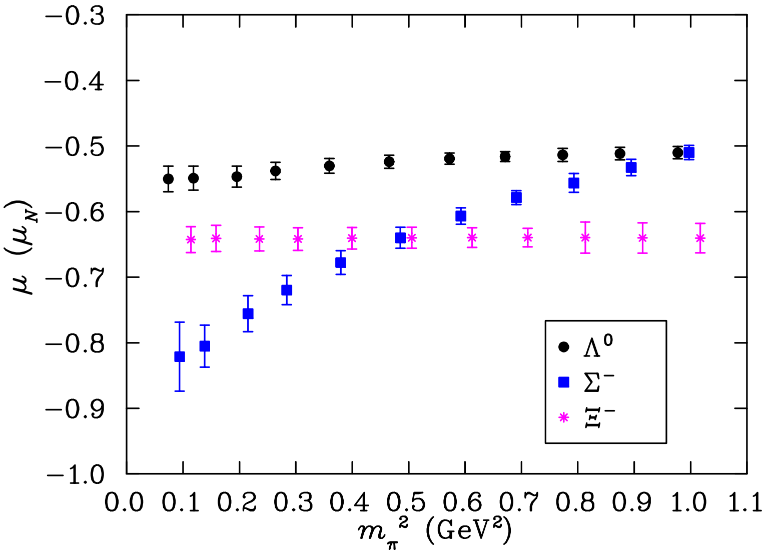

Figure 7.21: Magnetic moments of Σ^-, Λ^0 and Ξ^- as a function of m_π^2. Results for Λ^0 and Ξ^- are offset left and right respectively for clarity.

quenched QCD. On the other hand, the Λ^0 magnetic moment has some positive strength in the energetically favored NK channel, suggesting curvature towards negative values as the chiral limit is approached. These features are manifest in the Λ^0 and Ξ^- moments of Fig. 7.21 where the curvature in the Λ^0 moment towards negative values contrasts the invariance of the Ξ^- moment.

Figure 7.22 presents results for the Σ^0 baryon where chiral curvature is anticipated to be small. However, a comparison of p and Σ^+ magnetic moments provides a favorable opportunity to observe chiral curvature. The proton has a strong negative coupling to the pion channel, predicting curvature towards positive values as the chiral limit is approached. This contrasts the Σ^+ where the strong coupling is to the energetically unfavorable ΞK channel suggesting a more linear approach to the chiral limit.

Figure 7.23 depicts the variation of these moments with quark mass. These results are highly correlated and therefore the enhancement of the magnetic moment of the proton over the Σ^+ provides significant evidence of chiral nonanalytic behavior in accord with the LNA predictions of chiral perturbation theory. The strong correlation of these results is evident in the $SU(3)$ flavor-symmetric point at $m_\pi^2 \simeq 0.5$ GeV^2 where the results are identical.

Figure 7.24 reports the magnetic moments of the neutron and Ξ^0. The neutron provides a favorable case for the observation of chiral curvature associated with the pion

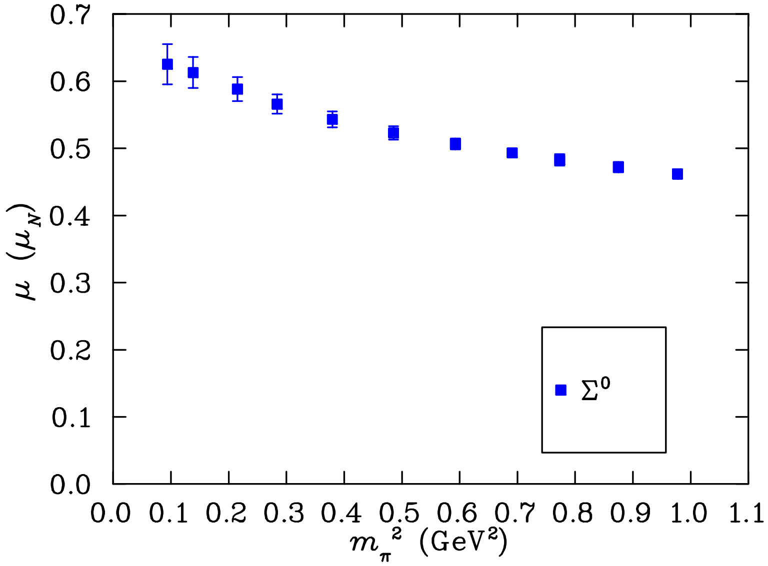

Figure 7.22: Magnetic moment of Σ^0 as a function of m_π^2.

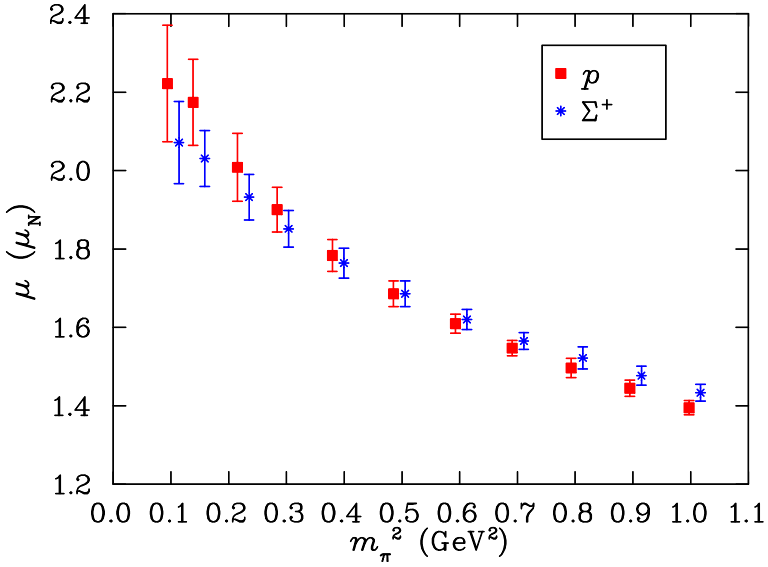

Figure 7.23: Magnetic moments of the proton and Σ^+ as a function of m_π^2. The Σ^+ moments are offset to the right for clarity.

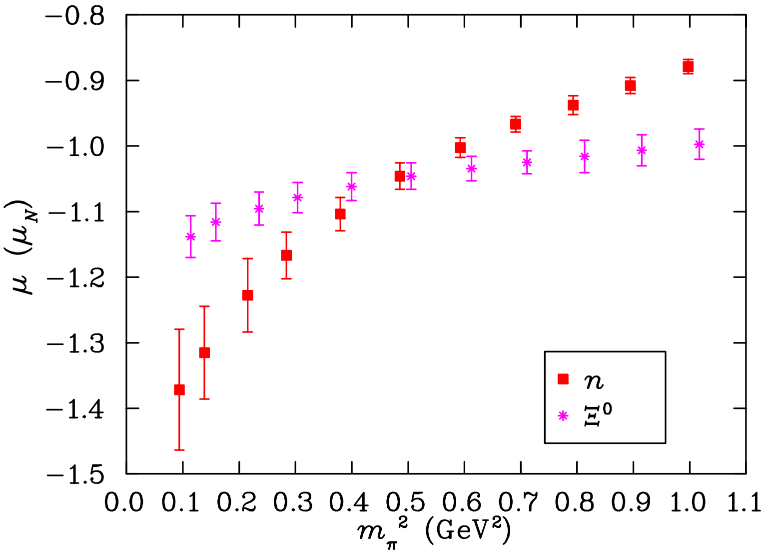

Figure 7.24: Magnetic moments of the neutron and Ξ^0 as a function of m_π^2. Ξ^0 moments are offset to the right for clarity.

channel. Similarly the Ξ^0 has significant strength in the energetically favored ΣK channel. In both cases the chiral coefficient, χ is positive, predicting curvature towards negative values as the chiral limit is approached. These predictions are in accord with the observations of Fig. 7.24.

In summary, we have performed an unprecedented exploration of the light quark-mass properties of octet-baryon magnetic moments in quenched QCD. Figure 7.25 presents our results in the context of recent state of the art results from lattice QCD [51, 83, 82]. The precision afforded by 400 $20^3 \times 40$ lattices and the efficient access to the chiral regime enabled by our use of the FLIC fermion action is clear. In every case, the LNA curvature predicted by chiral perturbation theory is manifest in our results.

7.3.3 Ratio of μ_{Ξ^-} to μ_Λ

The experimentally measured value of magnetic moment of Ξ^- is $-0.651 \pm 0.003\mu_N$ and that of Λ is $-0.613 \pm 0.004\mu_N$, making their ratio greater than 1 at 1.062 ± 0.012. This has presented a long-standing problem to constituent quark models which predict the magnetic moment ratio, Ξ^-/Λ^0 to be less than one.

In the simple $SU(6)$ spin-flavor quark model, the magnetic moment of Ξ^- is

$$\mu_{\Xi^-} = \frac{4}{3}\mu_s - \frac{1}{3}\mu_d \,, \tag{7.9}$$

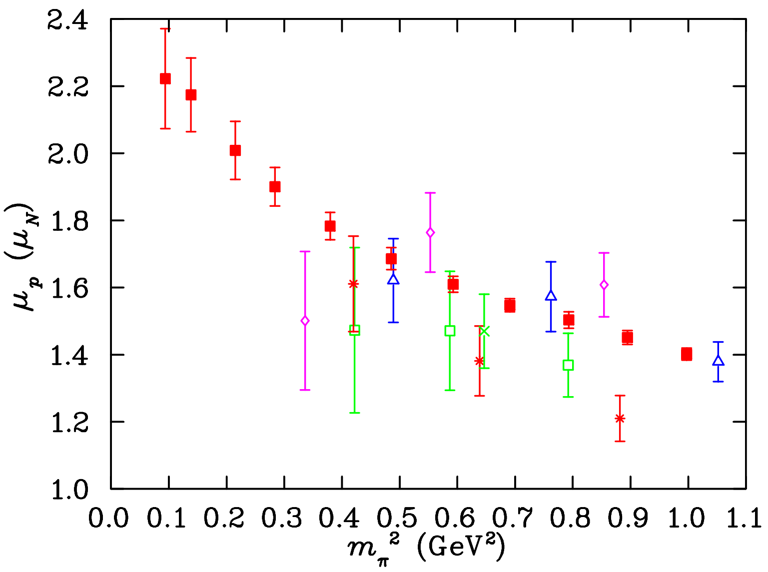

Figure 7.25: Proton magnetic moment in nuclear magnetons is compared to a variety of lattice simulations. The solid squares indicate our current lattice QCD results with FLIC fermions. The stars indicate the early lattice results of Ref. [51]. The crosses (only one point) indicate the results of Ref. [83]. The open symbols describe the QCD-SF collaboration results [82]. Open squares indicate results with $\beta = 6.0$, open triangles indicate those with $\beta = 6.2$ while the open diamonds indicate their results with $\beta = 6.4$.

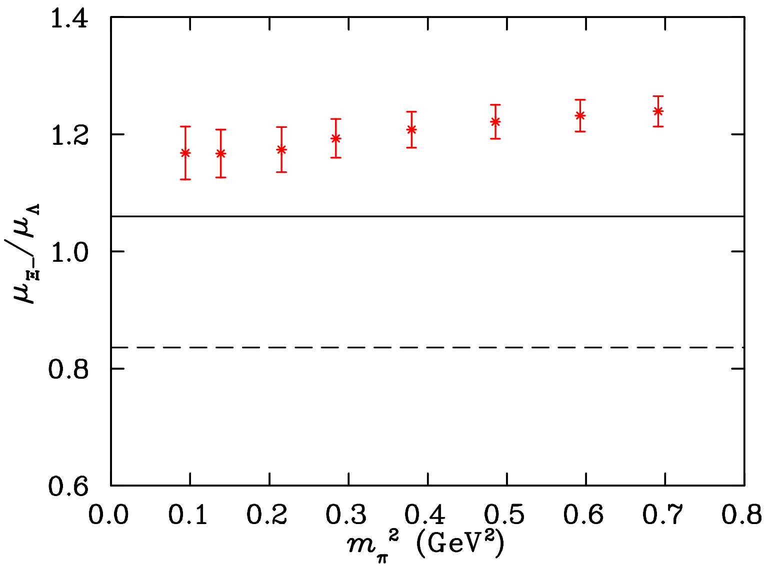

Figure 7.26: Ratio of the magnetic moment of μ_{Ξ^-} and μ_Λ as a function of quark mass. Experimental value of the ratio is indicated by the solid line. The dashed line is the value suggested by the SQM.

where μ_s and μ_d are the magnetic moments of the constituent s and d quarks respectively. Since the u-d pair in Λ forms a spin-0 state, the magnetic moment of the Λ has a sole contribution from the s quark

$$\mu_\Lambda = \mu_s\,. \tag{7.10}$$

Taking the ratio yields

$$\frac{\mu_{\Xi^-}}{\mu_\Lambda} = \frac{4}{3} - \frac{1}{3}\frac{\mu_d}{\mu_s}\,. \tag{7.11}$$

Now since, the magnetic moment of a charged Dirac particle goes inversely as its mass, and since the s and d quarks have identical charge, the ratio may be written

$$\frac{\mu_{\Xi^-}}{\mu_\Lambda} = \frac{4}{3} - \frac{1}{3}\frac{m_s}{m_d}\,, \tag{7.12}$$

where m_d and m_s are the constituent masses of the d and s quarks respectively. Given that $m_s > m_d$ it is inescapable that this ratio is less than 1 in the simple quark model. Indeed, the accepted values of d and s constituent quark masses place this ratio at 0.836.

Figure 7.26 shows the μ_{Ξ^-}/μ_Λ ratio as a function of quark mass as observed in our quenched lattice calculations. Remarkably, the ratio is greater than one at all quark masses.

There are two important aspects of our previous discussion that give rise to a result exceeding 1. First, as illustrated in Fig. 7.17, we have found that the singly represented quarks give a contribution to the magnetic moment that is much smaller in magnitude than that of the $SU(6)$ quark model prediction. This gives rise to a 40% reduction in the contribution of the second term of Eq. (7.12).

While this is sufficient to correct the ratio to ~ 1, there is a second effect. Namely, the light quark sector makes a nontrivial contribution to the Λ magnetic moment. As illustrated in Fig. 7.18, this contribution is positive for unit charge quarks. Since the net charge of the u-d sector is $+1/3$, the contribution of the s quark in Λ^0 must have a negative value whose magnitude exceeds the observed Λ moment. This is seen in Fig. 7.19. There, chiral curvature in s_Λ makes the ratio of magnetic moment contributions $s_\Lambda/s_\Xi \sim 3/2$ as opposed to the $SU(6)$ suggestion of 4/3. This resolves the long-standing discrepancy.

7.4 Magnetic Radii

Using the values for the magnetic moments obtained by scaling the individual quark sector contributions to $Q^2 = 0$, and our values for the form factors at finite Q^2, magnetic radii may be determined in exactly the same fashion as the electric radii.

Analogous to the charge radius, we adopt a dipole form for the Q^2 dependence and define the magnetic radius as

$$\frac{\langle r_M^2 \rangle}{\mathcal{G}_M(0)} = \frac{12}{Q^2}\left(\sqrt{\frac{\mathcal{G}_M(0)}{\mathcal{G}_M(Q^2)}} - 1 \right) . \tag{7.13}$$

The magnetic radii, $\langle r_M^2 \rangle / \mathcal{G}_M(0)$ of the octet baryons are tabulated in Tables A.17 and A.18.

Figure 7.27 depicts the magnetic radii of the proton and Σ^+ as a function of input quark mass. The somewhat subtle differences have a simple explanation in terms of the more localized strange quark in Σ.

In the proton, the long-range nature of the light-quark distributions means that their contributions to the magnetic form factor reduce quickly for increasing momentum transfers. In the case of Σ^+, which has a broadly distributed u quark distribution and a narrowly distributed s quark distribution, the reduction in magnitude of the form factor is less. Here, the s-quark distribution contributes positively and remains relatively invariant with increased resolution. Thus the Σ^+ has a larger form factor than the proton

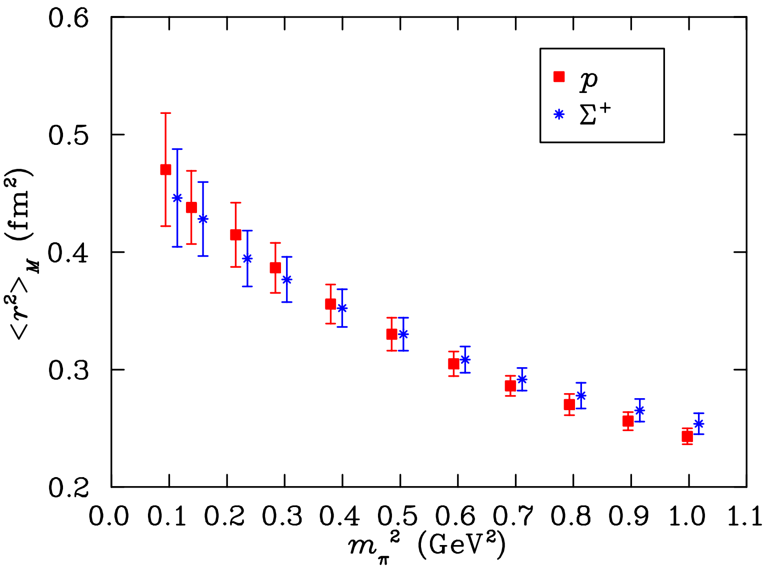

Figure 7.27: Magnetic radii of the proton and Σ^+ at different m_π^2 values. Σ^+ magnetic radius is plotted at shifted quark mass values.

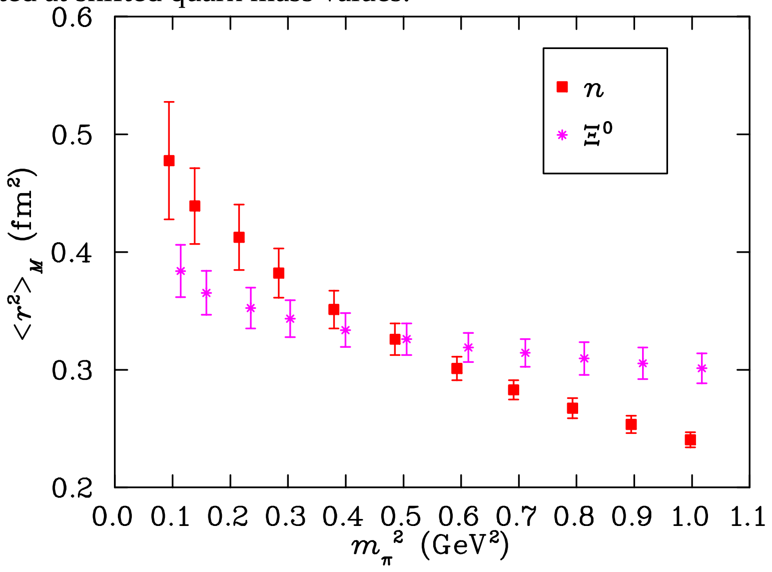

Figure 7.28: Magnetic radii of the neutron and Ξ^0 at different m_π^2. Ξ^0 magnetic radius is offset for clarity.

at finite Q^2 and hence a smaller magnetic radius.

Figure 7.28 reports the magnetic radii of the neutron and Ξ^0. Following a similar argument as above, the neutron is expected to have a larger magnetic radius than the Ξ^0, and this is confirmed in the plot.

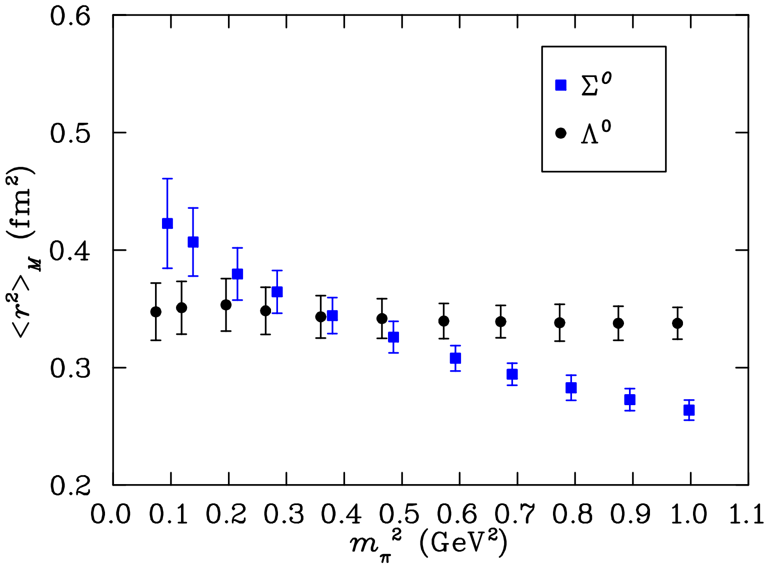

Figure 7.29: Magnetic radii of Σ^0 and Λ as a function of m_π^2. The Λ magnetic radius is plotted at shifted quark mass.

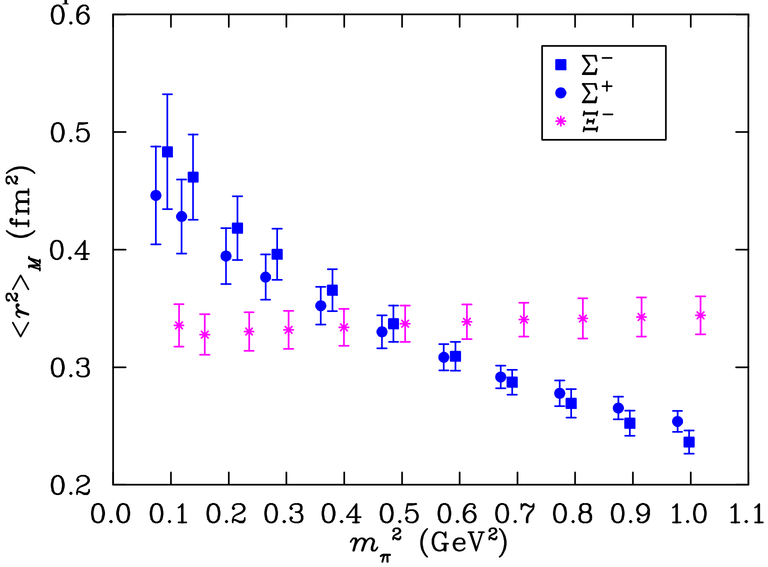

Figure 7.30: Magnetic radii of Σ^+,Σ^- and Ξ^- as a function of m_π^2. The data for Σ^+ and Ξ^- is plotted at shifted quark mass values.

Figure 7.29 illustrates the magnetic radii of Λ and Σ^0 as a function of the input quark mass. In Λ, most of the magnetic moment has its origin in the *s* quark and therefore the magnetic radius will be relatively small. In the Σ^0 the *u*-*d* sector is major contributor to the form factor. As a result, the form factor reduces more at finite momentum transfer, which in turn implies that the magnetic radius of the Σ^0 will be relatively large.

Figure 7.30 illustrates the magnetic radii of Σ^-, Σ^+ and Ξ^-. Σ^+ is replotted here to facilitate comparison with the other two members of the baryon octet.

Σ^- has the largest magnetic radius among the octet baryons and this is to be expected based on our considerations of the origin of the baryon magnetic moment. Here, the doubly represented d quark contributes to the total baryon form factor with the same sign, whereas the strange sector acts to reduce the magnitude of the total form factor. Upon increasing the momentum transfer resolution, the d-sector is reduced dramatically whereas the strange sector, acting to reduce the total form factor, is relatively preserved. this gives rise to a large drop in the total form factor at finite Q^2 and thus a large magnetic radius.

On the other hand, the singly represented d quark in the Ξ^- makes only a small contribution to the Ξ^- form factor, and therefore the magnetic radius reflects the small distribution of the strange quark.

7.5 Summary

The electromagnetic properties of octet baryons have been investigated extensively in a numerical simulation using the FLIC fermion action. This efficient fermion operator with excellent scaling properties [24] and vastly improved chiral properties [74] has enabled the first exploration of the electromagnetic form factors at light quark masses approaching the physical values. The unprecedented nature of our quark masses is illustrated in Figs. 7.13 and 7.25 for the proton charge radii and magnetic moments respectively.

Central to our discussion of the results is the search for evidence of chiral non-analytic behavior as predicted by chiral perturbation theory. We have discovered that all baryons having non-vanishing energetically-favorable couplings to virtual meson-baryon transitions tend to be broader than those which do not. This qualitative realization provides a simple explanation for the patterns revealed in our quenched-QCD simulations.

Of particular mention is the environmental isospin dependence of the strange quark distributions in Λ^0 and Σ^0. When the environmental quarks are in an isospin-0 state in the Λ, the strange quark distribution is broad. On the other hand, when the environmental quarks are in an isospin-1 state in Σ baryons, the distribution radius is significantly smaller.

Still, evidence of chiral *curvature* on our large-volume lattice is rather subtle in general and absent in the exceptional case of the singly-represented quark in the neutron or Ξ. In this case, the chiral loop effects act to oppose the Compton broadening of the distribution. However, it is thought that the restriction of momenta to discrete values on the finite-volume lattice prevents the build up of strength in the loop integral sufficient to counter the natural broadening of the distribution as the quark becomes light. It will be interesting to explore this quantitatively in finite-volume chiral effective field theory.

In contrast, chiral curvature is evident in the quark-sector contributions to baryon magnetic moments. In every case, the curvature predicted by chiral perturbation theory is manifest in our results. Of particular mention is the comparison of the u-quark contribution to the proton and Σ^+ illustrated in Figs. 7.14 and 7.15. The environment sensitivity of the s quark in Λ^0 depicted in Fig. 7.19 is particularly robust.

We find it remarkable that the leading nonanalytic features of chiral perturbation theory are observed in our simulation results. Naively, one might have expected a nontrivial role for the higher order terms of the chiral expansion which might have acted to hide the leading behavior. However, the smooth and slow variation of our simulation results indicate that these higher order terms must sum to provide only a small correction to the leading behavior. These observations indicate that regularizations of chiral effective field theory which resum the chiral expansion at each order, to ensure that higher order terms sum to only small corrections, will be effective in performing quantitative extrapolations to the physical point. Indeed work in this direction [47, 59, 61] has been very successful.

Comparison of our quenched QCD results with experiment is not as interesting. The chiral physics of quenched QCD differs from the correct chiral physics of full QCD and our results do not explore sufficiently light quark masses to reveal these discrepancies. The simulation results do not agree with experiment, particularly for light quark baryons where chiral physics makes significant contributions. However, methods have been discovered for quantitatively estimating the corrections to be encountered in simulating full QCD and we refer the interested reader to Refs. [47, 59, 61] for further discussion.

In future simulations it will be interesting to explore the utility of boundary conditions which allow access to arbitrarily small momentum transfers, providing opportunities to map out hadron form factors in detail. Similarly, by calculating near $Q^2 = 0$ one would have more direct access to the magnetic moment. Nevertheless, such boundary conditions cannot be seen to substitute for larger volume lattices, as the discretization of the momenta due to the finite volume of the lattice acts to suppress chiral nonanalytic behavior. Only with increasing lattice volumes will the continuous momentum of chiral loops be approximated well on the lattice.

Chapter 8

Results-Decuplet baryons

8.1 Form Factors

The baryon form factors are calculated on a quark-sector by quark-sector basis with each sector normalized to the contribution of a single quark with unit charge, as explained in Chapter 7. To calculate the corresponding baryon property, each quark sector contribution should be multiplied by the appropriate charge and quark number.

Under such a scheme for a generic form factor f, the Δ^+ form factor, f_{Δ^+}, is obtained from the u- and d-quark sectors normalized to a single quark of unit charge via

$$f_{\Delta^+} = 2 \times \frac{2}{3} \times f_u + 1 \times \left(-\frac{1}{3}\right) \times f_d \,. \tag{8.1}$$

Figure. 8.1 depicts the electric form factor $E0$ of the u quark in the Δ as a function of time at the $SU(3)$ flavor limit. The u and d quarks in the Δ states are identical, being identical spin states. The straight lines indicate the time-slices which were selected using the χ^2/dof considerations explained in Chapter 6.

For light quark masses lighter than the strange quark mass, we fit the change in the form factor ratios of Eq. (6.62) from one quark mass to the next and add this to the previous result at the heavier quark mass.

Figure 8.2 shows the fitting of the electric form factor splitting for the Δ^+ between the eighth and ninth quark masses, the latter having $m_\pi^2 = 0.2153$ GeV^2. The improvement of the plateau is apparent in Fig. 8.2. Still substantial Euclidean time evolution is required to obtain an acceptable χ^2/dof. The onset of noise at this lighter quark mass is particularly apparent at time slice 21.

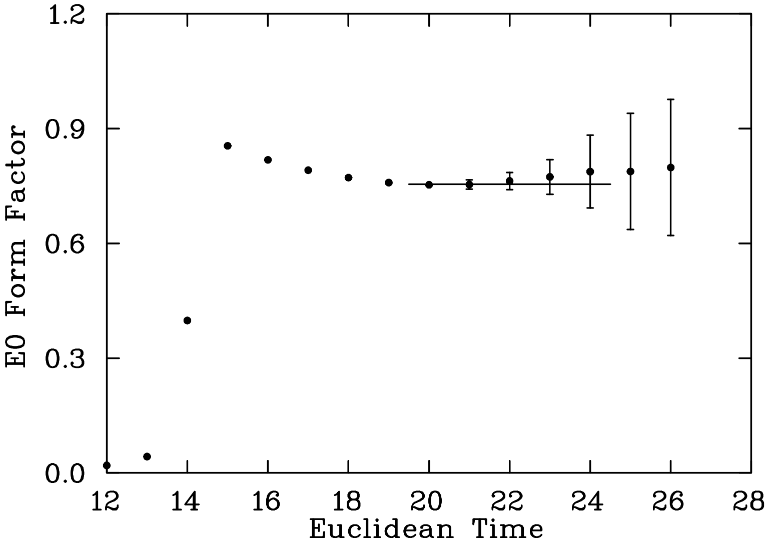

Figure 8.1: $E0$ electric form factor of the u quark in Δ at $Q^2 = 0.230(1)\mathrm{GeV}^2$ as a function of Euclidean time (t_2) for $m_\pi^2 = 0.4854(31)$ GeV^2, the $SU(3)$-flavor limit. The line indicates the fitting window and the best fit value.

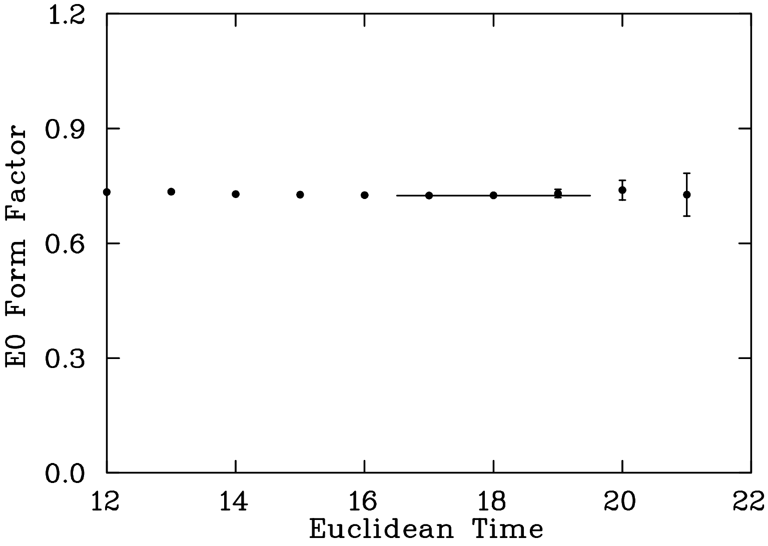

Figure 8.2: $E0$ electric form factor of the u quark in Δ at $Q^2 = 0.230(1)$ GeV^2 as a function of Euclidean time(t_2) at the ninth quark mass where $m_\pi^2 = 0.2153(35)$ GeV^2. The correlator is obtained from the splitting between the ninth and eighth quark mass results. The line indicates the fitting window and the best fit value.

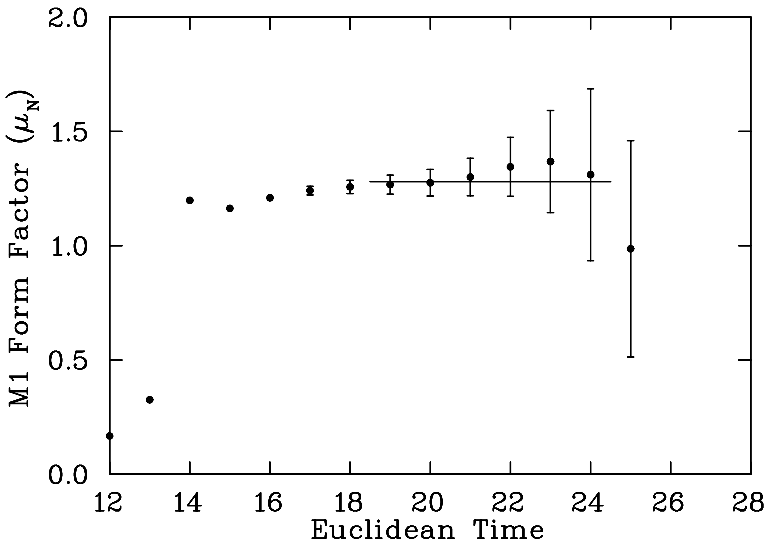

Figure 8.3: $M1$ magnetic form factor of the u or d quark in the Δ at $Q^2 = 0.230(1)$ GeV^2 as a function of Euclidean time (t_2) for $m_\pi^2 = 0.4854$ GeV^2, the $SU(3)$-flavor limit. The line indicates the fitting window and the best fit value.

Tables A.19 to A.21 list the $E0$ form factors for all the decuplet baryons at the quark level for the eleven quark masses considered. In the tables, the selected time frame, the fit value and the associated χ^2/dof are indicated.

The magnetic form factor $M1$ for the u quark sector in the Δ at the $SU(3)$ limit is plotted in Fig. 8.3 as a function of Euclidean time. Here the conversion from the natural magneton, $e/(2\,m_B)$ where the mass of the baryon under investigation appears, to the nuclear magneton, $e/(2\,m_N)$ where the physical nucleon mass appears, has been done by multiplying the lattice form factor results by the ratio m_N/m_B. In this way the form factors are presented in terms of a constant unit; *i.e.* the nuclear magneton.

In Fig. 8.4 we present the Euclidean time dependence of the the $M1$ magnetic form factors of Δ calculated at the ninth quark mass where $m_\pi^2 = 0.2153(35)$ GeV^2. The splittings analysis provides an early onset of acceptable plateau behavior. Results for the quark-sector contributions to the $M1$ magnetic form factors of decuplet baryons are summarized in Tables A.22 to A.24.

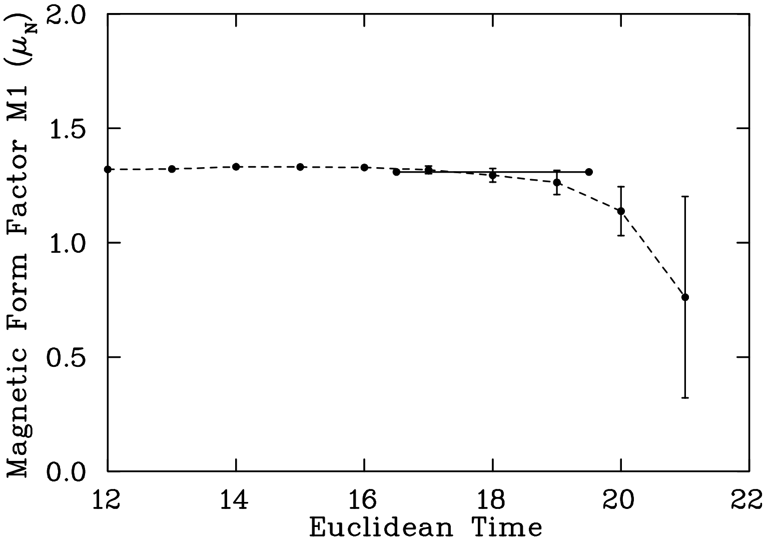

Figure 8.4: $M1$ form factor of the u quark in Δ at $Q^2 = 0.230(1)$ GeV^2 at the ninth quark mass where $m_\pi^2 = 0.2153(35)$ GeV^2. The correlator is obtained from the splitting between the ninth and eighth quark mass results. The line indicates the fitting window and the best fit value.

8.2 Charge Radii

We use the expression described in Chapter 7 which allows us to calculate the electric charge radius of a baryon using our two available values of the Sachs electric form factor ($\mathcal{G}_E(q^2_{\rm min})$, $\mathcal{G}_E(0)$), namely

$$\frac{\langle r_E^2 \rangle}{\mathcal{G}_E(0)} = \frac{12}{q^2}\left(\sqrt{\frac{\mathcal{G}_E(0)}{\mathcal{G}_E(q^2)}} - 1\right) . \tag{8.2}$$

However to calculate the charge radii of the neutral baryons, the above equation cannot be used, due to the fact that in those cases $\mathcal{G}_E(0) = 0$. As in the case of octet baryons, for the neutral baryons we first calculate the charge radii for each quark sector which are then combined using the appropriate charge and quark number factors as described in Sec. 7.1 to obtain the total baryon charge radii. We use the same procedure to calculate the charge radii of all the baryons. Tables A.25 to A.27 provide the electric charge radii of the decuplet baryons and the quark sector contributions. At the $SU(3)$ limit (sixth quark mass) the quark contribution is identical in all cases as expected. The quark contributions in the baryons are close to each other and do not show substantial environment sensitivity.

Figures 8.5 and 8.6 depict plots of the quark contributions to the decuplet charge radii. Figures 8.7 and 8.8 indicate charge radii of the quark sectors in the decuplet baryons and the octet baryons at the ninth quark mass. From the figures it is evident that the contribution of the quarks is very much baryon dependent in the octet case, while it is less sensitive to the environment in the decuplet case. The charge radius of the u quark distribution in the decuplet baryons is smaller than that in the octet baryons. The u quark charge radius in the octet baryons decreases with the inclusion of the s quark. The u quark charge radius in the nucleon, Σ and Ξ are in decreasing order due to the inclusion of additional s quarks. Such an influence of the s quark on u quark charge radius is absent in the decuplet behavior.

From Fig. 8.7 it is evident that the charge radius of the u quark in proton (u_p) is higher than that of the u quark in Δ^+ (u_{Δ^+}). To remove the overlapping errors in comparison we computed the ratios of charge distribution of similar quarks in the octet to that in the decuplet. The ratio $\langle r^2\rangle(u_p)/\langle r^2\rangle(u_{\Delta^+})$ is calculated at all configurations and averaged using jack-knife methods. Figures 8.9 and 8.10 depict the ratio of the quark contributions in the octet baryons to that in the decuplet baryons at the $SU(3)$-flavor limit and the ninth quark mass respectively. In the figures u_{p/Δ^+} denotes the ratio $\langle r^2\rangle(u_p)/\langle r^2\rangle(u_{\Delta^+})$. In both the cases, the u quark contribution to charge radius in the proton is higher than that in the Δ^+ at the $SU(3)$ limit. At the $SU(3)$ limit all the quarks have equal mass, equal to that of the strange quark and one would expect the quark model picture to dominate. This suggests that the u_Δ should have a broader distribution than the distribution of u_p. Our results contrast this prediction. The smaller charge radius of u_Δ compared to that of u_p also rules out any suggestion of a hyperfine attraction leading to $u-d$ diquark clustering in the nucleon or the hyperon states [65].

Figures 8.11, 8.12 and 8.13 are plots of the decuplet baryon charge radii as a function of quark mass. The charge radius of Δ^- is numerically equal to that of the Δ^+ with a negative sign. This makes the charge radius of Δ^0 identically equal to zero. The charge radius of Ω^- is taken as that of the Δ^- at the $SU(3)$ limit, and is numerically equal to $-0.31 \pm 0.01\text{fm}^2$.

The decuplet baryon form factors are dominated by the net charge of the light quarks. For the Δ^0 the symmetry of the u and d quarks makes the form factors vanish. In the neutron however the three quarks are in mixed symmetric states giving rise to a non-zero form factor and charge radius. Charge radii of the neutral Σ^* and Ξ^* too are close to zero and are dominated by the light quark sectors. The presence of the s quark as one moves from Δ to Σ^* and Ξ^* reduces the magnitude of the charge radius as indicated in the figures for the charged baryons.

Figure 8.14 depicts the ratio of charge radii of the octet to decuplet baryons. Here

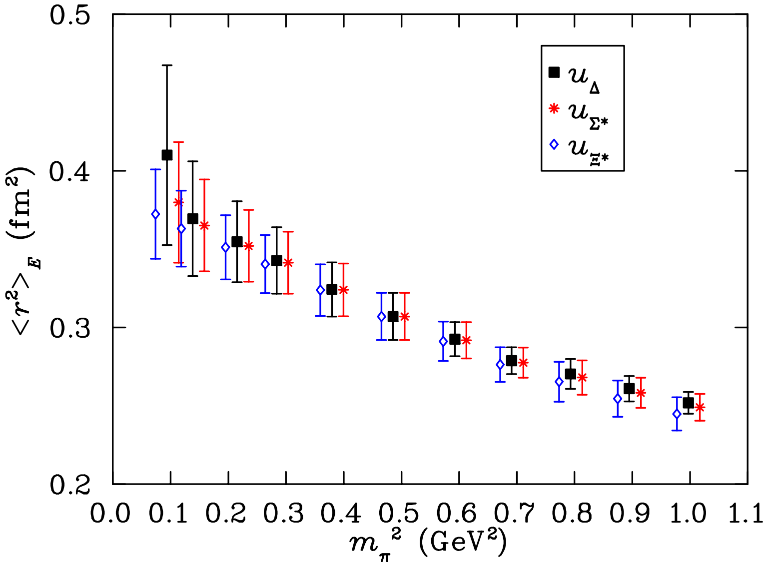

Figure 8.5: Charge radii of u_Δ, u_{Σ^*} and u_{Ξ^*} as a function of m_π^2. The values for Δ are plotted at m_π^2 while that of the u_{Σ^*} and u_{Ξ^*} are plotted at shifted m_π^2 for clarity.

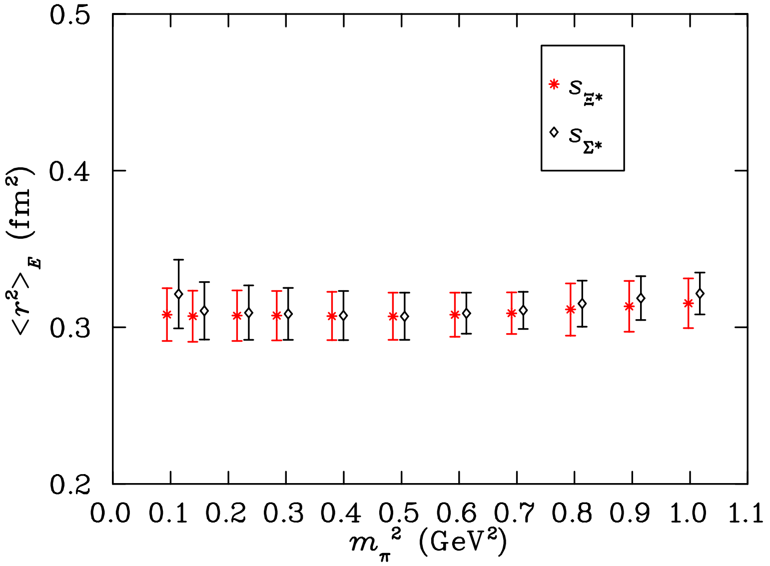

Figure 8.6: Charge radii of s_{Σ^*} and s_{Ξ^*} as a function of m_π^2. The values for s_{Σ^*} are plotted for shifted m_π^2 values for clarity.

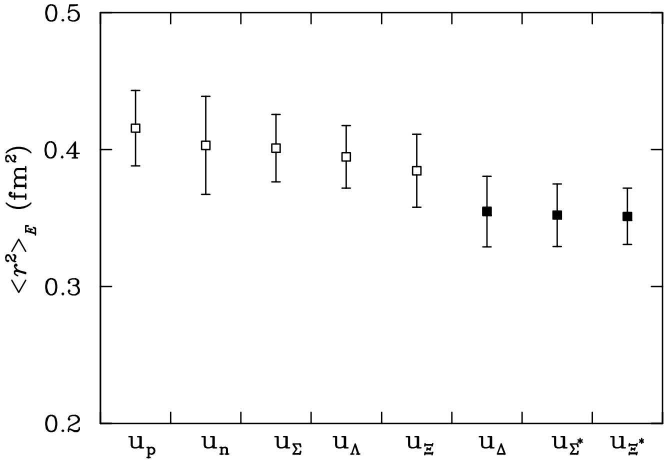

Figure 8.7: Charge radii of *u* quark in the octet and decuplet baryons at the ninth quark mass where $m_\pi^2 = 0.2153(35)$ GeV^2.

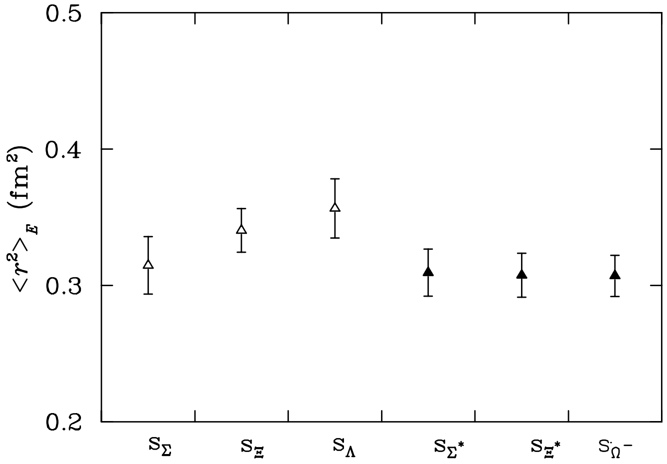

Figure 8.8: Charge radii of *s* quark in the octet and the decuplet baryons at the ninth quark mass where $m_\pi^2 = 0.2153(35)$ GeV^2.

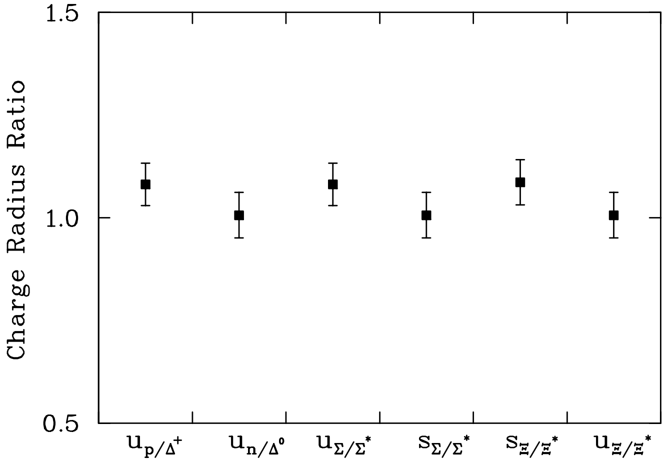

Figure 8.9: Ratio of charge radii of the quark sector contributions in the octet/decuplet baryons at the *SU*(3)-flavor limit where $m_\pi^2 = 0.4854(31)$ GeV^2. The *SU*(3)-flavor symmetry is manifest in the results.

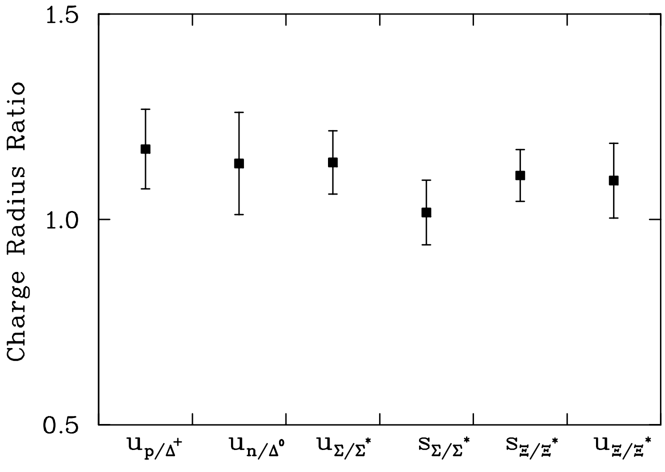

Figure 8.10: Ratio of charge radii of the quark sector contributions in the octet/decuplet baryons at the ninth quark mass where $m_\pi^2 = 0.2153(35)$ GeV^2.

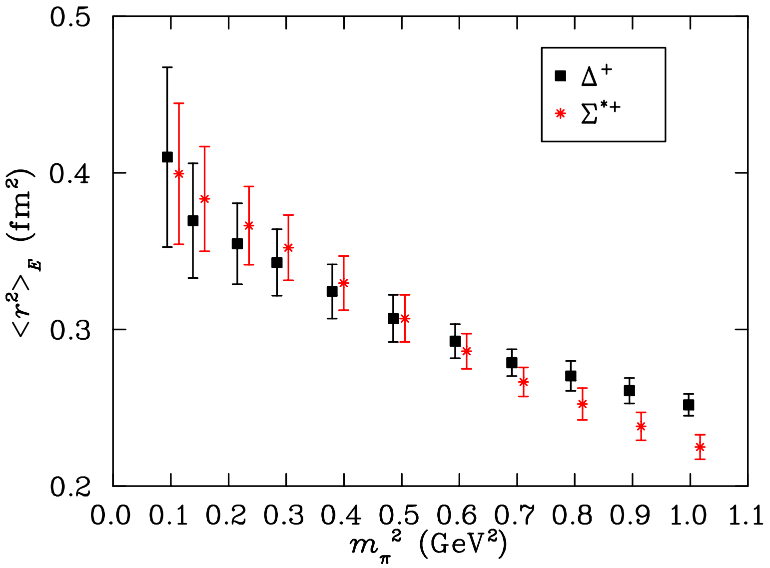

Figure 8.11: Charge radii of Δ^+ and Σ^{*+} as a function of m_π^2. The values for Σ^* are plotted at shifted m_π^2 for clarity.

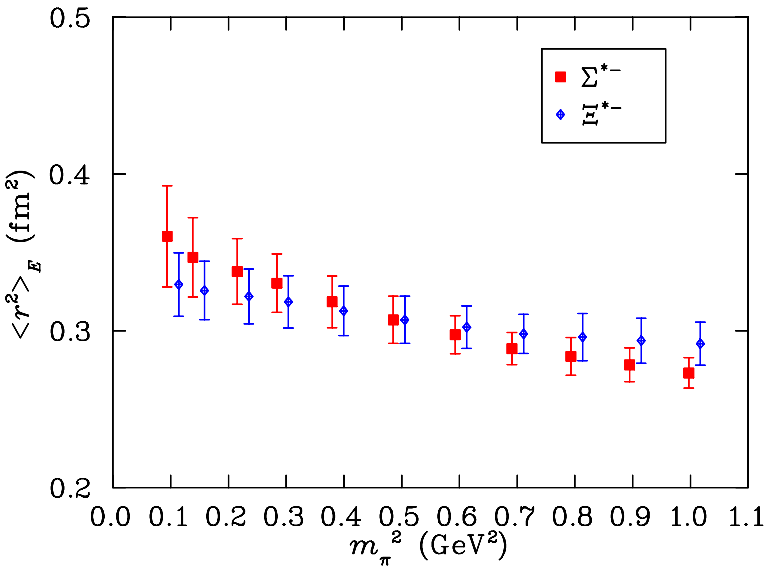

Figure 8.12: Charge radii(magnitude) of Σ^{*-} and Ξ^{*-} as a function of m_π^2. The values for Ξ^{*-} are plotted at shifted m_π^2 for clarity.

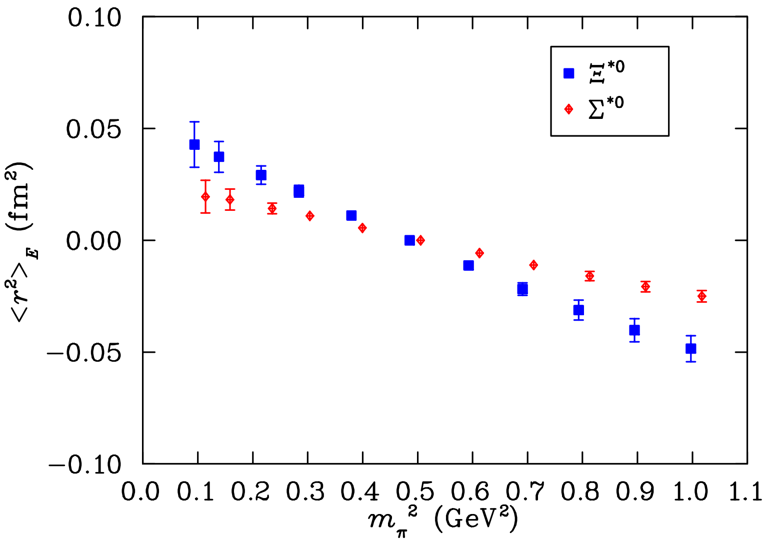

Figure 8.13: Charge radii of Σ^{*0} and Ξ^{*0} as a function of m_π^2. The values for Σ^{*0} are plotted at shifted m_π^2 for clarity.

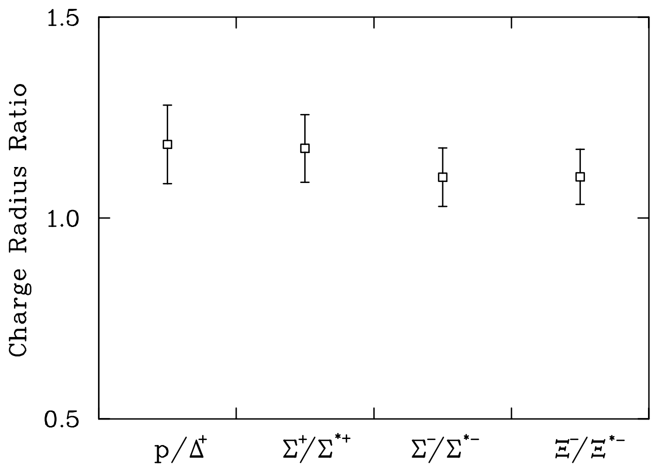

Figure 8.14: Ratio of charge radii of the octet baryons to decuplet baryons at the ninth quark mass where $m_\pi^2 = 0.2153(35)$ GeV^2.

too the octet baryons display a slightly larger charge radius than their decuplet counterparts. The charge radii of the decuplet baryons with the quark sector contribution are listed in tables A.25-A.27.

8.3 Magnetic Moments

The magnetic moment is defined as the value of the magnetic form factor at zero momentum transfer, $q^2 = 0$,

$$\mu = \frac{e}{2M_B}\mathcal{G}_M(0)\,, \tag{8.3}$$

where M_B is the mass of the baryon. We calculate magnetic form factors at the smallest finite value of q^2 available on our lattice, hence we must scale our results from $\mathcal{G}_M(q^2)$ to $\mathcal{G}_M(0)$. We assume a scaling of electric and magnetic form factors in q^2. In hyperons, the strange and light quarks are scaled separately by

$$\frac{\mathcal{G}_M(Q^2)}{\mathcal{G}_M(0)} \simeq \frac{\mathcal{G}_E(Q^2)}{\mathcal{G}_E(0)}\,. \tag{8.4}$$

We use the above relation to scale the individual quark-sector contributions and then reconstruct the baryon magnetic moments as

$$\mathcal{G}^B_M(0) = \mathcal{G}^l_M(0) + \mathcal{G}^s_M(0), \tag{8.5}$$

where l labels the light quarks and s labels the strange quark. Similar calculations are performed for the u and d sectors of the Δ.

Figures 8.15, 8.16 and 8.17 depict magnetic moments of the quark sectors in the decuplet baryons. The contributions of all the quarks are equal at the sixth quark mass indicating $SU(3)$ symmetry. The quark contributions in the Σ^* and Ξ^* are very similar to each other and there is not much evidence of any environment sensitivity. It is interesting to note the turn around in the magnetic moment contribution of the u quark in Δ at low quark mass.

To compare the decuplet moments with our octet moments, we plot the effective moments of the octet and the decuplet in Figs. 8.18 and 8.19.

Effective moments have been defined by equating the lattice quark sector contributions to the same sector of the $SU(6)$-magnetic moment formula derived from $SU(6)$-spin-flavor symmetry wave functions.

The simple quark model formula from $SU(6)$-spin-flavor symmetry gives the magnetic moment of the proton as

$$\mu_p = \frac{4}{3}\mu_u - \frac{1}{3}\mu_d\,, \tag{8.6}$$

where μ_u and μ_d are the magnetic moments per single quark of the doubly represented u quarks and singly represented d quarks. This can be generalized for any baryon with two doubly represented quarks D and one singly represented quark S.

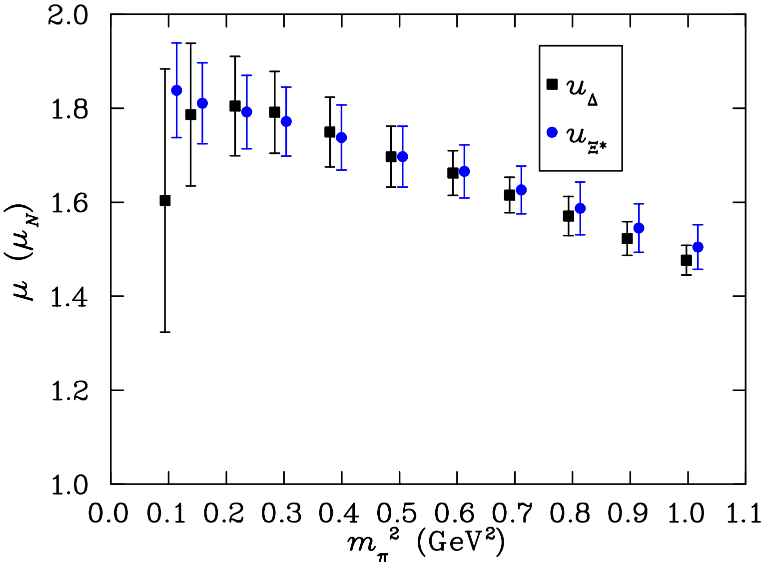

Figure 8.15: Magnetic moments of the u_Δ and u_{Ξ^*} as a function of m_π^2. The values for u_{Ξ^*} are plotted at shifted m_π^2 for clarity.

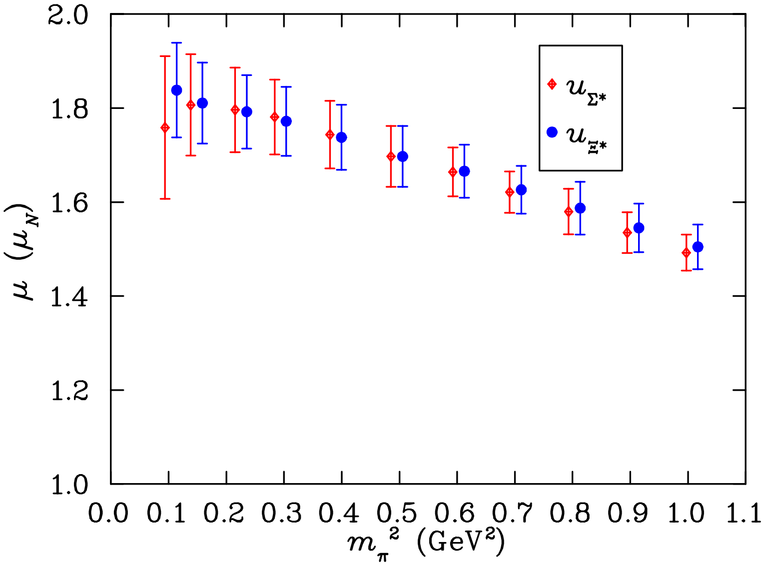

Figure 8.16: Magnetic moments of the u_{Σ^*} and u_{Ξ^*} as a function of m_π^2. The values for u_{Ξ^*} are plotted at shifted m_π^2 for clarity.

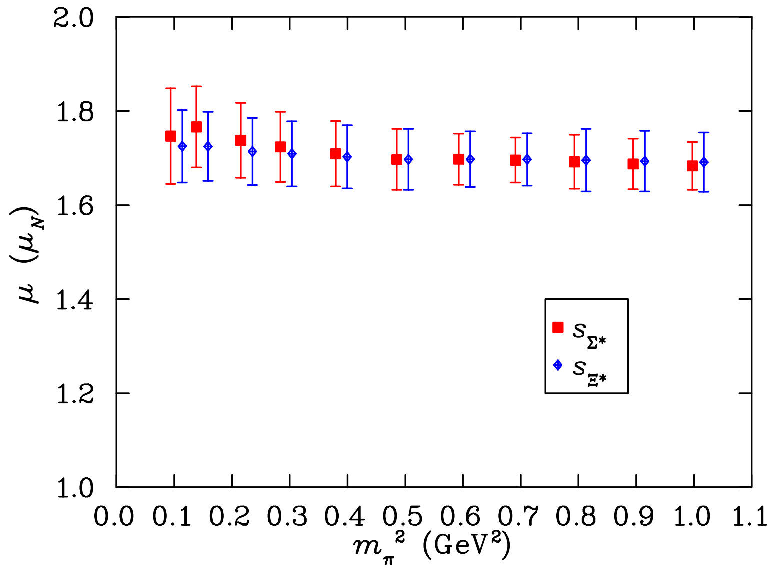

Figure 8.17: Magnetic moments of the s_{Σ^*} and s_{Ξ^*} as a function of m_π^2. The values for s_{Ξ^*} are plotted at shifted m_π^2 for clarity.

Focusing on the proton and using the charge factors of the doubly represented and singly represented quarks as 2/3 and (-1/3) respectively, the above equation is modified to

$$\mu_p = \left(\frac{4}{3}\right)\left(\frac{2}{3}\right)\mu_D^{\text{Eff}} - \left(\frac{1}{3}\right)\left(-\frac{1}{3}\right)\mu_S^{\text{Eff}} , \tag{8.7}$$

where μ_D^{Eff} and μ_S^{Eff} are the magnetic moments of a single quark of unit charge, for the doubly and singly represented quarks respectively. The factors 2/3 and -1/3 account for the charge factors separately.

On the lattice we calculate the baryon magnetic moments from the quark sectors using

$$\mu_p = 2\left(\frac{2}{3}\right)\mu_D^{\text{Latt}} + 1\left(-\frac{1}{3}\right)\mu_S^{\text{Latt}} . \tag{8.8}$$

In the above equation the factors 2 and 1 in the first and second term account for the doubly and singly represented quarks, for single quarks of unit charge. Equating quark sectors in Eqs. (8.7) and (8.8) yields for the effective moments respectively,

$$\begin{aligned} \mu_S^{\text{Eff}} &= -3\mu_S^{\text{Latt}} , \\ \mu_D^{\text{Eff}} &= \frac{3}{2}\mu_S^{\text{Latt}} , \end{aligned} \tag{8.9}$$

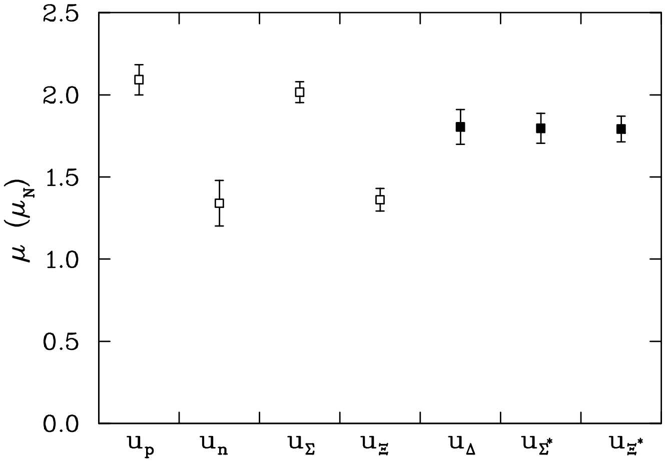

Figure 8.18: Effective moments of the *u* quark sector in the octet and the decuplet baryons at the ninth quark mass where $m_\pi^2 = 0.2153(35)$ GeV^2 .

in the spirit of a constituent quark moment, $e\hbar/2m_q^{\rm Eff}$.

For the decuplet baryons the magnetic moment is the sum of the individual quark contributions. Hence Eq. (8.7) for the Δ baryons becomes

$$\mu_{\Delta^+} = 2\left(\frac{2}{3}\right)\mu_D^{\rm Eff} + 1\left(-\frac{1}{3}\right)\mu_S^{\rm Eff} \, . \tag{8.10}$$

On the lattice this is exactly the equation we use to build the decuplet baryon moments from the quark sector contributions. Therefore the quark level magnetic moments that we calculate are the effective moments of the quarks for both the doubly and singly represented quarks, *i.e.*,

$$\mu^{\rm Eff} = \mu^{\rm Latt} \, . \tag{8.11}$$

From the figures of the effective moments, it is evident that the quarks in the octet baryons show far more environmental sensitivity than their counterparts in the decuplet baryons.

The baryon magnetic moments are plotted in Fig. 8.20, Fig. 8.21 and Fig.8.22. For the magnetic moment of Ω^- we take the value of μ_{Δ^-} at the $SU(3)$ limit viz.,$-1.70 \pm 0.06\ \mu_N$. This is smaller than the value given by the Particle Data Group ($-2.02 \pm 0.05\ \mu_N$). The mass of the Ω^- from the lattice calculation (1.73 ± 0.012 GeV) over estimates the experimental value (1.67 GeV). The higher calculated mass may yield a lower magnetic moment in magnitude. This could be one of the reasons for a lower magnitude of the magnetic moment.

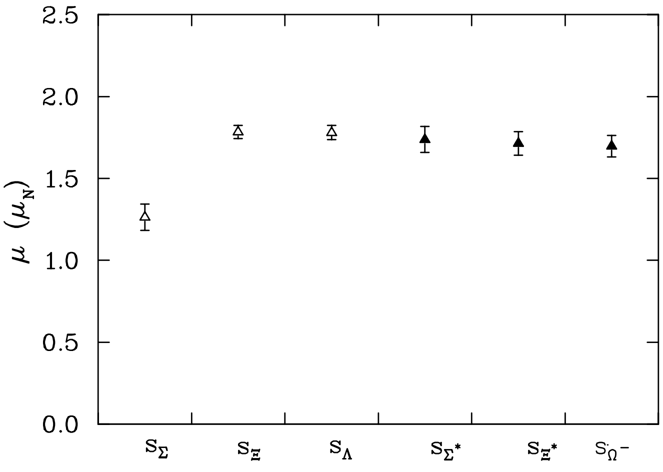

Figure 8.19: Effective moments of the s quark sector in the octet and the decuplet baryons at the ninth quark mass where $m_\pi^2 = 0.2153(35)$ GeV^2.

The other reason for this discrepancy probably lies in the absence of K-Ξ loops in the virtual transition of Ω^-. The virtual transition $\Omega \to \Xi K$ requires the presence of a light sea-quark flavor, whereas in QQCD, only the heavy strange flavor is present in the quenched Ω. In reality this would have significant contribution, since Ξ is a lower mass state than Ω^-. Such absence of important loops in QQCD represents missing physics in QQCD and causes the discrepancy from the values of Full QCD.

Figure 8.23 compares the magnetic moment of the Δ^+ with that calculated for the proton on the lattice. The simple quark model predicts that the proton and the Δ^+ have equal magnetic moments. However the interplay between the different pion-loop contributions to the Δ^+ magnetic moments indicate that the proton magnetic moment will be greater than that of the Δ^+ in Full QCD [49]. The Δ^+ magnetic moment shows a turn over as the quark mass becomes lighter.

In fact, all the decuplet baryons show to some extent, a turn over in the low quark mass region, in our quenched simulations. The magnitude of the turn over is dampened by the presence of s quark. Σ^* has a smaller turn over than Δ. The Ξ baryons with two s quarks show hardly any turn over.

As the light quarks get replaced by the heavier s quarks, some pion loops are replaced by kaon loops which are suppressed. These important contributions are suppressed in QQCD causing such a turnover of the decuplet baryon magnetic moments in the light quark mass region. Magnetic moments of the decuplet baryons are listed in Tables A.28 to A.30.

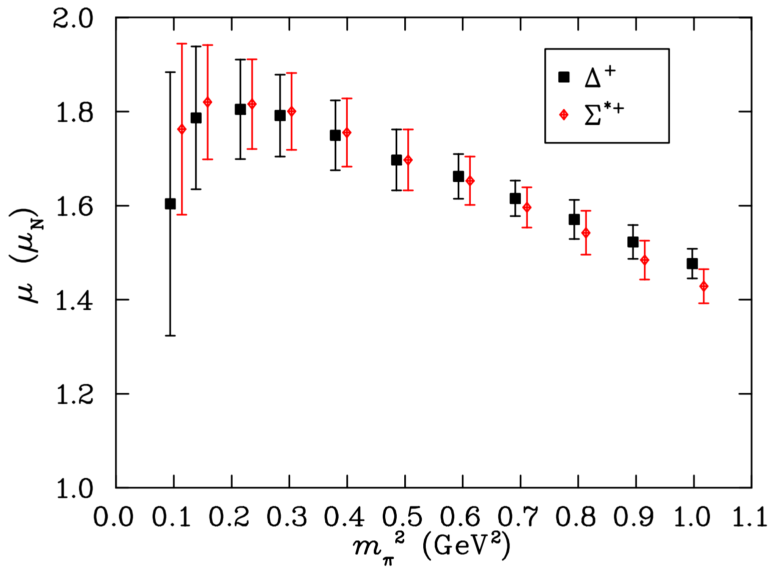

Figure 8.20: Magnetic moments of Δ^+ and Σ^{*+} as a function of m_π^2. The values for Σ^{*+} are plotted at shifted m_π^2 for clarity.

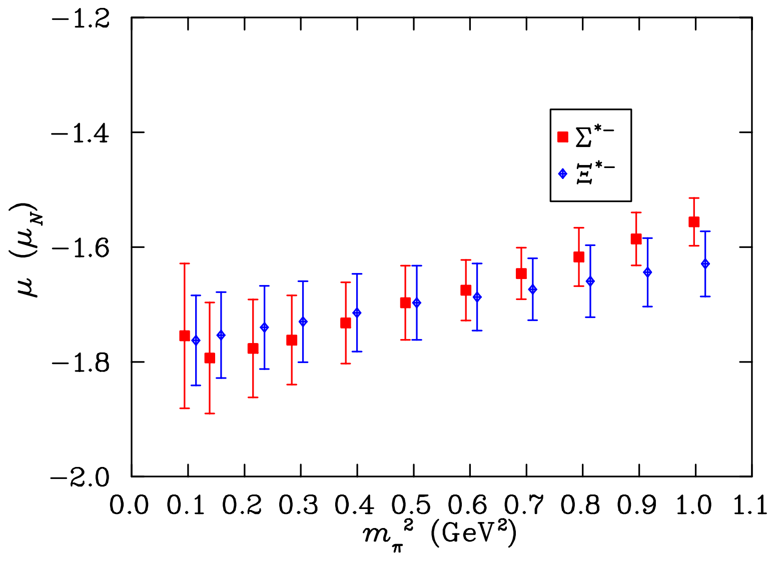

Figure 8.21: Magnetic moments of Σ^{*-} and Ξ^{*-} as a function of m_π^2. The values for Ξ^{*-} are plotted at shifted m_π^2 for clarity.

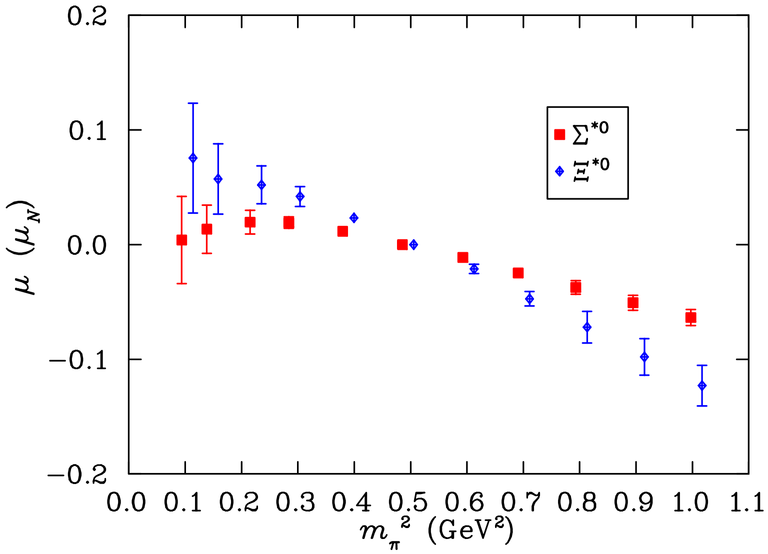

Figure 8.22: Magnetic moments of Σ^{*0} and Ξ^{*0} as a function of m_π^2. The values for Ξ^{*0} are plotted at shifted m_π^2 for clarity.

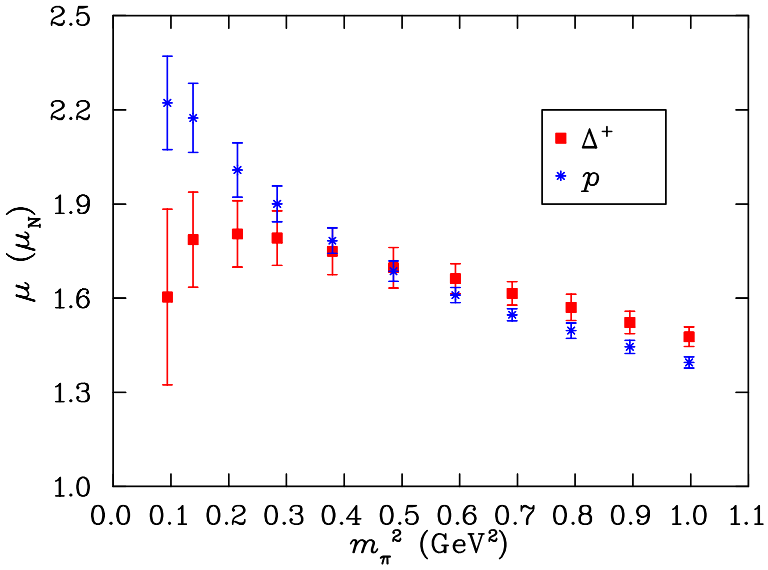

Figure 8.23: Magnetic moments of Δ^+ and the proton as a function of m_π^2.

8.4 Electric Quadrupole Form Factors

The $E2$ form factors of the spin-3/2 decuplet baryons give interesting information about the spherical symmetry of the charge distribution and hence is the subject of theoretical scrutiny. Figure 8.24 depicts the quadrupole form factor $E2$ of the u quark in Δ at the $SU(3)$-flavor limit, in units of e/M_N^2, as a function of time. Figure 8.25 indicates the quadrupole form factor of the u quark in Δ at the ninth quark mass. Here too the employment of splittings technique facilitates an earlier plateau. As mentioned in Sections 6.4.2 and 6.5.3, we considered the symmetry of the last two terms in Eq. (6.70) as the deciding factor in selecting the upper limit of the fit-window.

The quark sector contributions to the form factors in units of e/M_N^2 of all the decuplet members are indicated in Tables A.31 to A.33. For an axially deformed object the quadrupole form factor is related to the charge distribution through [63]

$$\mathcal{G}_{E2}(0) = M_B^2 \int d^3r \overline{\psi}(r)(3z^2 - r^2)\psi(r)\,, \tag{8.12}$$

where $3z^2 - r^2$ is the standard operator used for quadrupole moments. A positive quadrupole moment for a positively charged baryon indicates a prolate charge distribution, while a negative quadrupole moment indicates an oblate charge distribution. In non-relativistic models $E2$ form factor vanishes unless some configuration mixing is included in the baryon ground state.

The $E2$ form factors of the charged decuplet baryons in units of fm^2 for different values of m_π^2 are listed in table A.34. The $E2$ form factor of the Δ^0 is identically equal to 0 and other neutral baryons is close to zero. The value for the charged decuplet baryons is non-zero indicating a deformed shape.

From our simulation we conclude that the $E2$ form factor of the Ω^- baryon (the value of the Δ^- form factor at $SU(3)$ flavor limit) in units of 10^{-2} fm^2 is 0.85 ± 0.12. The small error limits show that the value is definitely on the positive side. Ω^- is a negatively charged baryon and hence this implies an oblate shape, with the equatorial axis being larger than the polar axis.

Similarly the $E2$ form factor for the Δ^+ is -0.85 ± 0.12 in units of 10^{-2} fm^2. Again, it is worth noting the small error bar, making the lattice calculation a very precise one. The negative $E2$ moment of a positive Δ^+ baryon implies an oblate shape.

The $E2$ form factor of Δ^{++} is twice that of the Δ^+ $E2$ form factor and hence it is equal to -1.17 ± 0.23, indicating an oblate shape.

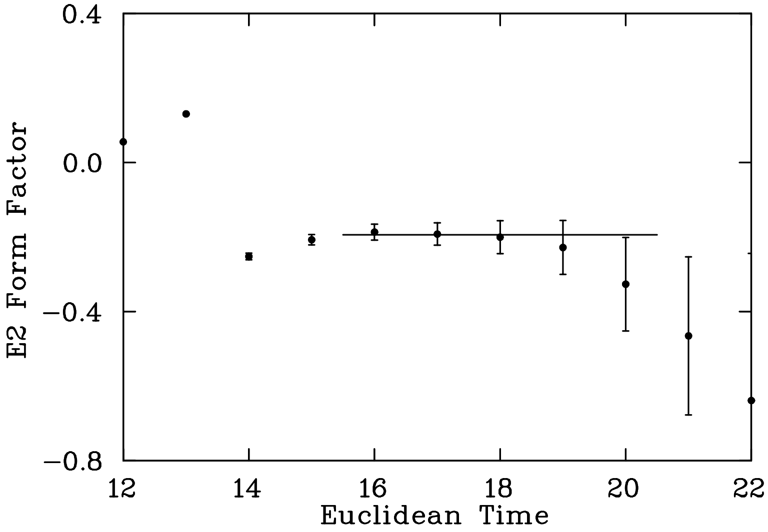

Figure 8.24: $E2$ electric form factor of the u or d quark sector in Δ at the $SU(3)$ flavor limit as a function of Euclidean time.

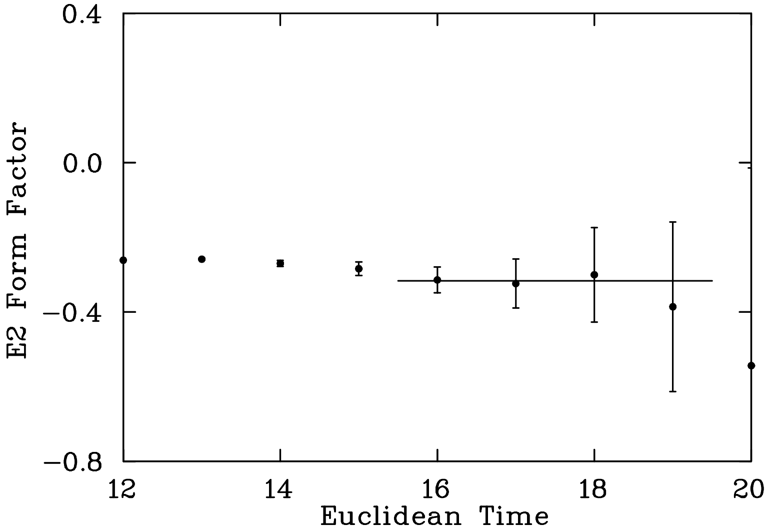

Figure 8.25: $E2$ electric form factor (splitting) of the quark sector in Δ as a function of Euclidean time at the ninth quark mass where $m_\pi^2 = 0.2153(35)\mathrm{GeV}^2$.

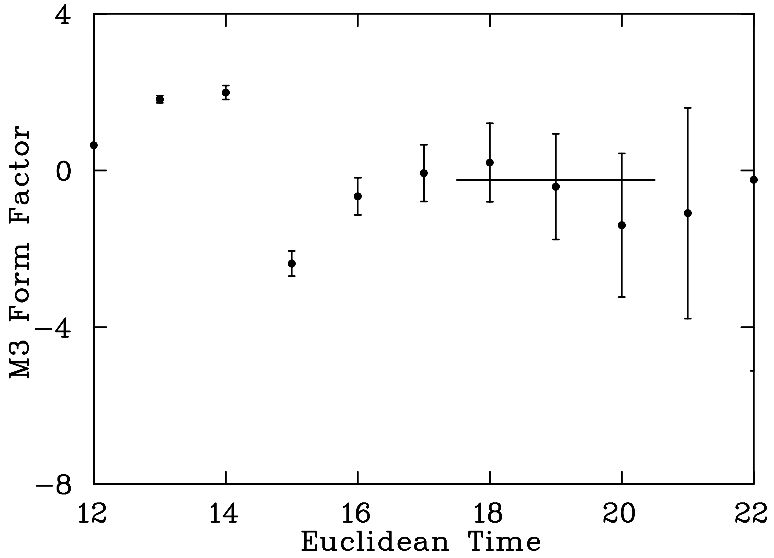

Figure 8.26: $M3$ Magnetic form factor of the u or d quark in Δ at the $SU(3)$ flavor limit as a function of time.

8.5 Magnetic Octupole Moments

The magnetic octupole form factors ($M3$) are consistent with zero. Like $E2$, the $M3$ transitions require nonzero orbital angular momentum admixtures in the ground state wave function [63]. Our statistics are not sufficient to reveal such admixtures.

Figure 8.26 is a plot of the $M3$ form factor of quark sector in the Δ as function of time at the sixth quark mass. Figure 8.27 is the $M3$ form factor at the ninth quark mass, where a reasonable plateau is realized due to the splittings method. Tables (A.35) to (A.37) list the quark sector $M3$ form factors.

8.6 Summary

We have performed an extensive calculation of the electromagnetic properties of the decuplet baryons at the quark level and the baryon level, including the quadrupole and octupole form factors of the spin-3/2 baryons. The splittings technique makes the extraction of form factors more reliable, with lower uncertainties. We find that the quarks in the decuplet are not as sensitive to the environment as their octet counterparts are. We have discovered that the decuplet baryon radii are smaller than that of the octet baryons, contradicting the simple quark model. The suppression of loop contributions in QQCD reduces the decuplet magnetic moment considerably. With the help of the E2 form

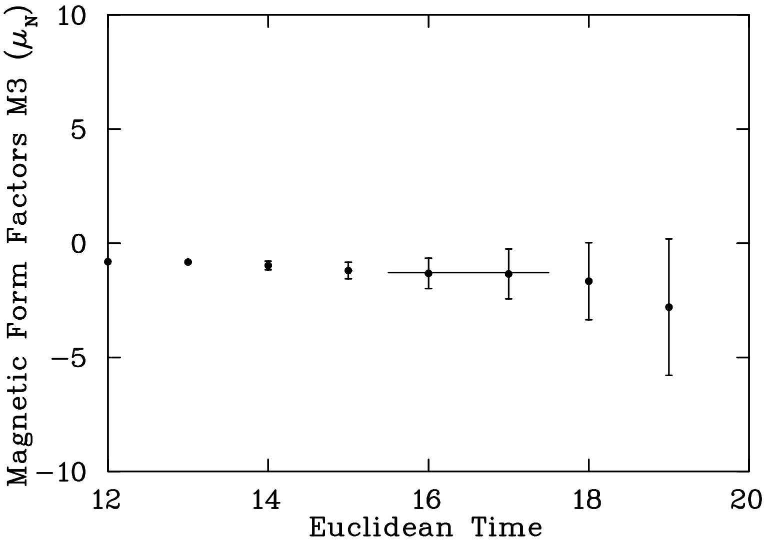

Figure 8.27: $M3$ Magnetic form factor (splitting) of the u or d quark in Δ as a function of time at the ninth quark mass where $m_\pi^2 = 0.2153(35)\text{GeV}^2$..

factors and the quadrupole moments we predict an oblate shape for the Δ^+, Δ^{++} and the Ω^- baryons. It will be interesting to confront this prediction with an experimental measurement of the Ω^- quadrupole form factor.

Chapter 9

Conclusions

This thesis reports details of the work I have done to calculate electromagnetic properties of the octet and decuplet baryons using numerical simulations of Lattice QCD. In Chapter 2 the fundamental concepts of elementary particles are given with special emphasis on the properties of octet and decuplet baryons. Chapter 3 captures the essential features and symmetries of Quantum Chromodynamics.

In Chapter 4, the role and methodology of Lattice QCD in calculation of observables is discussed. Finite volume and lattice spacing are the main causes for the artifacts and a number of innovative methods are used to reduce the errors. We have touched upon the various actions used.

For the current simulation we use the FLIC fermion action which offers reduced errors, of the order $\mathcal{O}(a^2)$ while maintaining current conservation. Another major advantage of using the FLIC fermion action is the access it provides to very light quark mass regime. We have succeeded in performing calculations efficiently at pion masses as low as 300 MeV.

In Chapter 5 a Chiral Perturbation Theory perspective of the baryon properties is given, since we compare our results with Quenched Chiral Perturbation theory for the octet baryons. The meson cloud around the baryons causes a non-analytic divergence in charge radii and magnetic moments of the baryons. Considering different pion loops in virtual decays of baryons, chiral coefficients for different baryons for all possible virtual transition channels are given. The charge radii and magnetic moments are expanded in terms of chiral coefficients. Hence the value of chiral coefficients gives a prediction of the non-analyticity of the charge radii and magnetic moments. For quick reference we have included the tables of chiral coefficients at the quark level and the baryon level for the octet baryons that is available from the literature.

Charge radii, magnetic radii and magnetic moments are calculated from the electric and magnetic form factors, which are calculated on the lattice. A detailed formalism with the required equations is given in Chapter 6, for the octet and the decuplet baryons. The form factors can be expressed as ratios of three-point correlation functions to two-point correlation functions. These ratios are calculated on the lattice for 400 configuration generated using Monte-Carlo methods. The data is then fit using the normal curve-fitting methods and averaging methods to extract the ratio of correlation functions with Jack-knifed errors.

We have calculated χ^2-per-degree-of-freedom to select the fit regime. We used covariance matrix methods to calculate the χ^2-per-degree-of-freedom. The details of the selection criteria are listed in Chapter 6, along with other techniques usually employed in Lattice QCD. Detailed results and discussions are given in Chapters 7 and 8.

We observe a non-analytic behavior in the charge radii and magnetic moments of the proton. The results are consistent with the predictions of the Quenched Chiral Perturbation theory, for the charged octet baryons.

We calculate the properties of the baryons from the properties of the quarks, using the appropriate charge factors. In the case of neutron, made of u and d quarks, the charge radii in the quark sectors are very close to each other. Combined with the proper charge factors, these contributions nearly cancel each other, leaving only their errors. Moreover, the cancellation is extremely sensitive to the selection of the fit-window. Hence for the neutron properties, it is necessary to approach the physical quark mass more closely to understand the chiral behavior.

We have held the strange quark mass fixed in our simulations. But the strange quark contribution to the properties of baryons depends upon the surrounding u and d quarks.

Our results exhibit the $SU(3)$-flavor symmetry at the ninth quark mass when $m_\pi^2 = 0.2153(35)\mathrm{GeV}^2$, as expected. The quarks in octet baryons exhibit environmental sensitivity, which increases with decrease in quark mass.

Simple quark model assumes that the contribution of u and d quarks to the magnetic moment of Λ^0 is zero and the entire magnetic moment of Λ^0 arises from the s quark. Our results prove that u and d quark contribute the magnetic moment of Λ^0, though much smaller than the contribution of the s quark.

The decuplet baryon results are analyzed and discussed in Chapter 8. Quarks in the decuplet baryon exhibit far less environmental sensitivity than those in the octet baryons.

The charge radii of the decuplet baryons are smaller than that of the octet baryons, which is a surprising result. The quarks in the decuplet baryons are identical states and one expects a small repulsion between them, causing a higher charge distribution. The fact that they are consistently lower than that of the octet baryons questions the validity of any such hyperfine repulsion model.

The magnetic moments of the decuplet baryons exhibit a small turn over as the quark mass reduces. This is a purely quenching effect. The magnitude of turn over is larger for baryons with lighter quarks. As the heavier s quark replaces the lighter u or d quarks, the turn over gets smaller. For the Ξ^* with two s quarks there is no visible turn over in the low quark mass regime.

The Ω^- baryon consists of three s quarks. Hence its properties must be equal to those of the other baryons in the $SU(3)$-flavor limit, when the masses of u and d quarks equal that of the s quark. For charge consistency, we took the values of Δ^- at the $SU(3)$-flavor limit as the properties of Ω^-.

The Ω^- is the only decuplet baryon that is stable against the strong interactions and hence any theoretical prediction of its properties is of interest. Our result for the mass of Ω^- overestimates the experimental value, while the magnetic moment underestimates the experimental value.

The K-Ξ loops are absent in the virtual decays of the Ω^- in quenched calculations while this would make non-trivial contributions in full QCD. This is one of the reasons for the underprediction of the magnetic moment of the Ω^-.

The decuplet baryons being spin-3/2 particles have four electromagnetic properties. We have presented $E2$ form factor results for the decuplet baryons which give important information about the symmetry of the charge distribution. A zero $E2$ form factor would mean a spherically symmetric distribution while a non-zero value implies a prolate or an oblate distribution.

Our results for $E2$ are with an unprecedented precision which helps us to establish that the decuplet baryons are indeed deformed. The value of $E2$ form factor for Δ^+ and Δ^{++} is negative while that of Ω^- is positive. Considering that Ω^- is a negatively charged baryon, this would mean that all of them have an oblate charge distribution.

The results for $M3$ form factor are consistent with zero.

The next step in this direction would be the calculation of the decuplet to octet transition moments.

It would also be quite interesting to explore if the lattice results showed any dependence on the volume of the lattice and lattice spacing. Reducing the lattice spacing and increasing the volume might remove errors and show any missing physics.

Lattice simulations with increased number of configurations should improve the statistics. Any improvement in actions that could give further access to the lower quark masses will greatly enable to study the chiral curvature of the properties.

Appendix A

Tables

Table A.1: Quark sector contributions to the electric form factors of the nucleon at $Q^2 = 0.227(2)$ GeV^2. Sector contributions are for a single quark having unit charge. The fit windows are selected using the criteria outlined in Sec. 6.5.3.

m_π^2		u_p			d_p	
(GeV^2)	fit value	fit window	χ^2/dof	fit value	fit window	χ^2/dof
0.9972(55)	0.798(5)	21 – 25	1.02	0.805(4)	21 – 25	2.36
0.8947(54)	0.789(5)	21 – 25	0.89	0.796(5)	21 – 25	2.53
0.7931(53)	0.779(6)	21 – 25	0.64	0.788(5)	21 – 25	2.21
0.6910(35)	0.768(6)	21 – 25	0.86	0.780(5)	21 – 25	1.57
0.5925(33)	0.756(7)	21 – 25	0.80	0.769(6)	21 – 25	1.42
0.4854(31)	0.740(9)	21 – 25	0.62	0.755(12)	21 – 25	1.19
0.3795(31)	0.725(10)	19 – 23	1.23	0.741(11)	19 – 23	0.77
0.2839(33)	0.708(12)	19 – 23	1.37	0.723(14)	19 – 23	1.31
0.2153(35)	0.693(15)	19 – 23	0.82	0.700(20)	19 – 23	1.23
0.1384(43)	0.682(17)	16 – 20	1.02	0.678(25)	16 – 20	0.89
0.0939(44)	0.666(25)	16 – 19	1.47	0.644(38)	16 – 19	1.28

Table A.2: Quark sector contributions to the electric form factors of Σ baryons at $Q^2 = 0.227(2)$ GeV^2. Sector contributions are for a single quark having unit charge. The fit windows are selected using the criteria outlined in Sec. 6.5.3.

m_π^2	u_Σ or d_Σ			s_Σ		
(GeV^2)	fit value	fit window	χ^2/dof	fit value	fit window	χ^2/dof
0.9972(55)	0.793(6)	21 – 25	0.91	0.759(6)	21 – 25	1.70
0.8947(54)	0.785(7)	21 – 25	0.86	0.758(7)	21 – 25	1.71
0.7931(53)	0.776(7)	21 – 25	0.66	0.757(8)	21 – 25	1.59
0.6910(35)	0.766(6)	21 – 25	1.00	0.757(6)	21 – 25	1.40
0.5925(33)	0.755(7)	21 – 25	0.90	0.756(7)	21 – 25	1.36
0.4854(31)	0.740(9)	21 – 25	0.62	0.755(9)	21 – 25	1.19
0.3795(31)	0.726(10)	19 – 23	1.46	0.754(10)	19 – 23	0.37
0.2839(33)	0.711(12)	19 – 23	1.78	0.753(11)	19 – 23	0.58
0.2153(35)	0.700(14)	19 – 23	0.73	0.752(13)	19 – 23	0.39
0.1384(43)	0.680(18)	19 – 21	0.73	0.754(17)	19 – 21	0.18
0.0939(44)	0.670(23)	19 – 21	1.30	0.750(26)	19 – 21	0.25

Table A.3: Quark sector contributions to the electric form factors of Λ at $Q^2 = 0.227(2)$ GeV^2. Sector contributions are for a single quark having unit charge. The fit windows are selected using the criteria outlined in Sec. 6.5.3.

m_π^2	u_Λ or d_Λ			s_Λ		
(GeV^2)	fit value	fit window	χ^2/dof	fit value	fit window	χ^2/dof
0.9972(55)	0.803(5)	21 – 25	1.20	0.745(8)	21 – 25	0.64
0.8947(54)	0.794(6)	21 – 25	1.23	0.744(9)	21 – 25	0.58
0.7931(53)	0.785(7)	21 – 25	1.06	0.744(10)	21 – 25	0.54
0.6910(35)	0.775(6)	21 – 25	1.17	0.738(8)	21 – 25	0.55
0.5925(33)	0.765(7)	21 – 25	1.12	0.737(9)	21 – 25	0.48
0.4854(31)	0.750(8)	21 – 25	1.02	0.735(10)	21 – 25	0.74
0.3795(31)	0.736(9)	19 – 23	0.94	0.734(11)	19 – 23	0.88
0.2839(33)	0.720(11)	19 – 23	1.17	0.730(12)	19 – 23	1.05
0.2153(35)	0.704(13)	19 – 23	1.23	0.727(13)	19 – 23	0.55
0.1384(43)	0.694(13)	16 – 19	3.79	0.727(13)	16 – 17	0.62
0.0939(44)	0.686(13)	16 – 17	2.43	0.729(14)	16 – 17	0.29

Table A.4: Quark sector contributions to the electric form factors of Ξ baryons at Q^2 = 0.227(2) GeV^2. Sector contributions are for a single quark having unit charge. The fit windows are selected using the criteria outlined in Sec. 6.5.3.

m_π^2		s_Ξ			u_Ξ or d_Ξ	
(GeV^2)	fit value	fit window	χ^2/dof	fit value	fit window	χ^2/dof
0.9972(55)	0.747(9)	21 – 25	0.34	0.804(8)	21 – 25	1.60
0.8947(54)	0.747(9)	21 – 25	0.36	0.794(8)	21 – 25	1.53
0.7931(53)	0.746(10)	21 – 25	0.37	0.785(9)	21 – 25	1.52
0.6910(35)	0.742(8)	21 – 25	0.54	0.778(7)	21 – 25	1.38
0.5925(33)	0.741(8)	21 – 25	0.55	0.768(8)	21 – 25	1.24
0.4854(31)	0.740(9)	21 – 25	0.62	0.755(9)	21 – 25	1.19
0.3795(31)	0.739(9)	19 – 23	0.70	0.740(10)	21 – 25	1.45
0.2839(33)	0.738(10)	19 – 23	1.18	0.723(13)	21 – 25	1.22
0.2153(35)	0.736(10)	19 – 23	1.42	0.709(16)	21 – 25	0.81
0.1384(43)	0.733(10)	19 – 22	0.52	0.690(19)	20 – 23	0.71
0.0939(44)	0.725(11)	19 – 23	1.21	0.672(22)	20 – 23	0.59

Table A.5: Quark sector contributions to the magnetic form factors of the nucleon at Q^2 = 0.227(2) GeV^2. Sector contributions are for a single quark having unit charge. The fit windows are selected using the criteria outlined in Sec. 6.5.3.

m_π^2 (GeV^2)		u_p (μ_N)			d_p (μ_N)	
	fit value	fit window	χ^2/dof	fit value	fit window	χ^2/dof
0.9972(55)	0.765(12)	19 – 23	1.78	−0.295(7)	18 – 22	0.61
0.8947(54)	0.785(14)	19 – 23	1.33	−0.298(8)	18 – 22	0.51
0.7931(53)	0.804(16)	19 – 23	1.01	−0.301(9)	18 – 22	0.43
0.6931(51)	0.817(13)	19 – 23	1.00	−0.301(8)	18 – 22	0.91
0.5944(51)	0.838(15)	19 – 23	0.73	−0.304(10)	18 – 22	0.79
0.4869(50)	0.861(20)	19 – 23	0.64	−0.306(12)	18 – 22	0.86
0.3795(31)	0.893(24)	17 – 21	0.14	−0.314(15)	16 – 18	1.64
0.2839(33)	0.932(31)	17 – 21	0.14	−0.313(19)	16 – 19	1.24
0.2153(35)	0.967(42)	17 – 21	0.61	−0.313(31)	16 – 20	0.53
0.1384(43)	1.034(52)	16 – 20	1.12	−0.309(40)	15 – 19	0.49
0.0939(44)	1.024(72)	15 – 17	0.82	−0.335(54)	15 – 17	2.92

Table A.6: Quark sector contributions to the magnetic form factors of Σ baryons at $Q^2 = 0.227(2)$ GeV^2. Sector contributions are for a single quark having unit charge. The fit windows are selected using the criteria outlined in Sec. 6.5.3.

m_π^2 (GeV^2)	u_Σ or d_Σ (μ_N)			s_Σ (μ_N)		
	fit value	fit window	χ^2/dof	fit value	fit window	χ^2/dof
0.9972(55)	0.775(14)	19 – 23	1.22	−0.316(10)	18 – 22	0.73
0.8947(54)	0.793(16)	19 – 23	1.10	−0.314(11)	18 – 22	0.63
0.7931(53)	0.810(18)	19 – 23	0.96	−0.312(11)	18 – 22	0.55
0.6910(35)	0.821(14)	19 – 23	0.98	−0.309(9)	18 – 22	0.94
0.5925(33)	0.840(16)	19 – 23	0.82	−0.308(10)	18 – 22	0.86
0.4854(31)	0.861(20)	19 – 23	0.64	−0.306(12)	18 – 22	0.86
0.3795(31)	0.886(23)	17 – 21	0.19	−0.308(13)	16 – 18	0.42
0.2839(33)	0.914(27)	17 – 21	0.26	−0.310(15)	16 – 18	0.03
0.2153(35)	0.941(32)	17 – 21	0.61	−0.317(19)	16 – 18	0.04
0.1384(43)	0.964(33)	15 – 20	1.57	−0.317(24)	16 – 18	0.92
0.0939(44)	0.969(41)	15 – 17	0.11	−0.322(28)	16 – 18	1.08

Table A.7: Quark sector contributions to the magnetic form factors of Λ at $Q^2 = 0.227(2)$ GeV^2. Sector contributions are for a single quark having unit charge. The fit windows are selected using the criteria outlined in Sec. 6.5.3.

m_π^2 (GeV^2)	u_Λ or d_Λ (μ_N)			s_Λ (μ_N)		
	fit value	fit window	χ^2/dof	fit value	fit window	χ^2/dof
0.9972(55)	0.069(9)	19 – 23	1.26	1.200(22)	18 – 22	1.38
0.8947(54)	0.072(9)	19 – 23	1.20	1.207(22)	18 – 22	1.17
0.7931(53)	0.075(10)	19 – 23	1.07	1.214(24)	18 – 22	0.99
0.6910(35)	0.079(8)	19 – 23	1.08	1.217(17)	18 – 22	0.95
0.5925(33)	0.083(9)	19 – 23	1.00	1.228(18)	18 – 22	0.80
0.4854(31)	0.087(11)	19 – 23	0.88	1.241(21)	18 – 22	0.75
0.3795(31)	0.091(12)	17 – 21	0.55	1.259(22)	16 – 20	0.59
0.2839(33)	0.097(13)	17 – 21	0.29	1.277(25)	16 – 20	0.42
0.2153(35)	0.099(17)	17 – 21	0.36	1.293(28)	16 – 20	0.42
0.1384(43)	0.105(18)	15 – 16	1.79	1.308(33)	16 – 18	0.94
0.0939(44)	0.105(22)	15 – 16	0.19	1.315(37)	15 – 16	1.98

Table A.8: Quark sector contributions to the magnetic form factors of Ξ baryons at $Q^2 = 0.227(2)$ GeV^2. Sector contributions are for a single quark having unit charge. The fit windows are selected using the criteria outlined in Sec. 6.5.3.

m_π^2 (GeV^2)	s_Ξ (μ_N)			u_Ξ or d_Ξ (μ_N)		
	fit value	fit window	χ^2/dof	fit value	fit window	χ^2/dof
0.9972(55)	0.846(27)	19 – 23	0.60	−0.290(10)	18 – 22	0.19
0.8947(54)	0.849(27)	19 – 23	0.67	−0.294(11)	18 – 22	0.21
0.7931(53)	0.851(28)	19 – 23	0.75	−0.299(12)	18 – 22	0.21
0.6931(51)	0.855(19)	19 – 23	0.41	−0.300(10)	18 – 22	0.59
0.5944(51)	0.858(19)	19 – 23	0.49	−0.303(11)	18 – 22	0.68
0.4869(50)	0.861(20)	19 – 23	0.64	−0.306(12)	18 – 22	0.86
0.3795(31)	0.866(21)	16 – 20	0.84	−0.311(13)	16 – 20	1.77
0.2839(33)	0.871(21)	16 – 20	0.78	−0.316(14)	16 – 20	1.66
0.2153(35)	0.875(22)	16 – 20	1.04	−0.322(15)	16 – 20	0.77
0.1384(43)	0.879(22)	16 – 20	1.16	−0.328(17)	15 – 19	0.86
0.0939(44)	0.879(23)	16 – 20	0.55	−0.333(18)	15 – 19	1.00

Table A.9: Electric charge radii of the nucleons with individual quark contributions,in fm^2 for different m_π^2 values in GeV^2.

m_π^2	u_p	d_p	p	n
0.9972(55)	0.243(7)	0.231(6)	0.247(8)	−0.007(3)
0.8947(54)	0.256(8)	0.245(7)	0.259(9)	−0.007(3)
0.7931(53)	0.270(9)	0.257(8)	0.273(10)	−0.008(4)
0.6910(35)	0.288(9)	0.270(9)	0.293(10)	−0.012(4)
0.5925(33)	0.307(11)	0.286(10)	0.313(12)	−0.014(5)
0.4854(31)	0.332(14)	0.309(14)	0.339(16)	−0.015(7)
0.3795(31)	0.358(17)	0.332(17)	0.367(19)	−0.017(8)
0.2839(33)	0.389(22)	0.362(24)	0.397(23)	−0.017(11)
0.2153(35)	0.416(27)	0.403(36)	0.420(29)	−0.008(16)
0.1384(43)	0.437(30)	0.444(46)	0.435(32)	0.005(21)
0.0939(44)	0.467(48)	0.510(77)	0.452(52)	0.029(40)

Table A.10: Electric charge radii of the Σ baryons with individual quark contributions in fm^2 for different m_π^2 values in GeV^2.

m_π^2	u_Σ	s_Σ	Σ^+	Σ^0	Σ^-
0.9972(55)	0.249(9)	0.301(10)	0.233(10)	−0.017(3)	−0.266(9)
0.8947(54)	0.262(10)	0.302(11)	0.249(12)	−0.013(3)	−0.275(9)
0.7931(53)	0.276(11)	0.304(12)	0.266(15)	−0.010(3)	−0.285(11)
0.6910(35)	0.291(10)	0.304(10)	0.286(11)	−0.005(2)	−0.295(9)
0.5925(33)	0.309(11)	0.306(11)	0.309(13)	0.001(3)	−0.308(11)
0.4854(31)	0.332(14)	0.309(14)	0.340(16)	0.008(4)	−0.324(13)
0.3795(31)	0.356(16)	0.310(15)	0.371(19)	0.015(4)	−0.341(15)
0.2839(33)	0.382(19)	0.312(18)	0.405(23)	0.023(5)	−0.359(18)
0.2153(35)	0.401(25)	0.315(21)	0.430(29)	0.029(6)	−0.372(22)
0.1384(43)	0.437(32)	0.311(26)	0.480(40)	0.042(8)	−0.395(28)
0.0939(44)	0.457(43)	0.318(41)	0.503(57)	0.046(15)	−0.410(37)

Table A.11: Electric charge radii of the Λ^0 baryon with individual quark contributions in fm^2 for different m_π^2 values n GeV^2.

m_π^2	u_Λ	s_Λ	Λ^0
0.9972(55)	0.235(8)	0.322(13)	−0.029(3)
0.8947(54)	0.248(9)	0.323(14)	−0.025(3)
0.7931(53)	0.262(10)	0.324(15)	−0.021(3)
0.6910(35)	0.276(9)	0.335(13)	−0.019(3)
0.5925(33)	0.293(10)	0.336(15)	−0.014(3)
0.4854(31)	0.316(13)	0.339(16)	−0.008(4)
0.3795(31)	0.340(15)	0.343(17)	−0.001(5)
0.2839(33)	0.367(18)	0.350(19)	0.006(5)
0.2153(35)	0.395(23)	0.357(22)	0.013(6)
0.1384(43)	0.414(24)	0.356(22)	0.019(63)
0.0939(44)	0.428(25)	0.354(23)	0.025(71)

Table A.12: Electric charge radii of the Ξ baryons with individual quark contributions in fm^2 for different m_π^2 values in GeV^2.

m_π^2	s_Ξ	u_Ξ	Ξ^-	Ξ^0
0.9972(55)	0.319(14)	0.235(11)	−0.290(12)	−0.056(7)
0.8947(54)	0.320(15)	0.249(12)	−0.296(13)	−0.047(7)
0.7931(53)	0.322(16)	0.262(13)	−0.301(14)	−0.039(8)
0.6910(35)	0.329(13)	0.273(11)	−0.310(11)	−0.037(6)
0.5925(33)	0.329(14)	0.288(12)	−0.316(12)	−0.028(7)
0.4854(31)	0.332(14)	0.309(14)	−0.324(13)	−0.015(7)
0.3795(31)	0.334(15)	0.333(17)	−0.333(14)	−0.0003(8)
0.2839(33)	0.337(15)	0.361(21)	−0.345(16)	0.016(10)
0.2153(35)	0.340(16)	0.385(27)	−0.355(18)	0.029(13)
0.1384(43)	0.345(16)	0.419(34)	−0.369(19)	0.049(19)
0.0939(44)	0.358(18)	0.451(41)	−0.389(23)	0.062(22)

Table A.13: Magnetic moment of the nucleons with individual quark contributions in nuclear magnetons for different values of m_π^2 in GeV^2.

m_π^2	u_p	d_p	p	n
0.9972(55)	0.960(13)	−0.366(8)	1.401(18)	−0.883(11)
0.8947(54)	0.995(15)	−0.373(9)	1.451(21)	−0.913(12)
0.7931(53)	1.032(18)	−0.382(10)	1.503(25)	−0.943(14)
0.6910(35)	1.063(14)	−0.386(10)	1.547(19)	−0.967(12)
0.5925(33)	1.108(17)	−0.395(12)	1.609(24)	−1.002(15)
0.4854(31)	1.163(23)	−0.406(16)	1.686(33)	−1.046(20)
0.3795(31)	1.231(29)	−0.424(20)	1.783(41)	−1.103(25)
0.2839(33)	1.317(41)	−0.433(28)	1.900(57)	−1.167(36)
0.2153(35)	1.394(62)	−0.447(47)	2.010(86)	−1.227(56)
0.1384(43)	1.517(79)	−0.456(59)	2.17(11)	−1.315(71)
0.0939(44)	1.54(11)	−0.521(87)	2.22(15)	−1.372(92)

Table A.14: Magnetic moments of the Ξ baryons with individual quark contributions in nuclear magnetons for different values of m_π^2 in GeV^2.

m_π^2	s_Ξ	u_Ξ	Ξ^0	Ξ^-
0.9972(55)	1.132(33)	−0.361(13)	−0.996(23)	−0.635(22)
0.8947(54)	1.137(34)	−0.371(14)	−1.005(24)	−0.634(23)
0.7931(53)	1.141(35)	−0.381(15)	−1.014(25)	−0.634(24)
0.6910(35)	1.152(21)	−0.385(13)	−1.024(18)	−0.640(14)
0.5925(33)	1.157(22)	−0.395(14)	−1.034(19)	−0.640(15)
0.4854(31)	1.163(24)	−0.406(16)	−1.046(20)	−0.640(16)
0.3795(31)	1.171(24)	−0.421(18)	−1.062(21)	−0.642(17)
0.2839(33)	1.181(25)	−0.437(20)	−1.079(23)	−0.642(17)
0.2153(35)	1.189(26)	−0.454(23)	−1.095(25)	−0.642(18)
0.1384(43)	1.199(29)	−0.475(27)	−1.115(29)	−0.641(20)
0.0939(44)	1.211(29)	−0.496(31)	−1.138(32)	−0.643(20)

Table A.15: Magnetic moment of the Σ baryons with individual quark contributions in nuclear magnetons for different values of m_π^2 in GeV^2.

m_π^2	u_Σ	s_Σ	Σ^+	Σ^0	Σ^-
0.9972(55)	0.976(15)	−0.416(13)	1.444(21)	0.464(7)	−0.512(10)
0.8947(54)	1.000(18)	−0.414(14)	1.484(24)	0.474(8)	−0.535(12)
0.7931(53)	1.044(20)	−0.412(15)	1.530(28)	0.485(9)	−0.559(14)
0.6910(35)	1.072(15)	−0.408(12)	1.565(21)	0.493(7)	−0.579(11)
0.5925(33)	1.113(18)	−0.407(13)	1.620(26)	0.507(8)	−0.607(13)
0.4854(31)	1.163(24)	−0.406(16)	1.686(33)	0.522(10)	−0.640(16)
0.3795(31)	1.221(27)	−0.409(18)	1.764(38)	0.543(12)	−0.678(18)
0.2839(33)	1.286(34)	−0.412(21)	1.852(47)	0.566(14)	−0.720(22)
0.2153(35)	1.344(42)	−0.421(27)	1.932(58)	0.588(18)	−0.756(28)
0.1384(43)	1.418(50)	−0.421(34)	2.031(72)	0.613(23)	−0.805(32)
0.0939(44)	1.446(77)	−0.429(42)	2.07(10)	0.625(30)	−0.821(53)

Table A.16: Magnetic moment of the Λ^0 in nuclear magnetons with quark contributions for different values of m_π^2 in GeV^2.

m_π^2	u_Λ	s_Λ	Λ^0
0.9972(55)	0.086(10)	1.611(29)	−0.509(9)
0.8947(54)	0.091(12)	1.621(20)	−0.510(10)
0.7931(53)	0.095(13)	1.631(32)	−0.512(10)
0.6910(35)	0.102(11)	1.650(21)	−0.516(8)
0.5925(33)	0.109(12)	1.666(24)	−0.519(8)
0.4854(31)	0.117(14)	1.689(28)	−0.524(10)
0.3795(31)	0.124(16)	1.715(32)	−0.530(11)
0.2839(33)	0.135(18)	1.749(37)	−0.538(13)
0.2153(35)	0.140(24)	1.780(43)	−0.547(16)
0.1384(43)	0.151(27)	1.799(49)	−0.549(18)
0.0939(44)	0.153(31)	1.804(53)	−0.550(20)

Table A.17: Magnetic radii of the nucleons and Σ baryons measured in fm^2 for different quark masses in GeV^2.

m_π^2	p	n	Σ^+	Σ^0	Σ^-
0.9972(55)	0.241(7)	0.240(6)	0.254(9)	0.264(9)	0.236(10)
0.8947(54)	0.255(8)	0.252(7)	0.265(10)	0.273(9)	0.252(10)
0.7931(53)	0.269(9)	0.266(9)	0.278(10)	0.283(10)	0.269(12)
0.6910(35)	0.286(9)	0.283(8)	0.292(10)	0.294(9)	0.287(11)
0.5925(33)	0.305(10)	0.301(10)	0.309(11)	0.308(11)	0.309(12)
0.4854(31)	0.330(14)	0.326(13)	0.330(14)	0.326(13)	0.337(15)
0.3795(31)	0.356(17)	0.351(16)	0.352(16)	0.344(15)	0.365(18)
0.2839(33)	0.387(21)	0.382(21)	0.377(20)	0.364(18)	0.396(22)
0.2153(35)	0.415(27)	0.413(28)	0.395(24)	0.380(22)	0.418(27)
0.1384(43)	0.438(30)	0.439(32)	0.429(32)	0.407(29)	0.462(36)
0.0939(44)	0.470(48)	0.478(50)	0.446(42)	0.423(38)	0.483(48)

Table A.18: Magnetic radii of the Λ^0 and Ξ baryons measured in fm^2 for different quark masses in GeV^2.

m_π^2	Λ	Ξ^0	Ξ^-
0.9972(55)	0.328(14)	0.298(13)	0.337(16)
0.8947(54)	0.328(14)	0.302(13)	0.335(17)
0.7931(53)	0.328(16)	0.306(13)	0.334(17)
0.6910(35)	0.339(14)	0.314(11)	0.340(14)
0.5925(33)	0.339(15)	0.319(12)	0.339(13)
0.4854(31)	0.342(17)	0.326(13)	0.337(15)
0.3795(31)	0.343(18)	0.333(14)	0.333(16)
0.2839(33)	0.348(20)	0.343(16)	0.332(16)
0.2153(35)	0.353(22)	0.352(17)	0.330(16)
0.1384(43)	0.351(22)	0.365(19)	0.328(17)
0.0939(44)	0.347(24)	0.384(22)	0.336(18)

Table A.19: Quark sector contributions to the electric form factor $E0$ of Δ at $Q^2 = 0.227(2)$ GeV^2. Sector contributions are for single quark having unit charge. The fit windows are selected using the criteria outlined in Sec. 6.5.3.The quark contribution at the $SU(3)$ limit when $m_\pi^2 = 0.4854$GeV^2 provides the s quark contribution in Ω^-.

m_π^2		u_Δ			d_Δ	
(GeV^2)	fit value	fit window	χ^2/dof	fit value	fit window	χ^2/dof
0.9972(55)	0.800(5)	20 – 24	1.47	0.800(6)	20 – 24	1.47
0.8947(54)	0.794(6)	20 – 24	0.95	0.794(6)	20 – 24	0.95
0.7931(53)	0.788(7)	20 – 24	0.79	0.788(7)	20 – 24	0.79
0.6910(35)	0.773(6)	20 – 24	1.46	0.773(6)	20 – 24	1.46
0.5925(33)	0.764(7)	20 – 24	1.07	0.764(7)	20 – 24	1.07
0.4854(31)	0.755(10)	20 – 24	0.53	0.755(10)	20 – 24	0.53
0.3795(31)	0.744(11)	17 – 20	0.73	0.744(11)	17 – 20	0.73
0.2839(33)	0.733(13)	17 – 20	0.79	0.733(13)	17 – 20	0.79
0.2153(35)	0.725(16)	17 – 19	0.46	0.725(16)	17 – 19	0.46
0.1384(43)	0.717(22)	17 – 19	0.23	0.717(22)	17 – 19	0.23
0.0939(44)	0.693(33)	17 – 19	0.34	0.693(33)	17 – 19	0.34

Table A.20: Quark sector contributions to the electric form factor $E0$ of Σ^* at $Q^2 = 0.227(2)$ GeV^2. Sector contributions are for a single quark having unit charge. The fit windows are selected using the criteria outlined in Sec. 6.5.3.

m_π^2		u_{Σ^*}			s_{Σ^*}	
(GeV^2)	fit value	fit window	χ^2/dof	fit value	fit window	χ^2/dof
0.9972(55)	0.804(6)	20 – 24	0.85	0.759(9)	20 – 24	0.54
0.8947(54)	0.798(7)	20 – 24	0.65	0.761(9)	20 – 24	0.50
0.7931(53)	0.792(8)	20 – 24	0.63	0.763(10)	20 – 24	0.49
0.6910(35)	0.774(6)	20 – 24	1.15	0.752(8)	20 – 24	0.97
0.5925(33)	0.764(8)	20 – 24	0.91	0.753(8)	20 – 24	0.79
0.4854(31)	0.755(10)	20 – 24	0.53	0.755(10)	20 – 24	0.53
0.3795(31)	0.744(11)	17 – 20	0.89	0.754(10)	17 – 20	0.22
0.2839(33)	0.733(12)	17 – 20	0.81	0.754(11)	17 – 20	0.37
0.2153(35)	0.727(14)	17 – 19	0.15	0.753(11)	17 – 19	0.21
0.1384(43)	0.719(18)	17 – 19	0.07	0.753(12)	17 – 19	0.05
0.0939(44)	0.710(23)	17 – 19	0.22	0.746(14)	17 – 19	0.63

Table A.21: Quark sector contributions to the electric form factor $E0$ of Ξ^* at Q^2 = 0.227(2) GeV^2. Sector contributions are for a single quark having unit charge. The fit windows are selected using the criteria outlined in Sec. 6.5.3.

m_π^2	s_{Ξ^*}			u_{Ξ^*}		
(GeV^2)	fit value	fit window	χ^2/dof	fit value	fit window	χ^2/dof
0.9972(55)	0.765(10)	20 – 24	0.47	0.809(8)	20 – 24	0.66
0.8947(54)	0.766(11)	20 – 24	0.47	0.802(8)	20 – 24	0.58
0.7931(53)	0.767(11)	20 – 24	0.49	0.795(9)	20 – 24	0.61
0.6910(35)	0.753(9)	20 – 24	0.73	0.775(7)	20 – 24	0.89
0.5925(33)	0.754(9)	20 – 24	0.66	0.765(8)	20 – 24	0.75
0.4854(31)	0.755(10)	20 – 24	0.53	0.755(10)	20 – 24	0.53
0.3795(31)	0.754(10)	17 – 20	0.19	0.744(10)	17 – 20	1.19
0.2839(33)	0.754(10)	17 – 20	0.22	0.734(11)	17 – 20	0.77
0.2153(35)	0.754(10)	17 – 19	0.03	0.727(13)	17 – 19	0.09
0.1384(43)	0.755(11)	17 – 19	0.11	0.720(14)	17 – 19	0.10
0.0939(44)	0.754(11)	17 – 19	0.66	0.714(11)	17 – 19	0.19

Table A.22: Quark sector contributions to the magnetic form factor $M1$ of Δ at Q^2 = 0.227(2) GeV^2. Sector contributions are for a single quark having unit charge. The fit windows are selected using the criteria outlined in Sec. 6.5.3. The quark contribution at the $SU(3)$ limit when $m_\pi^2 = 0.4854$GeV^2 provides the s quark contribution in Ω^-.

m_π^2 (GeV^2)	u_Δ (μ_N)			d_Δ (μ_N)		
	fit value	fit window	χ^2/dof	fit value	fit window	χ^2/dof
0.9972(55)	1.173(25)	19 – 24	1.45	1.173(25)	19 – 24	1.45
0.8947(54)	1.201(29)	19 – 24	1.14	1.201(29)	19 – 24	1.14
0.7931(53)	1.230(33)	19 – 24	0.95	1.230(33)	19 – 24	0.95
0.6910(35)	1.248(32)	19 – 24	1.25	1.248(32)	19 – 24	1.25
0.5925(33)	1.269(41)	19 – 24	0.79	1.269(41)	19 – 24	0.79
0.4854(31)	1.280(56)	19 – 24	0.31	1.280(56)	19 – 24	0.31
0.3795(31)	1.301(64)	17 – 21	1.37	1.301(64)	17 – 21	1.37
0.2839(33)	1.312(75)	17 – 19	1.14	1.312(75)	17 – 19	1.14
0.2153(35)	1.309(89)	17 – 19	0.91	1.309(89)	17 – 19	0.91
0.1384(43)	1.28(12)	17 – 18	1.26	1.28(12)	17 – 18	1.26
0.0939(44)	1.11(22)	17 – 18	1.79	1.11(22)	17 – 18	1.79

Table A.23: Quark sector contributions to the magnetic form factor $M1$ of Σ^* at Q^2 = 0.227(2) GeV^2. Sector contributions are for a single quark having unit charge. The fit windows are selected using the criteria outlined in Sec. 6.5.3.

m_π^2 (GeV^2)	u_{Σ^*} or d_{Σ^*} (μ_N)			s_{Σ^*} (μ_N)		
	fit value	fit window	χ^2/dof	fit value	fit window	χ^2/dof
0.9972(55)	1.191(31)	19 – 24	1.07	1.268(40)	19 – 24	0.51
0.8947(54)	1.216(35)	19 – 24	0.90	1.275(42)	19 – 24	0.49
0.7931(53)	1.242(39)	19 – 24	0.82	1.282(45)	19 – 24	0.47
0.6910(35)	1.254(37)	19 – 24	0.94	1.275(41)	19 – 24	0.69
0.5925(33)	1.272(45)	19 – 24	0.64	1.278(47)	19 – 24	0.51
0.4854(31)	1.280(56)	19 – 24	0.31	1.280(56)	19 – 24	0.31
0.3795(31)	1.297(62)	17 – 21	1.72	1.289(60)	17 – 21	0.70
0.2839(33)	1.306(68)	17 – 19	1.88	1.299(65)	17 – 19	0.04
0.2153(35)	1.305(76)	17 – 19	1.84	1.309(69)	17 – 19	0.08
0.1384(43)	1.299(89)	17 – 19	3.44	1.330(74)	17 – 19	0.44
0.0939(44)	1.249(12)	17 – 18	2.55	1.303(88)	17 – 18	0.16

Table A.24: Quark sector contributions to the magnetic form factor $M1$ of Ξ^* at Q^2 = 0.227(2) GeV^2. Sector contributions are for a single quark having unit charge. The fit windows are selected using the criteria outlined in Sec. 6.5.3.

m_π^2 (GeV^2)	s_{Ξ^*} (μ_N)			u_{Ξ^*} or d_{Ξ^*} (μ_N)		
	fit value	fit window	χ^2/dof	fit value	fit window	χ^2/dof
0.9972(55)	1.286(50)	19 – 24	0.45	1.208(39)	19 – 24	0.84
0.8947(54)	1.289(52)	19 – 24	0.46	1.231(42)	19 – 24	0.79
0.7931(53)	1.293(54)	19 – 24	0.46	1.254(46)	19 – 24	0.76
0.6910(35)	1.278(48)	19 – 24	0.48	1.260(44)	19 – 24	0.68
0.5925(33)	1.280(51)	19 – 24	0.40	1.274(49)	19 – 24	0.52
0.4854(31)	1.280(56)	19 – 24	0.31	1.280(56)	19 – 24	0.31
0.3795(31)	1.285(58)	17 – 21	0.70	1.293(60)	17 – 21	2.56
0.2839(33)	1.289(60)	17 – 19	0.04	1.300(63)	17 – 19	2.66
0.2153(35)	1.293(62)	17 – 19	0.02	1.303(66)	17 – 19	1.44
0.1384(43)	1.302(64)	17 – 18	0.73	1.303(72)	17 – 18	2.36
0.0939(44)	1.301(67)	17 – 18	0.23	1.313(81)	17 – 18	0.56

Table A.25: Charge radius of the Δ with individual quark contributions in fm^2 for different m_π^2 in GeV^2. The quark contributions at the $SU(3)$ flavor limit provide the s quark contributions per unit quark charge in the Ω^-. Charge radius of Δ^- is equal to that of Δ^+ with a negative sign and that of Δ^0 is 0.

m_π^2	u_Δ	d_Δ	Δ
0.9972(55)	0.238(7)	0.238(7)	0.238(7)
0.8947(54)	0.247(8)	0.247(8)	0.247(8)
0.7931(53)	0.256(10)	0.256(10)	0.256(10)
0.6910(35)	0.279(9)	0.279(9)	0.279(9)
0.5925(33)	0.293(10)	0.293(10)	0.293(10)
0.4854(31)	0.307(15)	0.307(15)	0.307(15)
0.3795(31)	0.324(17)	0.324(17)	0.324(17)
0.2839(33)	0.343(21)	0.343(21)	0.343(21)
0.2153(35)	0.355(26)	0.355(26)	0.355(26)
0.1384(43)	0.370(37)	0.370(37)	0.370(37)
0.0939(44)	0.410(57)	0.410(57)	0.410(57)

Table A.26: Charge radii of the Σ^* states with individual quark contributions in fm^2 for different values of m_π^2 in GeV^2.

m_π^2	u_{Σ^*}	s_{Σ^*}	Σ^{*+}	Σ^{*0}	Σ^{*-}
0.9972(55)	0.233(8)	0.299(13)	0.212(8)	−0.022(3)	0.255(10)
0.8947(54)	0.242(10)	0.296(14)	0.224(9)	−0.018(2)	0.260(11)
0.7931(53)	0.251(11)	0.293(15)	0.237(10)	−0.014(2)	0.265(12)
0.6910(35)	0.278(10)	0.311(12)	0.267(9)	−0.011(1)	0.289(10)
0.5925(33)	0.292(12)	0.309(13)	0.286(11)	−0.006(1)	0.298(12)
0.4854(31)	0.307(15)	0.307(15)	0.307(15)	0.000(0)	0.307(15)
0.3795(31)	0.324(17)	0.308(16)	0.329(17)	0.0006(1)	0.319(16)
0.2839(33)	0.341(20)	0.309(17)	0.353(21)	0.011(1)	0.330(19)
0.2153(35)	0.352(23)	0.309(17)	0.367(25)	0.014(2)	0.338(21)
0.1384(43)	0.365(29)	0.310(18)	0.384(34)	0.018(5)	0.347(26)
0.0939(44)	0.380(39)	0.321(22)	0.400(46)	0.019(7)	0.360(32)

Table A.27: Charge radii of the Ξ^* states with individual quark contributions in fm^2 for different values of m_π^2 in GeV^2.

m_π^2	s_{Ξ^*}	u_{Ξ^*}	Ξ^{*-}	Ξ^{*0}
0.9972(55)	0.291(16)	0.227(11)	0.269(14)	−0.042(5)
0.8947(54)	0.289(16)	0.236(12)	0.271(14)	−0.035(5)
0.7931(53)	0.287(17)	0.246(13)	0.273(15)	−0.027(4)
0.6910(35)	0.309(13)	0.276(11)	0.298(12)	−0.022(3)
0.5925(33)	0.308(14)	0.291(12)	0.302(14)	−0.011(2)
0.4854(31)	0.307(15)	0.307(15)	0.307(15)	0.0($e-14$)
0.3795(31)	0.307(15)	0.324(16)	0.313(16)	0.011(1)
0.2839(33)	0.307(16)	0.340(19)	0.318(17)	0.022(3)
0.2153(35)	0.307(16)	0.351(21)	0.322(17)	0.029(4)
0.1384(43)	0.307(16)	0.363(24)	0.325(19)	0.037(7)
0.0939(44)	0.308(17)	0.372(29)	0.329(20)	0.043(10)

Table A.28: Magnetic moment of the Δ in nuclear magnetons with individual quark contributions for different m_π^2 in GeV^2. Magnetic moment of Δ^- is equal to that of Δ^+ with a negative sign and that of Δ^0 is 0. Magnetic moment of Δ^{++} is equal to twice that of Δ^+. Magnetic moment of Ω^- is that of Δ^- at the $SU(3)$ flavor limit.

m_π^2	u_Δ	d_Δ	Δ
0.9972(55)	1.466(31)	1.466(31)	1.466(31)
0.8947(54)	1.512(36)	1.512(36)	1.512(36)
0.7931(53)	1.559(42)	1.559(42)	1.559(42)
0.6910(35)	1.615(38)	1.615(38)	1.615(38)
0.5925(33)	1.662(48)	1.662(48)	1.662(48)
0.4854(31)	1.697(65)	1.697(65)	1.697(65)
0.3795(31)	1.749(74)	1.749(74)	1.749(74)
0.2839(33)	1.792(87)	1.792(87)	1.792(87)
0.2153(35)	1.80(10)	1.80(10)	1.80(10)
0.1384(43)	1.78(15)	1.78(15)	1.78(15)
0.0939(44)	1.60(28)	1.60(28)	1.60(28)

Table A.29: Magnetic moments of Σ^* in nuclear magnetons with individual quark sector contributions for different values of m_π^2 in GeV^2 .

m_π^2	u_{Σ^*}	s_{Σ^*}	Σ^{*+}	Σ^{*0}	Σ^{*-}
0.9972(55)	1.482(38)	1.671(51)	1.418(36)	−0.063(7)	−1.545(42)
0.8947(54)	1.524(43)	1.675(54)	1.474(41)	−0.050(6)	−1.574(46)
0.7931(53)	1.568(48)	1.680(57)	1.531(47)	−0.037(6)	−1.606(51)
0.6910(35)	1.621(44)	1.695(48)	1.596(43)	−0.025(3)	−1.646(45)
0.5925(33)	1.664(52)	1.697(54)	1.653(51)	−0.011(2)	−1.675(53)
0.4854(31)	1.697(15)	1.697(65)	1.697(65)	0.000(0)	−1.697(65)
0.3795(31)	1.744(17)	1.709(69)	1.755(72)	0.012(2)	−1.732(71)
0.2839(33)	1.781(20)	1.724(75)	1.800(82)	0.019(5)	−1.762(78)
0.2153(35)	1.796(23)	1.738(80)	1.816(95)	0.020(10)	−1.777(85)
0.1384(43)	1.807(29)	1.766(86)	1.82(12)	0.013(21)	−1.793(97)
0.0939(44)	1.759(39)	1.747(10)	1.76(18)	0.004(40)	−1.75(12)

Table A.30: Magnetic moments of Ξ^* in nuclear magnetons with individual quark sector contributions for different values of m_π^2 in GeV^2.

m_π^2	s_{Ξ^*}	u_{Ξ^*}	Ξ^{*-}	Ξ^{*0}
0.9972(55)	1.681(63)	1.494(48)	−1.619(57)	−0.124(18)
0.8947(54)	1.683(65)	1.534(52)	−1.633(60)	−0.099(16)
0.7931(53)	1.685(66)	1.576(56)	−1.649(63)	−0.073(14)
0.6910(35)	1.697(56)	1.626(51)	−1.674(54)	−0.047(6)
0.5925(33)	1.698(59)	1.666(57)	−1.687(58)	−0.021(4)
0.4854(31)	1.697(65)	1.697(65)	−1.697(15)	0.0(e − 14)
0.3795(31)	1.703(67)	1.738(69)	−1.714(68)	0.023(1)
0.2839(33)	1.709(69)	1.772(73)	−1.730(70)	0.042(9)
0.2153(35)	1.714(71)	1.792(78)	−1.740(73)	0.052(16)
0.1384(43)	1.725(73)	1.811(86)	−1.753(75)	0.057(31)
0.0939(44)	1.725(77)	1.84(10)	−1.763(79)	0.076(48)

Table A.31: Quark sector contributions to the electric form factor $E2$ of Δ at $Q^2 = 0.227(2)$ GeV^2. Sector contributions are for a single quark having unit charge. The fit windows are selected using the criteria outlined in Sec. 6.5.3. The quark contribution at the $SU(3)$ limit when $m_\pi^2 = 0.4854$GeV^2 provides the s quark contribution in Ω^-.

m_π^2 (GeV^2)	u_Δ (e/M_N^2)			d_Δ (e/M_N^2)		
	fit value	fit window	χ^2/dof	fit value	fit window	χ^2/dof
0.9972(55)	−0.117(16)	16 – 20	1.63	−0.117(16)	16 – 20	1.63
0.8947(54)	−0.123(18)	16 – 20	1.39	−0.123(18)	16 – 20	1.39
0.7931(53)	−0.130(22)	16 – 20	1.16	−0.130(22)	16 – 20	1.16
0.6910(35)	−0.163(17)	16 – 20	0.76	−0.163(17)	16 – 20	0.76
0.5925(33)	−0.177(21)	16 – 20	0.75	−0.177(21)	16 – 20	0.75
0.4854(31)	−0.194(27)	16 – 20	0.86	−0.194(27)	16 – 20	0.86
0.3795(31)	−0.218(40)	16 – 19	1.03	−0.218(40)	16 – 19	1.03
0.2839(33)	−0.263(67)	16 – 19	1.57	−0.263(67)	16 – 19	1.57
0.2153(35)	−0.32(11)	16 – 19	1.20	−0.31(11)	16 – 19	1.20
0.1384(43)	−0.52(20)	16 – 18	0.72	−0.52(20)	16 – 18	0.72
0.0939(44)	−0.68(26)	15 – 16	1.06	−0.68(26)	15 – 16	1.06

Table A.32: Quark sector contributions to the electric form factor $E2$ of Σ^* at Q^2 = 0.227(2) GeV^2. Sector contributions are for a single quark having unit charge. The fit windows are selected using the criteria outlined in Sec. 6.5.3.

m_π^2 (GeV^2)	u_{Σ^*} or d_{Σ^*} (e/M_N^2)			s_{Σ^*} (e/M_N^2)		
	fit value	fit window	χ^2/dof	fit value	fit window	χ^2/dof
0.9972(55)	−0.132(19)	16 – 20	1.52	−0.113(29)	16 – 20	0.75
0.8947(54)	−0.136(22)	16 – 20	1.36	−0.118(31)	16 – 20	0.64
0.7931(53)	−0.145(25)	16 – 20	1.20	−0.124(33)	16 – 20	0.66
0.6910(35)	−0.172(18)	16 – 20	0.91	−0.170(22)	16 – 20	0.48
0.5925(33)	−0.183(22)	16 – 20	0.89	−0.180(24)	16 – 20	0.61
0.4854(31)	−0.194(27)	16 – 20	0.86	−0.194(27)	16 – 20	0.86
0.3795(31)	−0.208(36)	16 – 20	0.48	−0.211(32)	16 – 20	1.89
0.2839(33)	−0.225(51)	16 – 17	0.41	−0.231(38)	16 – 17	0.61
0.2153(35)	−0.233(73)	16 – 19	1.08	−0.257(48)	16 – 19	1.84
0.1384(43)	−0.29(11)	16 – 17	1.71	−0.300(67)	16 – 17	1.07
0.0939(44)	−0.42(16)	16 – 17	0.94	−0.325(88)	16 – 17	0.31

Table A.33: Quark sector contributions to the electric form factor $E2$ of Ξ^* at Q^2 = 0.227(2) GeV^2. Sector contributions are for a single quark having unit charge. The fit windows are selected using the criteria outlined in Sec. 6.5.3.

m_π^2 (GeV^2)	s_{Ξ^*} (e/M_N^2)			u_{Ξ^*} or d_{Ξ^*} (e/M_N^2)		
	fit value	fit window	χ^2/dof	fit value	fit window	χ^2/dof
0.9972(55)	−0.127(36)	16 – 20	0.64	−0.157(25)	16 – 20	1.75
0.8947(54)	−0.131(37)	16 – 20	0.64	−0.157(27)	16 – 20	1.52
0.7931(53)	−0.136(39)	16 – 20	0.64	−0.159(30)	16 – 20	1.35
0.6910(35)	−0.180(24)	16 – 20	0.65	−0.184(20)	16 – 20	1.17
0.5925(33)	−0.186(25)	16 – 20	0.73	−0.190(23)	16 – 20	1.04
0.4854(31)	−0.194(27)	16 – 20	0.86	−0.194(27)	16 – 20	0.86
0.3795(31)	−0.201(29)	16 – 17	0.82	−0.198(33)	16 – 21	0.62
0.2839(33)	−0.208(31)	16 – 17	0.59	−0.200(41)	16 – 17	0.23
0.2153(35)	−0.214(34)	16 – 17	0.80	−0.191(52)	16 – 17	0.06
0.1384(43)	−0.222(38)	16 – 17	0.92	−0.184(71)	16 – 18	0.34
0.0939(44)	−0.222(41)	15 – 16	0.17	−0.183(82)	15 – 16	0.70

Table A.34: Electric form factor $E2$ of the charged decuplet baryons in units of 10^{-2}fm^2 for different m_π^2 values.The $E2$ form factor of the Δ^- at the $SU(3)$ flavor limit is the $E2$ form factor of Ω^-.

m_π^2 (GeV^2)	Δ^{++}	Δ^+	Δ^-	Σ^{*+}	Σ^{*-}	Ξ^{*-}
0.9972(55)	−1.03(14)	−0.515(68)	0.515(68)	−0.610(77)	0.553(97)	0.60(14)
0.8947(54)	−1.08(16)	−0.539(80)	0.539(80)	−0.626(87)	0.57(11)	0.62(15)
0.7931(53)	−1.15(19)	−0.573(95)	0.573(95)	−0.65(10)	0.60(12)	0.63(16)
0.6910(35)	−1.43(15)	−0.716(75)	0.716(75)	−0.762(77)	0.754(85)	0.80(10)
0.5925(33)	−1.56(18)	−0.779(90)	0.779(90)	−0.810(92)	0.801(98)	0.83(11)
0.4854(31)	−1.17(23)	−0.85(12)	0.85(12)	−0.85(12)	0.85(12)	0.85(12)
0.3795(31)	−1.92(35)	−0.96(17)	0.96(17)	−0.91(17)	0.92(15)	0.88(13)
0.2839(33)	−2.31(59)	−1.16(29)	1.16(29)	−0.98(24)	0.99(20)	0.90(15)
0.2153(35)	−2.78(95)	−1.39(47)	1.39(47)	−0.99(37)	1.06(28)	0.91(17)
0.1384(43)	−4.6(1.8)	−2.30(88)	2.30(88)	−1.27(58)	1.29(41)	0.92(21)
0.0939(44)	−6.0(2.2)	−3.0(1.1)	3.0(1.1)	−1.99(85)	1.71(56)	0.92(22)

Table A.35: Quark sector contributions to the magnetic form factor $M3$ of Δ at Q^2 = 0.227(2) GeV^2. Sector contributions are for a single quark having unit charge. The fit windows are selected using the criteria outlined in Sec. 6.5.3. The quark contribution at the $SU(3)$ limit when m_π^2 = 0.4854GeV^2 provide the s quark contribution in Ω^-.

m_π^2 (GeV^2)		u_Δ			d_Δ	
	fit value	fit window	χ^2/dof	fit value	fit window	χ^2/dof
0.9972(55)	0.32(53)	18 – 20	0.19	0.32(53)	18 – 20	0.19
0.8947(54)	0.34(63)	18 – 20	0.22	0.34(63)	18 – 20	0.22
0.7931(53)	0.35(76)	18 – 20	0.76	0.35(76)	18 – 20	0.76
0.6910(35)	−0.01(69)	18 – 20	0.90	−0.01(69)	18 – 20	0.90
0.5925(33)	−0.09(87)	18 – 20	1.00	−0.09(87)	18 – 20	1.00
0.4854(31)	−0.2(1.2)	18 – 20	0.92	−0.2(1.2)	18 – 20	0.92
0.3795(31)	−0.4(1.4)	16 – 18	0.44	−0.4(1.4)	16 – 18	0.44
0.2839(33)	−0.8(1.8)	16 – 18	0.16	−0.8(1.8)	16 – 18	0.16
0.2153(35)	−1.4(2.4)	16 – 18	0.01	−1.4(2.4)	16 – 18	0.01
0.1384(43)	−2.6(3.0)	15 – 17	0.28	−2.6(3.0)	15 – 17	0.28
0.0939(44)	−3.8(3.8)	15 – 17	0.32	−3.8(3.8)	15 – 17	0.32

Table A.36: Quark sector contributions to the magnetic form factor $M3$ of Σ^* at Q^2 = 0.227(2) GeV^2. Sector contributions are for a single quark having unit charge. The fit windows are selected using the criteria outlined in Sec. 6.5.3.

m_π^2 (GeV^2)	u_{Σ^*} or d_{Σ^*}			s_{Σ^*}		
	fit value	fit window	χ^2/dof	fit value	fit window	χ^2/dof
0.9972(55)	0.30(75)	18 – 20	0.34	0.74(75)	18 – 20	0.07
0.8947(54)	0.31(84)	16 – 20	0.37	0.75(84)	18 – 20	0.07
0.7931(53)	0.28(96)	18 – 20	0.39	0.73(96)	18 – 20	0.09
0.6910(35)	−0.08(82)	18 – 20	0.99	0.01(83)	18 – 20	0.78
0.5925(33)	−0.15(96)	18 – 20	1.03	−0.09(97)	18 – 20	0.41
0.4854(31)	−0.2(1.2)	18 – 20	0.92	−0.2(1.2)	18 – 20	0.92
0.3795(31)	−0.3(1.3)	16 – 18	0.43	−0.3(1.3)	16 – 18	0.55
0.2839(33)	−0.5(1.5)	16 – 18	0.10	−0.4(1.5)	16 – 18	0.56
0.2153(35)	−0.7(1.7)	16 – 18	0.03	−0.5(1.7)	16 – 18	0.13
0.1384(43)	−1.1(1.9)	15 – 16	1.91	−0.8(1.9)	15 – 16	0.02
0.0939(44)	−1.2(2.2)	15 – 16	0.004	−1.1(2.1)	15 – 16	1.33

Table A.37: Quark sector contributions to the magnetic form factor $M3$ of Ξ^* at Q^2 = 0.227(2) GeV^2. Sector contributions are for a single quark having unit charge. The fit windows are selected using the criteria outlined in Sec. 6.5.3.

m_π^2 (GeV^2)	s_{Ξ^*}			u_{Ξ^*} or d_{Ξ^*}		
	fit value	fit window	χ^2/dof	fit value	fit window	χ^2/dof
0.9972(55)	0.8(1.1)	18 – 20	0.10	0.1(1.1)	18 – 20	0.46
0.8947(54)	0.7(1.1)	18 – 20	0.12	0.1(1.2)	18 – 20	0.50
0.7931(53)	0.7(1.2)	18 – 20	0.15	0.1(1.2)	18 – 20	0.60
0.6910(35)	−0.08(98)	18 – 20	0.85	−0.21(99)	18 – 20	1.06
0.5925(33)	−0.2(1.1)	18 – 20	0.92	−0.2(1.1)	18 – 20	1.03
0.4854(31)	−0.2(1.2)	18 – 20	0.92	−0.2(1.2)	18 – 20	0.92
0.3795(31)	−0.3(1.3)	16 – 18	0.55	−0.4(1.3)	16 – 18	0.15
0.2839(33)	−0.3(1.3)	16 – 18	0.99	−0.4(1.4)	16 – 18	0.05
0.2153(35)	−0.3(1.4)	16 – 17	0.80	−0.4(1.4)	16 – 17	0.06
0.1384(43)	−0.3(1.4)	15 – 17	0.23	−0.6(1.5)	15 – 17	0.47
0.0939(44)	−0.4(1.5)	15 – 17	0.44	−0.3(1.6)	15 – 17	0.82

Table A.38: Coefficients, χ, providing the LNA contribution to baryon magnetic moments and charge radii in quenched QCD. Coefficients for magnetic moments in full QCD are also indicated. Here the coefficients for quark sector contributions to baryon properties are indicated for quarks having unit charge. Note that u_p for example denotes the coefficient for the two u quarks of the proton, each of which have unit charge. Intermediate (Int.) meson-baryon channels are indicated to allow for $SU(3)$-flavor breaking in both the meson and baryon masses. The coefficients are calculated from the expressions of Ref. [45] with the axial couplings $F = 0.50$ and $D = 0.76$ with $f_\pi = 93$ MeV.

q	Int.	Full QCD	Quenched QCD
$u_p \mid d_n$	$N\pi$	−6.87	−3.33
	ΛK	−3.68	0
	ΣK	−0.15	0
$d_p \mid u_n$	$N\pi$	+6.87	+3.33
	ΣK	−0.29	0
$s_p \mid s_n$	ΛK	+3.68	0
	ΣK	+0.44	0
$u_{\Sigma^+} \mid d_{\Sigma^-}$	$\Sigma\pi$	−2.16	0
	$\Lambda\pi$	−1.67	0
	NK	0	−0.29
	ΞK	−6.87	−3.04
$d_{\Sigma^+} \mid u_{\Sigma^-}$	$\Sigma\pi$	+2.16	0
	$\Lambda\pi$	+1.67	0
	NK	+0.29	0
s_Σ	NK	−0.29	+0.29
	ΞK	+6.87	+3.04
	$\Sigma\eta_s$	0	0
$u_{\Sigma^0} \mid d_{\Sigma^0}$	$\Sigma\pi$	0	0
	$\Lambda\pi$	0	0
	NK	+0.15	−0.15
	ΞK	−3.43	−1.52
$u_\Lambda \mid d_\Lambda$	$\Sigma\pi$	0	0
	$\Lambda\eta_l$	0	0
	NK	+3.68	+1.23
	ΞK	−0.40	+0.44
s_Λ	$\Lambda\eta_s$	0	0
	NK	−7.36	−2.45
	ΞK	+0.79	−0.88
$u_{\Xi^0} \mid d_{\Xi^-}$	$\Xi\pi$	−0.29	0
	ΛK	0	−0.40
	ΣK	+6.87	+3.43
	ΩK	0	+0.29
$d_{\Xi^0} \mid u_{\Xi^-}$	$\Xi\pi$	+0.29	0
	ΛK	+0.40	0
	ΣK	+3.43	0
s_Ξ	ΛK	−0.40	+0.40
	ΣK	−10.3	−3.43
	ΩK	0	−0.29
	$\Xi\eta_s$	0	0

Table A.39: Coefficients, χ, providing the LNA contribution to baryon magnetic moments and charge radii in quenched QCD. Coefficients for magnetic moments in full QCD are also indicated. Intermediate (Int.) meson-baryon channels are indicated to allow for $SU(3)$-flavor breaking in both the meson and baryon masses. The coefficients are calculated from the expressions of Ref. [45] with the axial couplings $F = 0.50$ and $D = 0.76$ with $f_\pi = 93$ MeV.

Baryon	Channel	Full QCD	Quenched QCD
p	$N\pi$	−6.87	−3.33
	ΛK	−3.68	0
	ΣK	−0.15	0
n	$N\pi$	+6.87	+3.33
	ΛK	0	0
	ΣK	−0.29	0
Σ^+	$\Sigma\pi$	−2.16	0
	$\Lambda\pi$	−1.67	0
	NK	0	−0.29
	ΞK	−6.87	−3.04
	$\Sigma\eta_s$	0	0
Σ^0	$\Sigma\pi$	0	0
	$\Lambda\pi$	0	0
	NK	+0.15	−0.15
	ΞK	−3.43	−1.52
	$\Sigma\eta_s$	0	0
Σ^-	$\Sigma\pi$	+2.16	0
	$\Lambda\pi$	+1.67	0
	NK	+0.29	0
	ΞK	0	0
	$\Sigma\eta_s$	0	0
Λ	$\Sigma\pi$	0	0
	$\Lambda\eta_l$	0	0
	NK	+3.68	+1.23
	ΞK	−0.40	+0.44
	$\Lambda\eta_s$	0	0
Ξ^0	$\Xi\pi$	−0.29	0
	ΛK	0	−0.40
	ΣK	+6.87	+3.43
	ΩK	0	+0.29
	$\Xi\eta_s$	0	0
Ξ^-	$\Xi\pi$	+0.29	0
	ΛK	+0.40	0
	ΣK	+3.43	0
	ΩK	0	0
	$\Xi\eta_s$	0	0

Appendix B

Gamma Matrices

We use the usual definition of Pauli matrices given as

$$\sigma^1 = \begin{pmatrix} 0 & 1 \\ 1 & 0 \end{pmatrix} \quad \sigma^2 = \begin{pmatrix} 0 & -i \\ i & 0 \end{pmatrix} \quad \sigma^3 = \begin{pmatrix} 1 & 0 \\ 0 & -1 \end{pmatrix} .$$

B.1 Dirac Representation

In the Dirac representation the γ matrices are given by

$$\begin{aligned} \gamma^i &= \begin{pmatrix} 0 & \sigma^i \\ -\sigma^i & 0 \end{pmatrix} \\ \gamma^0 &= \begin{pmatrix} I & 0 \\ 0 & -I \end{pmatrix} \\ \gamma_5 = \gamma^5 &= -\begin{pmatrix} 0 & I \\ I & 0 \end{pmatrix} \\ \gamma^5\gamma^i &= \begin{pmatrix} -\sigma^i & 0 \\ 0 & \sigma^i \end{pmatrix} \\ \gamma^5\gamma^0 &= \begin{pmatrix} 0 & -I \\ I & 0 \end{pmatrix} \\ \sigma^{0i} &= i\begin{pmatrix} 0 & \sigma^i \\ \sigma^i & 0 \end{pmatrix} \\ \sigma^{ij} = \epsilon_{ijk}\Sigma_k &= \epsilon_{ijk}\begin{pmatrix} \sigma^k & 0 \\ 0 & \sigma^k \end{pmatrix} . \end{aligned}$$

In the Dirac, Majaronna and Chiral representation the γ matrices satisfy

$$\{\gamma^\mu, \gamma^\nu\} = \gamma^\mu\gamma^\nu + \gamma^\nu\gamma^\mu = 2g^{\mu\nu} .$$

The γ_5 matrix is defined as

$$\gamma_5 = \gamma^5 = i\gamma^0\gamma^1\gamma^2\gamma^3 = -\frac{i}{4!}\epsilon_{\mu\nu\rho\sigma}\gamma^\mu\gamma^\nu\gamma^\rho\gamma^\sigma \,,$$

and satisfies

$$\begin{aligned} \left\{\gamma^5, \gamma^\mu\right\} &= 0 \\ \gamma_5^2 = I \quad &, \quad \gamma_5 = {\gamma_5}^\dagger \,. \end{aligned}$$

The γ matrix commutators are

$$\begin{aligned} \sigma^{\mu\nu} &= \frac{i}{2}\left[\gamma^\mu, \gamma^\nu\right] \\ \gamma^\mu\gamma^\nu &= g^{\mu\nu} - i\sigma^{\mu\nu} \\ \gamma_5\sigma^{\mu\nu} &= \frac{i}{2}\epsilon^{\mu\nu\rho\sigma}\sigma_{\rho\sigma} \\ \gamma_5\gamma^0\gamma^i &= \Sigma^i, \text{where } \Sigma^i = \frac{1}{2}\epsilon_{ijk}\sigma^{jk} \,. \end{aligned}$$

Hermitian conjugates of the γ matrices are

$$\begin{aligned} {\gamma_\mu}^\dagger &= \gamma^0\gamma^\mu\gamma^0 \\ {\gamma_5}^\dagger &= \gamma_5 = -\gamma^0\gamma_5\gamma^0 \\ (\gamma_5\gamma^\mu)^\dagger &= \gamma^0\left(\gamma_5\gamma^\mu\right)\gamma^0 \\ (\sigma^{\mu\nu})^\dagger &= \gamma^0\left(\sigma^{\mu\nu}\right)\gamma^0 \,. \end{aligned}$$

B.2 Sakurai Representation

In the Sakurai representation [73] the γ matrices are given by

$$\begin{aligned}
\gamma_i &= \begin{pmatrix} 0 & -i\sigma^i \\ i\sigma_i & 0 \end{pmatrix} \\
\gamma_4 &= \begin{pmatrix} I & 0 \\ 0 & -I \end{pmatrix} \\
\gamma_5 &= -\begin{pmatrix} 0 & I \\ I & 0 \end{pmatrix} \\
i\gamma_5\gamma_i &= i\begin{pmatrix} \sigma_i & 0 \\ 0 & -\sigma_i \end{pmatrix} \\
i\gamma_5\gamma_4 &= i\begin{pmatrix} 0 & I \\ -I & 0 \end{pmatrix} \\
\sigma_{4i} &= \begin{pmatrix} 0 & \sigma_i \\ \sigma_i & 0 \end{pmatrix} \\
\sigma_{ij} = \epsilon_{ijk}\Sigma_k &= \epsilon_{ijk}\begin{pmatrix} \sigma_k & 0 \\ 0 & \sigma_k \end{pmatrix} .
\end{aligned}$$

In this representation the γ matrices satisfy

$$\begin{aligned}
\left\{\gamma_\mu, \gamma_\nu\right\} &= 2\delta_{\mu\nu} \\
\sigma_{\mu\nu} &= \frac{1}{2i}\left[\gamma_\mu, \gamma_\nu\right] = -i\gamma_\mu\gamma_\nu \\
\gamma_5 &= \gamma_1\gamma_2\gamma_3\gamma_4 = \frac{1}{4!}\epsilon_{\mu\nu\rho\sigma}\gamma_\mu\gamma_\nu\gamma_\rho\gamma_\sigma \\
\{\gamma_5, \gamma_\nu\} &= 0 \\
\gamma_5^2 = I \quad &, \quad \gamma_5 = \gamma_5^\dagger .
\end{aligned}$$

Appendix C

Publications By The Author

- S. Boinepalli, D. B. Leinweber, A. G. Williams, J. M. Zanotti and J. B. Zhang, "Precision Electromagnetic Structure of Octet Baryons in the Chiral Regime", to be submitted to PRD.

- S. Boinepalli, D. B. Leinweber, A. G. Williams, J. M. Zanotti and J. B. Zhang, "Precision Electromagnetic Structure of Decuplet Baryons in the Chiral Regime", under preparation.

- D. B. Leinweber, S .Boinepalli, A. W. Thomas, P. Wang, A. G. Williams, R. D. Young, J. M. Zanotti and J. B. Zhang, "Strange electric form-factor of the proton", [arXiv:hep-lat/0601025]

- D. B. Leinweber, S .Boinepalli, A. W. Thomas, A. G. Williams, R. D. Young, J. B. Zhang and J. M. Zanotti, "Systematic Uncertainties in the Precise Determination of the Strangeness Magnetic Moment of the Nucleon", *Eur. Phys. J.* **A24S2** 79 (2005), [arXiv:hep-lat/0601025].

- D. B. Leinweber, S .Boinepalli, I. C. Cloet, A. W. Thomas, A. G. Williams, R. D. Young, J. B. Zhang, J. M. Zanotti and J. B. Zhang, "Precise Determination of the Strangeness Magnetic Moment of the Nucleon", *Phys. Rev. Letta.* **94** 212001 (2005), [arXiv:hep-lat/0406002].

- S. Boinepalli, W. Kamleh, D. B. Leinweber, A. G. Williams and J. M. Zanotti, "Improved Chiral Properties of FLIC Fermions", *Phys. Lett.* **B616** 196 (2005), [arXiv:hep-lat/0405026].

- J. M.Zanotti, S. Boinepalli, D. B. Leinweber, A. G. Williams and J. B. Zhang, "Electromagnetic Form-Factors with FLIC Fermions", *Nucl. Phys. Proc. Suppl.* **128** 233 (2004), [arXiv: hep-lat/0401029].

- D. B. Leinweber, S .Boinepalli, A. W. Thomas, A. G. Williams, R. D. Young, J. M. Zanotti and J. B. Zhang, “ The Strangeness Magnetic Moment of the Nucleon from FLIC Fermions”, *Nucl. Phys. Proc. Suppl.* **128** 132 (2004), [arXiv:hep-lat/0406003].

Bibliography

[1] B. R. Martin and G. Shaw, "Particle Physics", (Wiley - 2001).

[2] S. Eidelman *et al.*, *Phys. Lett.* **B592**,1, 2004.

[3] M. Gell-Mann and Y. Ne'eman, "The Eightfold Way", (Perseus Publishing 1964).

[4] T.Muta, "Foundations Of Quantum Chromodynamics", 2nd Edition, **57**, (World Scientific Lecture Notes).

[5] H. J. Rothe, "Lattice Gauge Theories", (World Scientific, 1997).

[6] Rajan Gupta, "Introduction To Lattice QCD" , 1997.

[7] Christine Davies, "Lattice QCD - A guide for people who want results", 2005.

[8] K. G. Wilson, "New Phenomena In Sub-nuclear Physics", (Plenum, New York, 1975).

[9] G. Curci, P. Menotti, and G. Paffuti, "Symanzik's improved Lagrangian for lattice gauge theory", *Phys. Lett.*, **B130**,205, (1983).

[10] M. Luscher and P. Weisz, "On-shell improved Lattice Gauge Theories", Commun. Math. Phys., **97**, 59 (1985).

[11] G. Peter Lepage and Paul B. Meckenzie, "On the viability of lattice Perturbation Theory", *Phys. Rev.*, **D48**, 2250 (1993).

[12] Mark G. Alford, W. Dimm, G. P. Lepage, G. Hockney and P. B. Meckenzie, "Lattice QCD on small computers", *Phys. Lett.*, **B361**, 87 (1995).

[13] H. W. Hamber and Chi Min Wu, "Some predictions for an improved fermion action on the lattice", *Phys. Lett.*, **B133**, 351 (1983).

[14] B. Sheikhholeslami and R. Wohlert, "Improved continuum limit lattice action for QCD with Wilson fermions", *Nucl. Phys.*, **B259**, 572 (1985).

[15] Martin Luscher, Stefan Sint, Rainer Sommer and Peter Weisz, "Chiral symmetry and $O(a)$ improvement in lattice QCD", *Nucl. Phys.*, **B478**, 365 (1996).

[16] R. G. Edwards, Urs M. Heller and T. R. Klassen, "The effectiveness of non-perturbative $O(a)$ improvement in lattice QCD". *Phys. Rev. Lett.*, **80**, 3448 (1998).

[17] T. DeGrand, "Simple observables from Fat Link fermion actions", *Phys. Rev.*, **D60**, 094501 (1999).

[18] W. Bardeen, A. Duncan, E. Eichten, G. Hockney and H.Thacker, "Light quarks, zero modes and exceptional configurations", *Phys. Rev.*, **D57**, 1633 (1998).

[19] Frederick D. R. Bonnet *et al.*, "Calibration of smearing and cooling algorithms in $SU(3)$- color gauge theory", *Phys. Rev.*, **D62**, 094509 (2000).

[20] M. C. Chu, J. M. Grandy, S. Huang and J. W. Negele, "Evidence for the role of instantons in hadron structure from lattice QCD", *Phys. Rev.*, **D49**, 6039 (1994).

[21] Thomas DeGrand, Anna Hasenfratz and Tamas G. Kovacs, "Optimizing the chiral properties of lattice fermion action", (1998).

[22] Mark Stephenson, Carleton DeTar, Thomas DeGrand and Anna Hasenfratz. "Scaling and eigen mode tests of the Improved Fat Clover Action", *Phys. Rev.*, **D63**, 034501 (2001).

[23] J.M. Zanotti *et al.*, "Hadron masses from Novel Fat-Link Fermion Actions", *Phys. Rev.* **D65**, 074507 (2002).

[24] J. M. Zanotti, B. Lasscock, D. B. Leinweber, and A. G. Williams, "Scaling of FLIC fermions", *Phys. Rev* **D71**, 034510 (2005).

[25] M. Albanese *et al*, "Glueball masses and string tension in lattice QCD", *Phys. Lett.* **B192**, 163(1987).

[26] A. Hasenfratz and F. Knechtli, "Flavor symmetry and the static potential with hyper cubic blocking", *Phys. Rev* **D64**, 034504 (2001).

[27] W. Kamleh, D. B. Leinweber and A. G. Williams, "Hybrid Monte Carlo with Fat Link Fermion Action", *Phys. Rev.* **D70**, 041502 (2004).

[28] Daniel Arndt and Brian C. Tiburzi, "Charge Radii of the Meson and Baryon octets in Quenched and Partially Quenched Chiral Perturbation Theory", *Phys. Rev.* **D68**, 094501 (2003).

[29] Daniel Arndt and Brian C. Tiburzi, "Electromagnetic properties of the Baryon Decuplet in Quenched and Partially Quenched Chiral Perturbation Theory", *Phy. Rev.* **D68**,114503 (2003).

[30] D.E.Groom *et al.*, Review of Particle Physics, *The European Physical Journal*, **C15**, 1 (2000).

[31] E. J. Hackett-Jones, "The role of Chiral Symmetry in extrapolations of lattice QCD results to the physical regime", (2001).

[32] M. N. Butler and M. J. Savage "Electromagnetic polarizability of the nucleon in chiral perturbation theory", *Phys. Lett.* **B294**, 369 (1992).

[33] M. J. Musolf and H. Ito, "Chiral symmetry and the nucleon's vector strangeness form factors", *Phys. Rev.* **C55**, 3066 (1997).

[34] Malcolm N. Butler, Martin J. Savage and Roxanne P. Springer, "Electromagnetic moments of the baryon decuplet" *Phys. Rev.* **D49**, 3459 (1994).

[35] R. F. Lebed, "Determination of $SU(6)$ Clebsch-Gordon coefficients and baryon mass and electromagnetic moment relations", *Phys. Rev.* **D51**, 5039 (1995).

[36] E. Jenkins and A. V. Manohar, "Chiral corrections to the baryon axial currents", *Phys. Lett.* **B259**, 353 (1991).

[37] E. Jenkins, M. Luke, A. V. Manohar and M. J. Savage. "Chiral perturbation theory analysis of the Baryon magnetic moments", *Phys. Lett.* **B302**, 482 (1993)

[38] B. Kubis, T. R. Hemmert and U. Meissner, "Baryon form factors", *Phys. Lett.* **B456**, 240 (1999).

[39] V. Bernard, N. Kaiser and U. Meissner, "Chiral dynamics in nucleons and Nuclei", *Int. J. Mod. Phys.* **E4**, 193 (1995).

[40] S. R.Sharpe, "Quenched Chiral Logarithms", *Phys. Rev.* **D46**, 3146 (1992).

[41] C. W. Bernard and M. F. Golterman, "Chiral perturbation theory for the quenched approximation of QCD", *Phys. Rev.* **D46**, 853 (1992)

[42] J. N. Labrenze and S. R. Sharpe. "Quenched Chiral perturbation theory for baryons", *Phys. Rev.* **D54**, 4594 (1996).

[43] D. B. Leinweber, "Quenched Chiral Perturbation Theory for baryon form factors", *Nucl. Phys.* **B109**, 45 (2002).

[44] D. B. Leinweber and T. D. Cohen, "Chiral corrections to lattice calculations of charge radii", *Phys. Rev.* **D47**, 2147 (1993).

[45] D. B. Leinweber, "Quark contributions to baryon magnetic moments in full, quenched and partially quenched QCD", *Phys. Rev.* **D69**, 014005 (2004).

[46] M. J. Savage, "The magnetic moments of the octet baryons in quenched chiral perturbation theory," *Nucl. Phys.* A **700**, 359 (2002) [nucl-th/0107038].

[47] R. D. Young, D. B. Leinweber and A. W. Thomas, "Leading quenching effects in the proton magnetic moment", *Phys. Rev.* **D71**, 014001 (2005).

[48] M. K. Banerjee and J. Milna, "The decuplet revisited in χPT", *Phys. Rev.* **D54**, 5804 (1996).

[49] I. C. Cloet, D. B. Leinweber, A. W. Thomas "Delta Baryon Magnetic Moments from Lattice QCD", *Phys. Lett.* **B563**, 157 (2003).

[50] D. B. Leinweber, R. D. Young and A. W. Thomas, "Observing chiral non-analytic behavior with FLIC fermions", *Nucl. Phys.* **A37**, 177 (2004).

[51] D. B. Leinweber, R. M. Woloshyn and T. Draper, "Electromagnetic structure of octet baryons", *Phys. Rev.* **D43**, 1659 (1991).

[52] B. L. Ioffe, "Calculation of baryon masses in Quantum Chromodynamics", *Nucl. Phys.* **B188**, 317 (1981).

[53] Y. Chung, H. G. Dosch, M. Kremer, and D. Schall, "Baryon sum rules and Chiral symmetry breaking", *Nucl. Phys.* **B197**, 55 (1982).

[54] M. Benmerrouche, R. M. Davidson, and N. C. Mukhopadhyay, "Problems of describing spin-3/2 baryon resonances in the effective Lagrangian theory", *Phys. Rev.* **C39**, 2339 (1989).

[55] V. M. Belyaev and B. L. Ioffe, "Determination of the baryon mass and baryon resonances from the Quantum Chromodynamics sum rule.Strange baryons", *Sov. Phys. JETP* **57**, 716 (1983).

[56] N. Mathur and S. J. Dong, "Strange magnetic moment of the nucleon from lattice QCD", *Nucl. Phys. Proc. Suppl.* **94**, 311 (2001).

[57] S. J. Dong, *et al.*, "Lattice calculation of the strangeness magnetic moment of the nucleon", *Phys. Rev.* **D58**, 074504 (1998).

[58] R. Lewis, W. Wilcox and R. M. Woloshyn, "The nucleon's strange electromagnetic and scalar matrix elements", *Phys. Rev.* **D67**, 013003 (2003).

[59] D. B. Leinweber *et al.*, "Precise determination of the strangeness magnetic moment of the nucleon", *Phys. Rev. Lett.* **94**, 212001 (2005).

[60] D. B. Leinweber, *et al.*, "Systematic uncertainties in the precise determination of the strangeness magnetic moment of the nucleon", *Eur. Phys. J.* **A24S2**, 79 (2005).

[61] D. B. Leinweber, *et al.*, "Strange electric form factor of the proton", [arXiv:hep-lat/0601025].

[62] D. B. Leinweber, "Lattice QCD evaluation of baryon magnetic moment sum rules", *Phys. Rev.* **D45**, 252 (1992).

[63] D. B. Leinweber, T. Draper and R. M. Woloshyn, "Decuplet baryon structure from lattice QCD", *Phys. Rev.* **D46**, 3067 (1992).

[64] D. B. Leinweber, T. Draper and R. M. Woloshyn, "Baryon octet to decuplet electromagnetic transitions", *Phys. Rev.* **D48**, 2230 (1993).

[65] D. B. Leinweber, "Do quarks really form diquark clusters in the nucleon?", *Phys. Rev.* **D47**, 5096 (1993).

[66] D. B. Leinweber and A. W. Thomas, "A lattice QCD analysis of the strangeness magnetic moment of the nucleon", *Phys. Rev.* **D62**, 074505 (2000).

[67] Y. Kuramashi *et al.*, "Lattice QCD calculation of full pion scattering lengths", *Phys. Rev. Lett.* **71**, 2387 (1993).

[68] S. J. Dong and K. F. Liu, "Stochastic estimation with Z_2 noise", *Phys. Lett.* **B328**, 130 (1994).

[69] S. Nozawa and D. B. Leinweber, " Angular Momentum in Quantum Mechanics", Princeton University Press, Princeton, 1990.

[70] C. Itzykin and J. B. Zuber, "Quantum Field Theory", Mc Graw Hill, New York, 1980.

[71] A. R. Edmonds, *Sov. Phys. JETP* **57**, 716 (1983).

[72] R. Sommer, "A New Way to Set the Energy Scale in Lattice Gauge Theories and Its Application to the Static Force and A_s in $SU(2)$ Yang-Mills Theory", *Nucl. Phys.* **B411**, 839 (1994).

[73] J.J. Sakurai, "Advanced Quantum Mechanics" (Addison-Wesley, 1982).

[74] S. Boinepalli, W. Kamleh, D. B. Leinweber, A. G. Williams and J. M. Zanotti, "Improved chiral properties of FLIC fermions", *Phys. Lett.* **B616**, 196 (2005).

[75] S. Gusken, "A study of smearing techniques for hadron correlation functions", *Nucl. Phys. Proc. Suppl.* **17**, 361 (1990).

[76] J. M. Zanotti, *et al.*, "Spin-3/2 nucleon and delta baryons in lattice QCD", *Phys. Rev.* **D68**, 054506 (2003)

[77] G. Martinelli, C. T. Sachrajda and A. Vladikas, "A study of 'Improvement' in Lattice QCD", *Nucl. Phys.* **B358**, (1991) 212.

[78] T. Draper, R. M. Woloshyn, W. Wilcox, "Electromagnetic Form-Factors of Hadrons", *Nucl. Phys. Proc.Suppl* **9**, 175 (1989).

[79] W. Melnitchouk *et al.*, "Excited baryons in lattice QCD", *Phys. Rev.* **D67**, 114506 (2003).

[80] B. Efron, "Computers and the theory of statistics", SIAM Review, **21**, 460 (1979).

[81] D. B. Leinweber, W. Melnitchouk, D. G. Richards, A. G. Williams and J. M. Zanotti, "Baryon spectroscopy in lattice QCD", [arXiv:nucl-th/0406032].

[82] M. Gockeler *et al.*, [QCDSF Collaboration], "Nucleon electromagnetic form factors on the lattice and in chiral effective field theory," *Phys. Rev.* **D71**, 034508 (2005)

[83] W. Wilcox, T. Draper and K. F. Liu, "Chiral limit of nucleon lattice electromagnetic form-factors," *Phys. Rev.* **D46**, 1109 (1992)